VARIABLE-SPEED SWITCHED RELUCTANCE MOTOR DRIVES FOR LOW-COST, HIGH-VOLUME APPLICATIONS

By

Jae Hyuck Kim

Dissertation submitted to the faculty of the Virginia Polytechnic Institute and State University in partial fulfillment of the requirements for the degree of

Doctor of Philosophy

In

Electrical Engineering

Krishnan Ramu, Committee Chair

Jamie De La Reelopez

Douglas K. Lindner

Daniel J. Stilwell

Werner E. Kohler

March 3, 2010

Blacksburg, Virginia

Keywords: Switched reluctance motor, power converter, variable-speed drives, Low-cost, high-volume applications, sensorless control, optimal efficiency

Abstract

Variable-Speed Switched Reluctance Motor Drives for Low-Cost, High-Volume Applications

Jae Hyuck Kim

Demand for energy-saving variable speed drives in low-cost, high-volume appliances has increased due to energy and environmental concerns and hence the need to comply with new regulations. Switched reluctance motor (SRMs) have been considered by many as attractive alternatives for brush commutated motors or permanent magnet brushless dc motors (PMBDCMs) in such cost-sensitive applications. The SRMs' unique features such as simple and fault-tolerant structure and unidirectional flow of their phase currents endow them with the possibility of various configurations on both machine and converter topologies for different applications. In the present study, three different variable-speed motor drive systems are proposed, studied, and implemented for their deployment in low-cost, high-volume applications with the power rating of 1.5kW or less. Two different two-phase SRMs and three different power converters are employed to realize three different low-cost drive systems. The first drive system is realized using a novel converter requiring only a single-controllable switch and an asymmetric two-phase 8/4 SRM capable of self-starting and four-quadrant operation. The second drive system is realized using another novel converter requiring two controllable switches, that way to achieve better control and utilization of the asymmetric 8/4 motor. The target applications for both drive systems are low power, low performance drives such as fans, hand tools, small appliances, etc. The third system is realized using a high-speed two-phase 4/2 SRM and a split ac source converter, which is designed for high-speed applications such as vacuum cleaners, ultracentrifuges, etc. The control and design aspects for each drive system are studied. Selection of optimal firing angles and optimal number of winding turns are also investigated. All of the drive systems are first demonstrated on the position sensor-based speed-control scheme. To

make the drive system even more cost-competitive, operation without the position sensor using the novel parameter insensitive sensorless control scheme is proposed and implemented. Concept, analysis, simulation, and experimental verification of the proposed sensorless scheme are discussed in detail.

Acknowledgements

First and foremost, I would like to express my sincere gratitude to my advisor, Professor Krishnan Ramu for his invaluable encouragement and guidance throughout the course of this research. He has given me the opportunity to instill in me the fundamentals of electric machines and drives that will continue to keep me firmly grounded in my future endeavors.

I would also like to thank my committee members, Dr. Jamie De La Reelopez, Dr. Douglas K. Lindner, Dr. Daniel J. Stilwell, and Dr. Werber E. Kohler for their encouragement and concerns.

Additional special thanks go to my colleagues: Cheewoo Lee for his camaraderie and encouragement whenever I have needed it and Ethan Swint and Nimal Lobo for their proofreading and technical discussions.

Last but not least, I wish to express everlasting thanks to my parents, parents-in-law and the rest of my family for their wholehearted love and support. Without them, I would not ever made it this far. The most crucial support came from my wife, best friend, and partner, Jeongwoo. Your patience, love, and strength helped me complete this journey. Thank you.

Table of Contents

List of Figures

List of Tables

Chapter 1

Introduction

1.1 Motivation

Growing energy and environmental concerns have intensified demand for variable-speed drives in emerging low cost, large volume applications such as heating, ventilating, and air conditioning (HVAC), fans, home appliances, etc [1], [2]. Most of these applications traditionally utilize drives with constant or few sets of speed and hence their regulation is achieved primarily by throttling the output flow of the media or simple on-off control. However, various benefits such as energy savings, better utilization of the motors, reduced maintenance, extended motor life, and improved comfort level can be obtained by employing variable-speed drives into these applications [3], [4]. The higher cost of conventional variable-speed drives compared to fixed-speed drives has been the main reason that the variable-speed drives have not penetrate such cost-sensitive applications. Fig. 1.1 shows a conventional variable-speed ac drive with the standard three-phase inverter. Although this provides high dynamic performance over a wide speed range, the high cost associated with the six-switch-based inverter is major impediment for its wider acceptance in residential applications. The universal motors with a triac or one-quadrant chopper [5], shown in Fig.1.2, may be the simplest existing variable-speed drives and acceptable in some low-power, low-performance appliance drives; however, their limited lifetime, acoustic noise, controversy over the harmful effects of carbon dust and electromagnetic interference (EMI), and severely curtailed overload capability due to their brush-commutator assembly disqualify them from any further consideration.

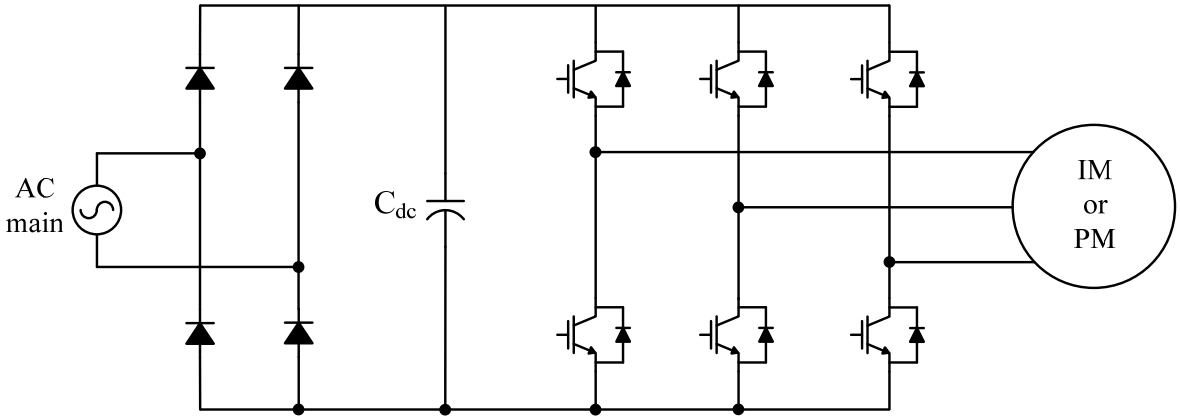

Fig. 1.1. Conventional variable-speed ac drive with six-switch-based inverter

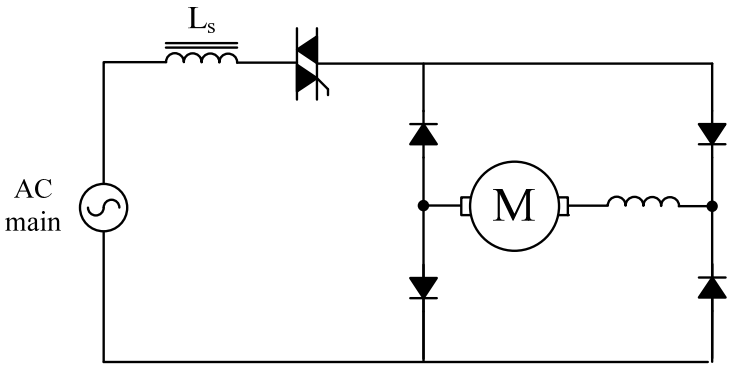

(a) ac drive using a Triac

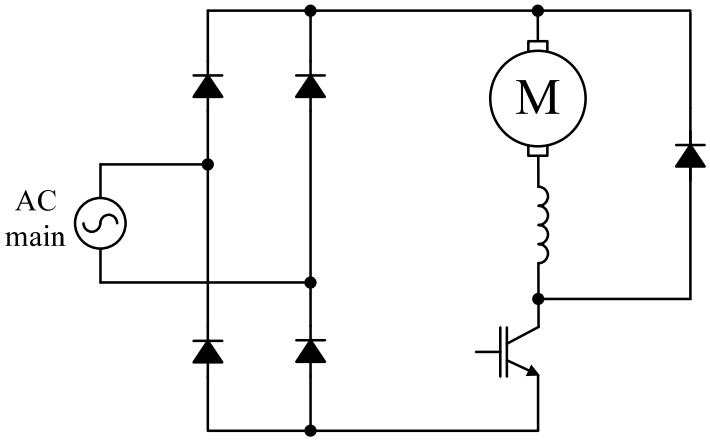

(b) dc drive using a one-quadrant chopper

Fig. 1.2. Universal motor drives

Therefore, the search for a simple, low-cost, brushless, variable-speed drive has intensified with the emerging variable-speed applications in residential HVAC and home appliances. Several low-cost drives with a reduced number of controllable switches, such as a single-phase induction motor with two switches [4] (Fig.1.3), a two-phase induction motor with four controllable switches [6] (Fig.1.4), a three-phase induction motor with three switches [7] (Fig.1.5) a three-phase permanent-magnet brushless dc (PMBLDC) motor with three switches [8] (Fig.1.6) have been published, to name a few. Although they presented reasonable performance with much less cost compared to the standard six-switch-inverter-based AC drives, manufacturing cost and or complexity of induction and permanent magnet brushless motors remain high thereby making the drive system cost beyond the reach of many of the targeted applications. Therefore, research and development has been ongoing in search for viable "brushless" and "magnetless" alternatives.

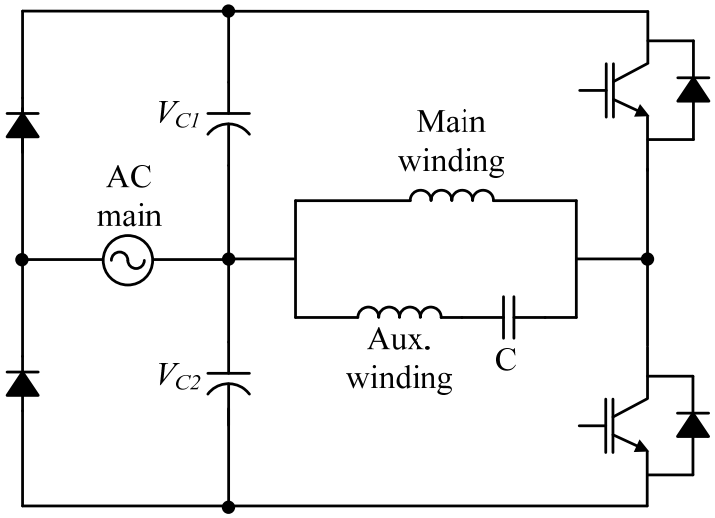

Fig. 1.3. Permanent split capacitor (PSC) single-phase induction motor using two controllable switches

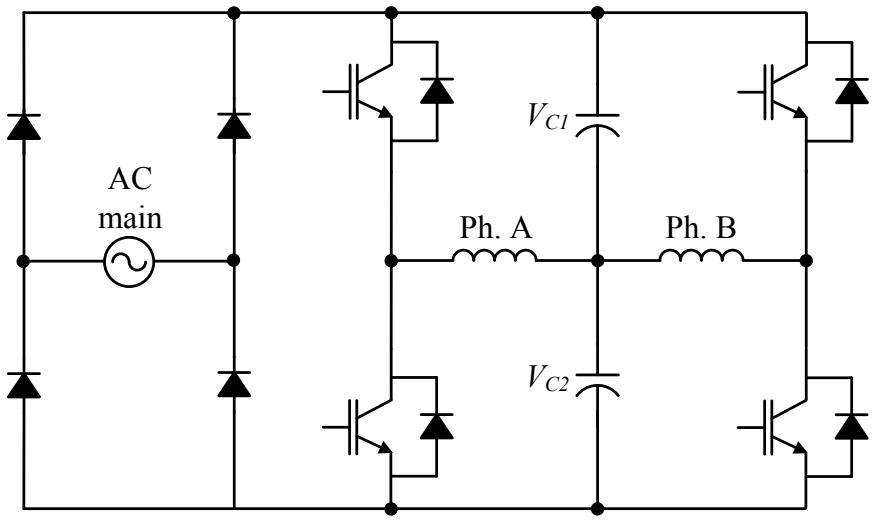

Fig. 1.4. Two-phase induction motor drive using four controllable switches

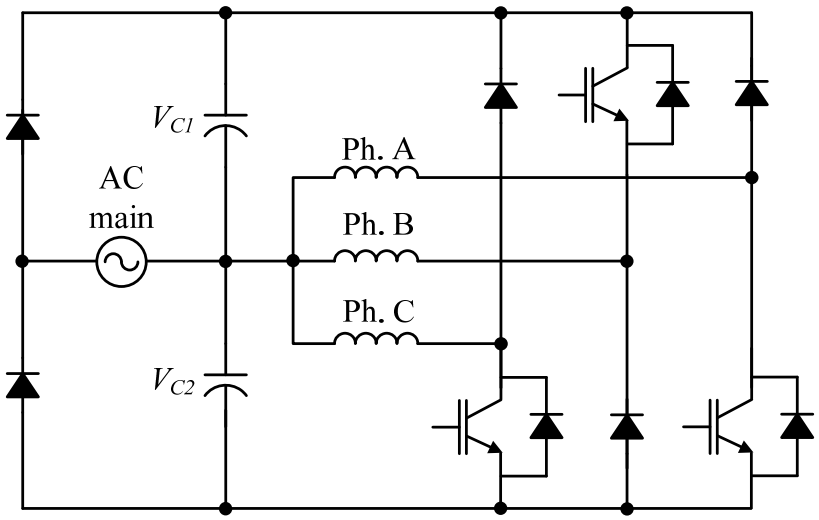

Fig. 1.5 Asymmetric three-phase induction motor drive using three-controllable switches

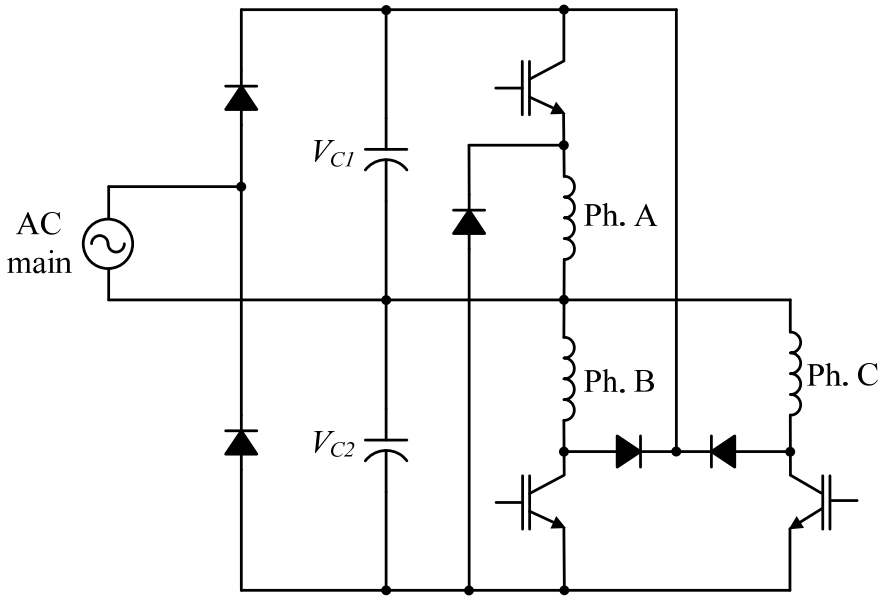

Fig. 1.6. Permanent magnet dc motor using three controllable switches

The switched reluctance motor (SRM) is known to be the lowest cost motor with the simplest construction having no brushes, commutators, windings, or magnets on its rotor and only concentrated windings on its stator [9],[10]. The simple configuration, along with the features such as unidirectional flow of current and negligible mutual coupling between the phases lends itself to a variety of motor and converter topologies for each intended application. Key to realizing cost minimization in SRM drives is reduction in the number of machine phases, preferably single or two-phase machines, and reduction in converter electronics, i.e., reduced number of switching devices. The single-phase SRM is known to be the simplest machines of all, requiring minimum amount of driving circuits. The drawbacks of the single-phase SRM, however, include the lack of self-starting capability unless otherwise built in to the machine with the additional mechanism such as a parking magnet, poor air-gap utilization, high peak-to-peak torque ripple, and increased acoustic noise [11], [12]. The applications are thus limited to applications which require limited starting torque and can tolerate large torque ripple such as fans. With proper design, the two-phase SRM can provide reliable starting at any rotor position without resorting to any additional apparatus. Although it may be more expensive than the single-phase SRM due the increased copper volume and converter electronics, the two-phase

SRM has less torque ripple and hence less acoustic noise and with conventional 4-2 structure this motor can still be a good candidate for high-speed vacuum cleaners.

A two-phase SRM with a two-switch-based asymmetric converter shown in Fig. 1.7 is found to be competitive for low-cost variable-speed applications. While this drive system provides desirable performance with significantly reduced drive electronics, a further reduction in cost and components would be highly appealing to some sectors of industry while for many others it is almost a necessity to meet highly cost-sensitive high-volume applications. In this study, three different low-cost brushless variable-speed drives realized by two different two-phase SRMs and three different low-cost converters are presented. Two novel converters for two-phase SRMs where the energy recovery is retained within the motor are proposed. All of the proposed drive systems are modeled, designed, analyzed, simulated, and experimentally verified. To make the proposed systems more viable for their intended applications, position sensorless control as well as power factor correction are also investigated and implemented. The detailed outline of this thesis is discussed in section 1.3.

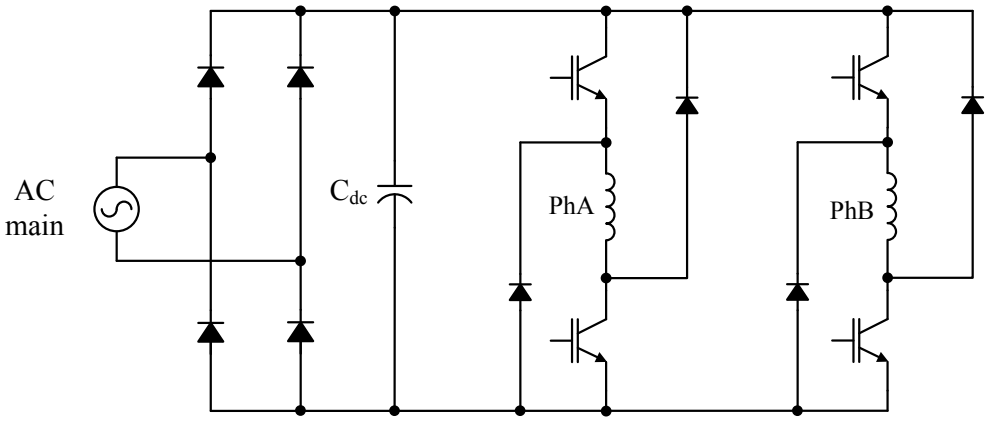

Fig. 1.7. Two-phase SRM drive with asymmetric converter

1.2 Scope and Contributions

The scope of this research is to develop low-cost, high-efficiency, anbrushless variable speed drives system targeting low-cost, high-volume application, such as the home appliance markets. Three different two-phase SRM drives are designed and implemented with a focus on minimum electronics and simple yet efficient drive control to meet the demanding requirement from home appliance market in terms of cost, efficiency, input power factor.

The scope and key contributions made in this research include:

1) Analysis, design, simulation, and experimental verification of the proposed two-phase, single-controllable-switch-converter based SRM drive.
2) Analysis, design, simulation, and experimental verification of the proposed two-phase, two-controllable-switch-converter based SRM drive
3) Analysis, design, simulation, and experimental validation of the proposed two-phase, two-switch based, high-speed SRM drive.
4) Optimal efficiency control in single-pulse mode with optimal number of winding turns.
5) Parameter insensitive position sensorless control and its implementation with the above proposed drive systems to achieve further cost reduction.
6) Study of effect of input power factor correction and its implementation using only passive components and the drive structure without external electronics.
7) Comparative study of the proposed drive systems, along with the existing brush-commutator or permanent magnet motors to provide guideline for their selection based on the requirement for their intended applications.

1.3 Outline of Dissertation

The report on this research is organized into chapters as follows.

Chapter 1 introduces the motivation, review, scope and contribution of the presented research work. In the review section, basic principle of operation of SRMs and state-of-art-review of SRMs of the single- and two-phase SRMs as well as converter topologies for low cost applications is discussed.

Chapter 2 briefly describes a theory behind the fundamental principles of SRM drives in terms of principles of operation, modeling, and control of the SRM. A review of state-of-art-converters for SRMs is also discussed.

Chapter 3 presents a novel single-controllable switch-based, two-phase SRM drive system. In this chapter, the key design consideration for both converter and machine parameter is discussed. The operation principle, derivation of converter modeling, dynamic simulation, and experimental validation are also presented.

Chapter 4 presents a novel two-switch-based, two-phase SRM drive system. Converter modes of operation and their derivation are followed. The estimation of energy transfer between the capacitors and estimation of the secondary capacitor voltage is also presented. The key design consideration is discussed, followed by dynamic simulation and experimental verification.

Chapter 5 presents a two-phase SRM drive system for high speed application. Modeling of the converter and motor is presented and then the effect of angle control as a main control parameter is characterized and discussed. Converter modes of operation and their derivation are followed. The effect of winding number turn as a key design parameters is studied and it optimal selection is discussed.

Chapter 6 presents a new position sensorless control algorithm. The brief review of state-of-art sensorless methods is discussed. Then, derivation of the proposed algorithm is followed.

Digital implementation as well as simulation is also presented and experimental verification on the proposed drive system is presented.

Chapter 7 summarizes the results and provides the key conclusions of this research work. Advantages and limitations of the proposed system will be reviewed. Ongoing and future related work will be discussed

Chapter 2

SRM Fundamentals and State-of-the-Art-Review of SRM Converters

2.1 SRM Fundamentals

The SRM is a doubly salient motor with simple mechanical construction. The rotor is made of sheets of laminated steel with no windings or permanent magnets on it. The stator is also made of sheets of laminated steel with concentrated windings wound on the stator poles. Fig. 2.1 shows a conventional three-phase 6/4 SRM with six salient poles on the stator and four salient poles on the rotor. The windings on each diametrically opposite pole pair are connected in series forming an individual stator phase. The motor is driven by a sequence of current pulses applied in each phase. The individual phases are consequently energized, forcing the motor to rotate. The resulting torque is created based on reluctance forces which lead to a pair of rotor poles moving into alignment with the excited stator pole pairs.

2.1.1 Principles of Operation

Fig. 2.2 shows the idealized profiles of inductance, current, and corresponding torque with respect to the rotor position for a phase of the three-phase 6/4 SRM. Waveforms for only one phase are shown. Each cycle (equal to the rotor pole pitch) has four distinct regions of inductance profile. Since torque production is associated with derivative of the inductance with rotor position, current is desired only where the inductance is either increasing ($dL/d\theta > 0$) for

motoring operation or decreasing ($dL/d\theta < 0$) for generating operation. The sign of the torque is determined by whether the inductance is increasing or decreasing, not by the direction of the current in the motor winding. Therefore, for motoring operation, the phase excitation should be established from the onset of the increasing current at θ_1 until the position with the maximum inductance, L_{max} at θ_2. From θ_2 to θ_3, both the stator and rotor poles are completely overlapped each other and hence the inductance remains constant at L_{max}. For generating operation, the phase winding must be energized during the region between θ_3 and θ_4, where the inductance decreases linearly toward the minimum value, L_{min}. From θ_4 to θ_1, the stator and rotor poles are not overlapped and the inductance remains constant at L_{min}. Since the variation of the inductance is zero for both regions of θ_2-θ_3 and θ_4-θ_1, there is no torque production in these regions.

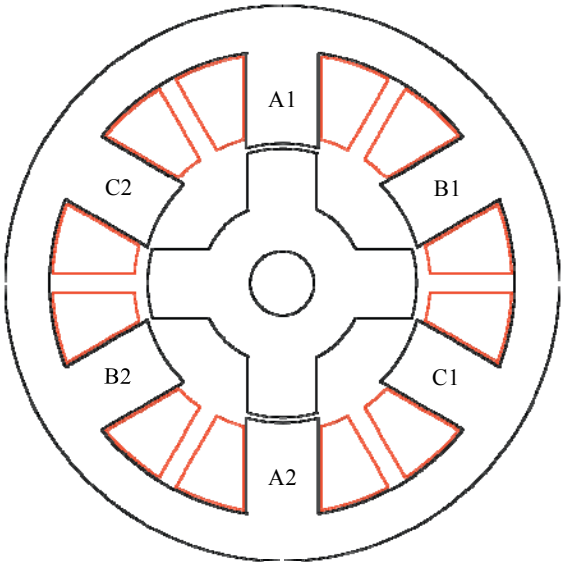

Fig. 2.1. Three-phase 6/4 SRM

Excitation of the individual phases A, B, and C can be achieved by placing the current pulse for each phase shifted by electrical 120º relative to each other. The level of torque is dependent on the amplitude of the current pulse set by current controller. In addition to the current amplitude, correct placement of current pulse with respect to the rotor position is of prime importance in successful operation of the SRM. In practice, the current cannot rise or fall instantaneously as oppose to the idealized waveform in Fig. 2.2. Hence, it is necessary to properly advance turn-on and turn-off angles based on the operating speed.

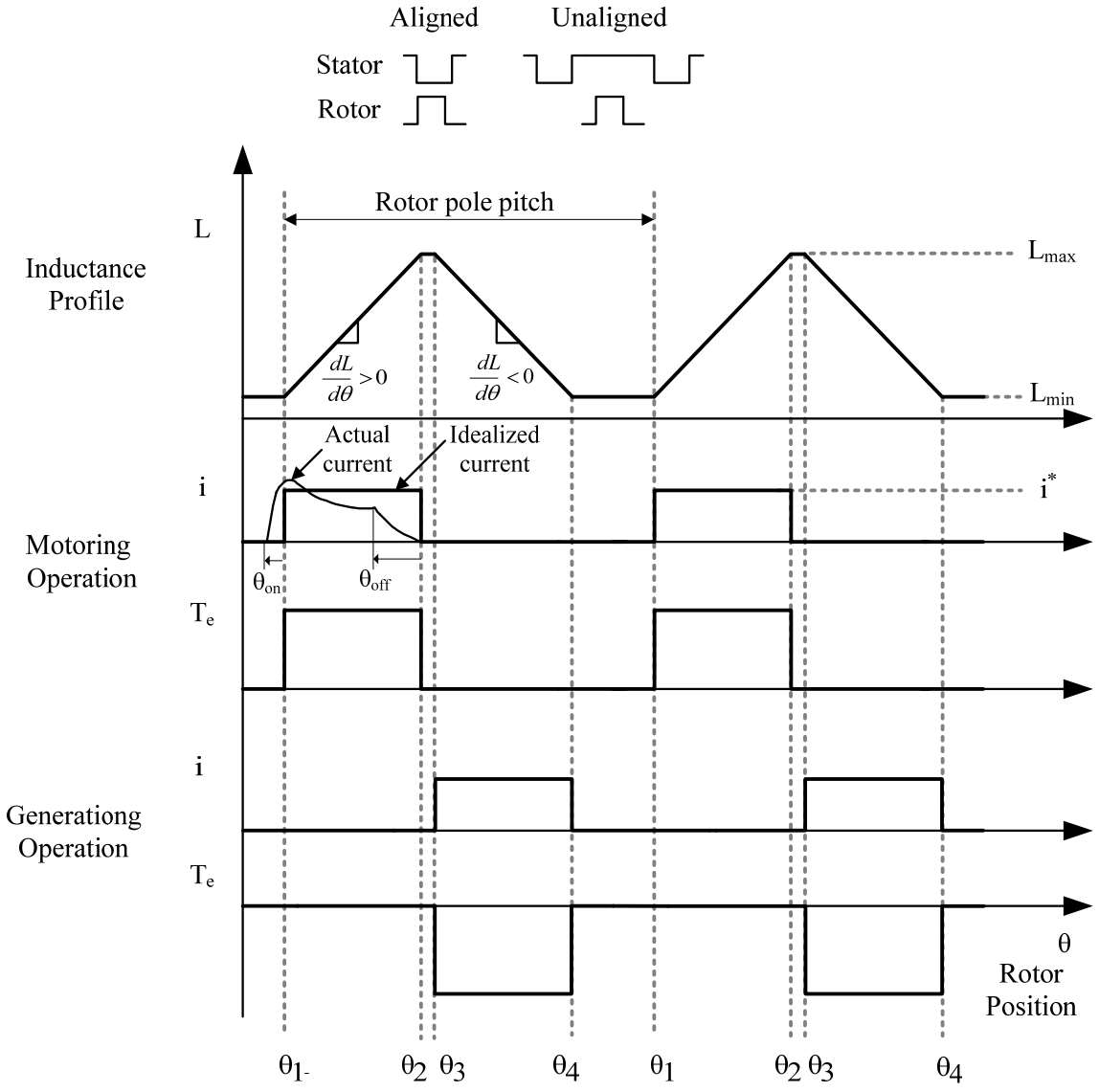

Fig. 2.2. Idealized waveforms of a phase of the three-phase 6/4 SRM
(Inductance, current, and torque profiles)

2.1.2 Mathematical Model of SRM

The SRM is a highly nonlinear system. Based on the non-linear theory describing the behavior of the motor, a mathematical model of an SRM can be created. The mathematical model enables simulation of the SRM system and hence development and implementation of sophisticated algorithms for controlling the SRM is feasible. The electromagnetic dynamics of an

SRM can be represented using Faraday's Law. For an N-phase SRM, the stator voltage equation for a phase coil can be expressed in terms of the phase currents and flux linkages:

$$\sum_{n=1}^{N} \frac{d\lambda_{kn}(\theta, i_n)}{dt} = v_k - R_k i_k \tag{2.1}$$

where θ is the rotor position, i_k is the phase current, v_k is the phase voltage, and R_k is the resistance of the phase coil respectively. Generally, the effect of mutual coupling in an SRM is negligible. Thus, the stator voltage equation can be given as

$$\frac{d\lambda_k(\theta, i_k)}{dt} = v_k - R i_k \tag{2.2}$$

Using the chain rule, (2.2) can be rewritten as

$$\begin{aligned} v_k - R_k i_k &= \frac{\partial \lambda_k(\theta, i_k)}{\partial i_k}\frac{di_k}{dt} + \frac{\partial \lambda_k(i_k, \theta)}{\partial \theta}\frac{d\theta}{dt} \\ &= l_k(\theta, i_k)\frac{di_k}{dt} + e_k \end{aligned} \tag{2.3}$$

Since the flux is the product of inductance and current, $\lambda_k = L_k i_k$, (2.3) can also be rewritten as

$$\begin{aligned} v_k - R_k i_k &= \frac{\partial\{L(i_{ph}, \theta) i_{ph}\}}{\partial i_{ph}}\frac{di_{ph}}{dt} + \frac{\partial\{L(i_{ph}, \theta) i_{ph}\}}{\partial \theta}\frac{d\theta}{dt} \\ &= \left(L(i_{ph}, \theta) + i_{ph}\frac{\partial L(i_{ph}, \theta)}{\partial i_{ph}} \right)\frac{di_{ph}}{dt} + i_{ph}\frac{\partial L(i_{ph}, \theta)}{\partial i_{ph}}\frac{d\theta}{dt} \\ &= l_k(\theta, i_k)\frac{di_k}{dt} + e_k \end{aligned} \tag{2.4}$$

From (2.2) and (2.3), $l_k(\theta, i_k)$ and e_k are the incremental inductance and back-EMF respectively.

$$l_k(\theta,i_k)=\frac{\partial\lambda_k(\theta,i_k)}{\partial i_k}=\left(L(\theta,i_k)+i_k\frac{\partial(\theta,i_k)}{\partial i_k}\right) \tag{2.5}$$

$$e_k=\frac{\partial\lambda(i_k,\theta)}{\partial\theta}\frac{d\theta}{dt}=i_k\frac{\partial L(\theta,i_k)}{\partial\theta}\frac{d\theta}{dt} \tag{2.6}$$

The electromagnetic torque of the SRM is given as

$$T_e=\sum_{k=1}^{N}\frac{\partial W_{ck}(\theta,i_k)}{\partial\theta} \tag{2.7}$$

where $W_{ck}(\theta,i_k)=\int_0^{i_k}\lambda_k(\theta,i_k)di_k$ is the co-energy. In the linear operating region, the electromagnetic torque can be expressed in terms of derivative of the phase inductances and the square of the phase currents:

$$T_e=\frac{1}{2}\sum_{k=1}^{N}i_k^2\frac{dL_k(\theta)}{d\theta} \tag{2.8}$$

Using the stator voltage equation and the load dynamic equation, the mathematical model of N-phase SRM can be given by (2.9) and (2.10) and its block diagram representation is depicted in Fig. 2.3. To calculate the current and torque waveforms, the dynamic model of an SRM has to be solved, i.e. the differential equations for all N phases' stator voltages and the mechanical equation have to be integrated simultaneously as shown in Fig. 2.3.

$$\begin{bmatrix}\frac{d\lambda_1(\theta,i_1)}{dt}\\ \frac{d\lambda_1(\theta,i_2)}{dt}\\ \vdots\\ \frac{d\lambda_N(\theta,i_N)}{dt}\end{bmatrix}=\begin{bmatrix}v_1\\ v_2\\ \vdots\\ v_N\end{bmatrix}-\begin{bmatrix}R_1 & 0 & \cdots & 0\\ 0 & R_2 & & \vdots\\ \vdots & & \ddots & 0\\ 0 & \cdots & 0 & R_N\end{bmatrix}\begin{bmatrix}i_1\\ i_1\\ \vdots\\ i_N\end{bmatrix} \tag{2.9}$$

$$\frac{d\omega}{dt}=\frac{1}{J}\left[\sum_{k=1}^{n}T_k(\theta,i_k)-B\omega-T_L\right] \tag{2.10}$$

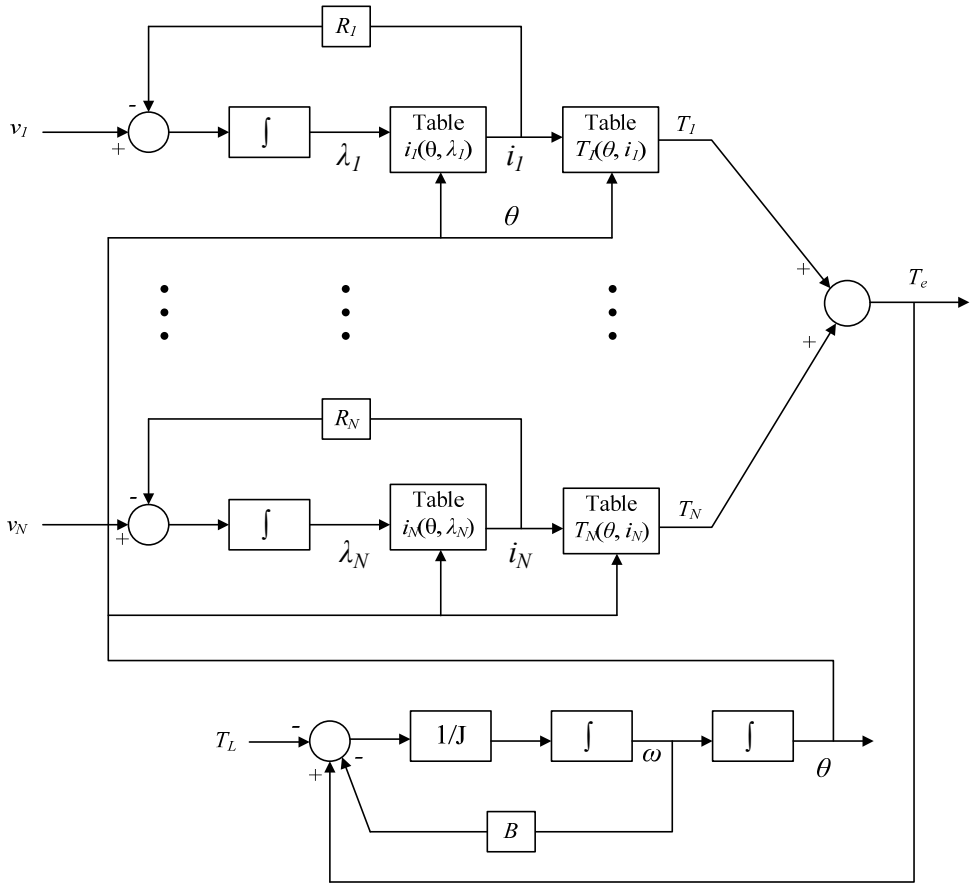

Fig. 2.3. Block diagram representation of dynamic mathematical model of an n-phase SRM

First, the flux and rotor speed is calculated from the integration and then the phase current and the torque is calculated from the lookup tables of magnetization and torque characteristics obtained from either finite element analysis (FEA) simulation or curve fit based off a few measured data sets.

The electromagnetic circuit of the SRM is characterized by non-linear magnetization which is a function between the magnetic flux, the phase current, and the motor position. The influence of the phase current is most apparent in the aligned position, where saturation effects can be observed. The torque generated by the motor phase is a function of the magnetic flux. Therefore, the phase torque is not constant for constant phase current for different motor positions. This contributes to torque ripple and acoustic noise.

2.1.3 Control of SRM

Torque production of the SRM resembles that of stepper motors in that coils in the stator serve as electromagnets that attract the nearest rotor poles. One of the important differences between the SRM and the stepper is that while a stepper operates open loop, an SR motor does not operate open loop but rather monitors its rotor position. Stator coils are energized in synchronism with the rotor and only when it is advantageous to do so. Fig. 2.4 depicts a cascaded control configuration for SRM drives. The outermost control loop is, in general, speed control, but it can be position control in case of servo drives. The innermost loop is generally current control which is implemented by either hysteresis or linear PI controller. If the drive does not require torque control or high performance, average phase voltage control by PWM chopping may be more desirable than current control. In that case, torque controller is not needed. Another important control block is control of switching angles (turn-on, turn-off) for proper placement of current pulses in synchronism with rotor position. Once the current reference and switching angles are defined, the proper sequence of excitation for each phase, so called "commutation" is executed. Therefore, performance of the SRM drives hinges on the performance of the current controller as well as correct placement of the current excitation. This leads to important control parameters of SRM drives: current reference, turn-on angle, turn-off angle.

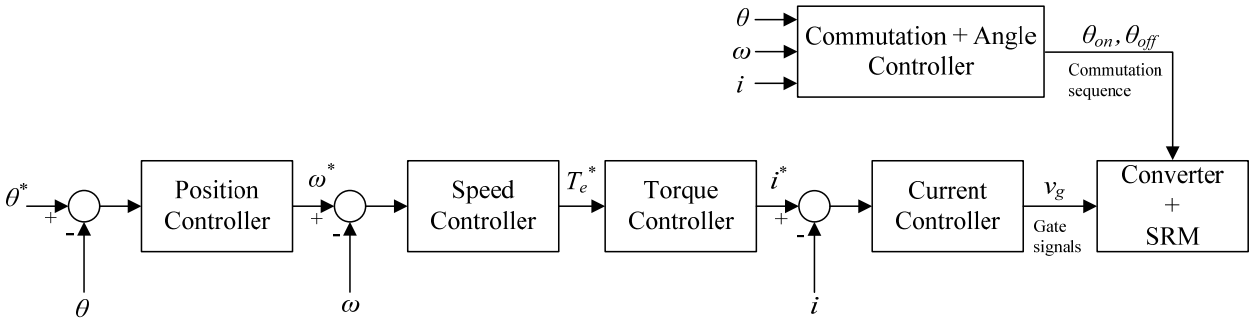

Fig. 2.4. Cascaded control block diagram for an SRM drive.

A torque-speed characteristic for SRMs is shown in Fig. 2.5. At low speeds, the motor back-EMF is much smaller than source voltage thereby allowing rapid buildup and decay of the

phase current. Therefore, torque production can be achieved mainly by current control with fixed or small variation of switching angles. As the speed increases, the motor back-EMF becomes significant and this slows the rise and the fall of current in the phase winding. Because the rate of current rise is slower, the rotor traverses a significant angle in the time it takes the current to rise to the commanded value and this results in loss of torque. Therefore, it is necessary to advance the turn-on angle in order to build current in the phase winding before the onset of pole overlap, and to extinguish the current before substantial braking torque is generated. Thus, control of switching angles becomes significant for higher speeds. The operation region below the base speed, ω_b is called current-limited or constant-torque region since the current and torque production should be limited and torque can be maintained at any speed by current control.

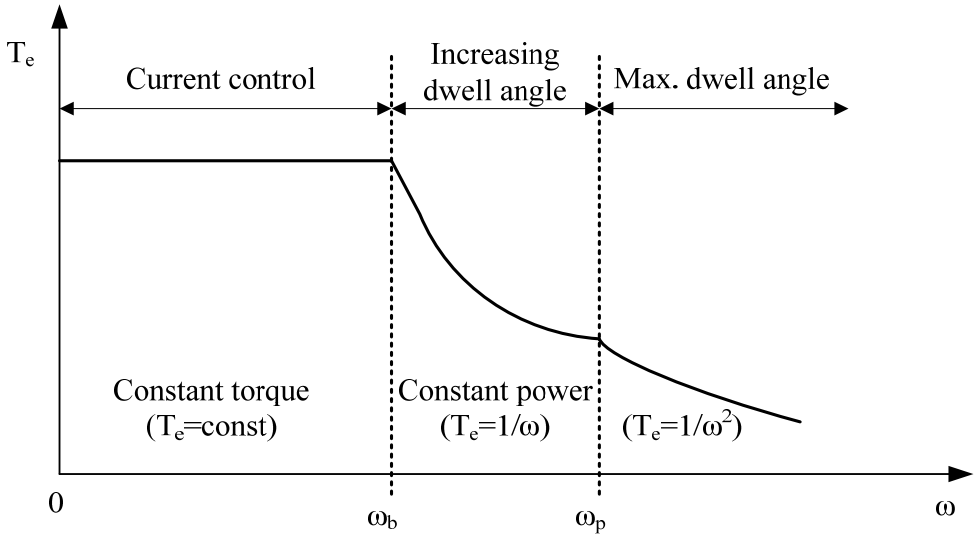

Fig. 2.5. SRM torque-speed characteristics

When the speed increases beyond the base speed, the back-EMF exceeds the supply voltage. In this region, PWM chopping is not achievable and hence the required torque is produced by advancing the turn-on angle significantly and thus increasing dwell angle. The current is switched on and off only once in each conduction period, thereby called “single-pulse operation”. Switching angles are only parameters to control torque. The operation region beyond the base speed is called constant power region and torque in this region falls off inversely proportional to speed (1/ω). If the speed increases even further beyond the point at which where

the maximum dwell angle is reached (ω_p), the motor enters maximum dwell region. Maintaining torque above this speed is not possible, and the torque falls off inversely proportional to square of speed ($1/\omega^2$).

2.2 State-of-the-Art-Review of SRM Converters

Unlike the induction motors or dc motors, the SRMs cannot run directly from an ac or dc power supply. A certain amount of control via a power electronic converter as an electronic commutator is required to control the supply of the current to the phase winding. Hence, the power converter has been one of the main research aspects of the SRM drives since the performance and cost of the drive is highly affected by the converter configuration. A large number of converter topologies have been proposed hitherto and their comparative studies have been published in [10], [13]-[17] to facilitate the selection of an appropriate converter topology for a wide range of applications. Several important requirements to be considered for designing or selecting a converter topology for the SRM are summarized as below.

- In an SRM, the torque is produced irrespective of the direction of the flux through the stator and rotor poles. Thus, only a unidirectional flow of phase current is required resulting in simpler and more reliable power converter circuits.
- The purpose of power converter circuit is to provide some means of increasing the supply of current to the phase winding. Hence, for the purpose of the phase current control, it is necessary to modulate the phase voltage. This is especially important at low speed, when the motor back-EMF is low.
- The magnetic field energy stored in the winding has to be provided with a path during commutation of a phase so that the surplus energy returned to the power supply rails without resulting in excessive voltage across the windings.
- For maximum control flexibility, the converter should be capable of providing three different excitation modes: positive voltage, negative voltage, zero voltage modes.
- The demagnetization voltage needs to be as high as possible in order to achieve fast fall time of the phase winding current should be as fast as possible.

- Large fall time of phase current results in negative torque and this time can be reduced if demagnetizing voltage is as high as possible.
- To reduce system cost, a low number of semiconductor switches is desirable.
- To reduce the torque ripple, it is necessary, at the same time, to control current in one phase and force demagnetizing of other phase of the motor.

In this section, the review of the converter topologies for SRM drives so far published is discussed. There are several factors for characterizations of the converter topologies but in general the converters can be classified by either the number of the controllable switches or the way the energy stored in the phase windings is managed.

2.2.1 Classification Based on the Number of Controllable Switches

Fig.2.6 shows the classification of the SRM converters based on the number of the required controllable switches. The SRM requires at least one controllable switch per phase for basic commutation of the operation. This leads itself to a single-switch-per-phase configuration which requires the minimum number of the switches among the existing converter topologies. However, to achieve more control flexibility additional switches are inevitable. In general, the converters with more switches per phase deliver more control flexibility and better performance but more expensive is their system cost. Detailed description of the converters for each category is as follows.

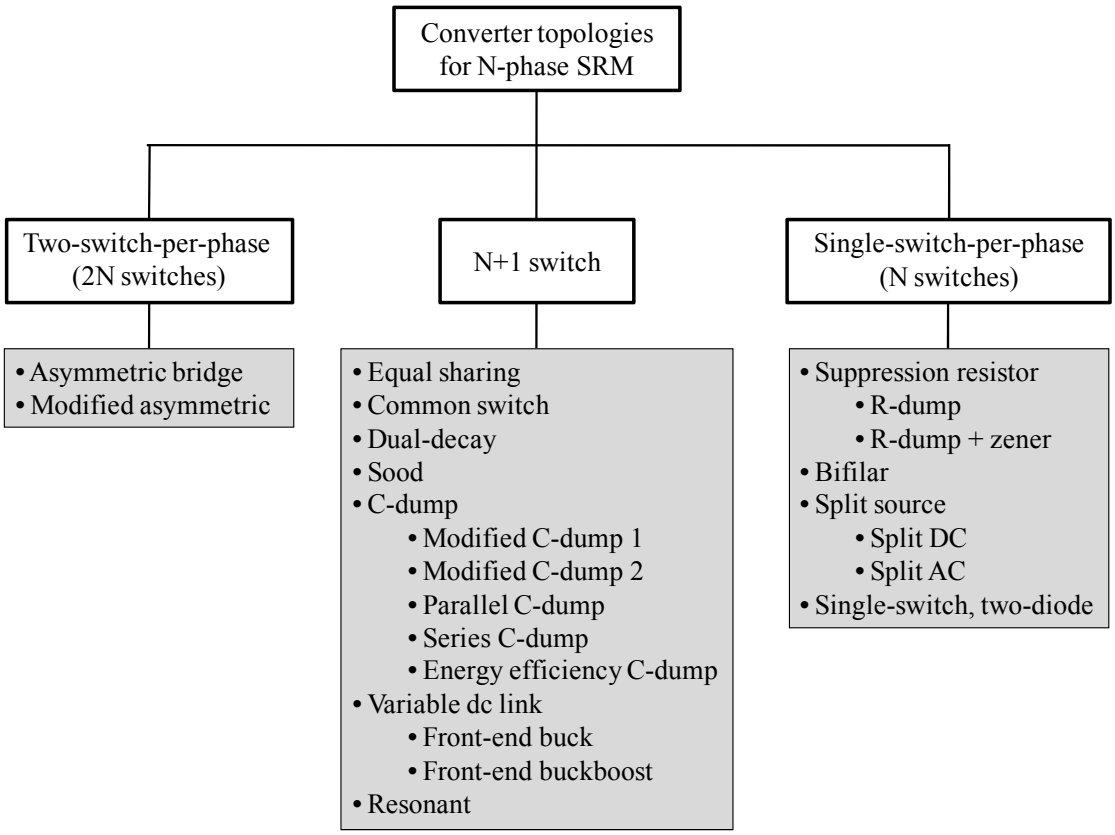

Fig. 2.6. Classification of the SRM converters based on the number of the controllable switches

2.2.1.1 Two-switch-per-phase Converters

Asymmetric converter [18]-[20]: The classic asymmetric bridge converter shown in Fig. 2.7 is one of the most widely used topologies. The asymmetric converter employs two switches per phase, with two freewheeling diodes to return the regenerative energy to the supply, hence requiring total of 2N switches and 2N diodes. The converter has the advantages of complete control of each phase winding. However, the per-phase component count is high due to the total number of switches along with their associated drive circuits thus making the drive system expensive. Therefore, the bridge converter is best fit for high performance applications, where the cost of the converter is not of prime importance.

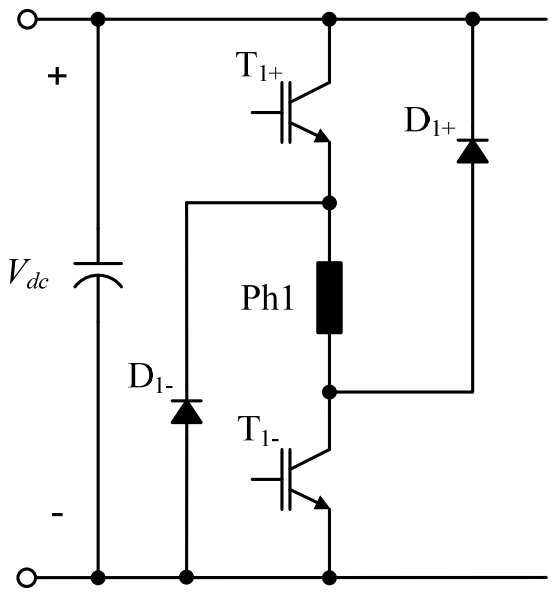

Fig. 2.7. Asymmetric bridge converter (only one bridge for one phase is shown)

2.2.1.2 N+1 Switch-Per-Phase Converters

The converters in this category have total of N+1switches, where N is the number of motor phases. There are several different configurations under this category and they are discussed as below.

Configuration with a common shared switch [21],[22]: Each phase of the motor requires only one diode and switch and there is an additional switch and a diode, shared by all phases for phase commutation. Although this converter has fewer switches than bridge converter it has the critical disadvantage that the commutation cannot be used until the other phase has been completely demagnetized making phase independence impossible. It does not tolerate phase overlapping, and therefore, its capability is very limited, particularly for the single-pulse mode.

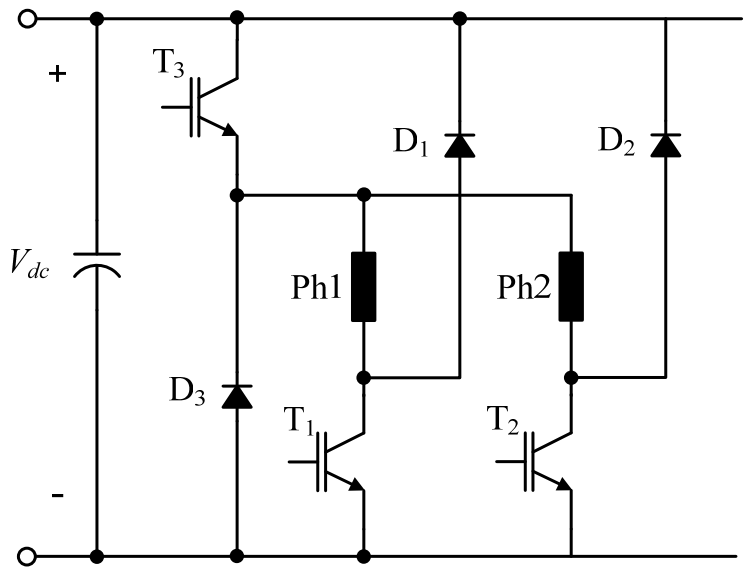

Fig. 2.8. Shared switch N+1 converter for two-phase SRM

Dual decay converter [26]: This converter is basically variation from the suppression resistor converter with switch across the resistor and since the switch is shared by all other phases, the converter has the similar to shared switch N+1 converter.

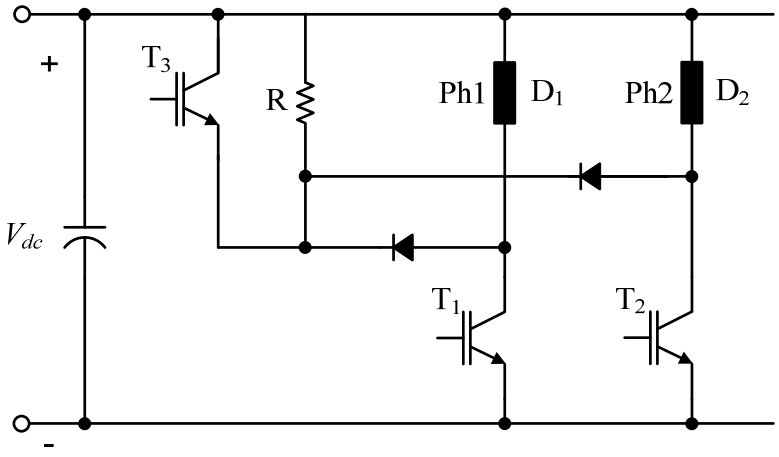

Fig. 2.9. Dual decay converter

Other N+1 configuration: C-dump converter, variable dc link, resonant, etc.

Although these converters basically retain (N+1) switch configuration, the additional switch is endowed from the extra circuit which are best characterized in terms of energy recovery and variable dc link. Thus, these converters are discussed in the later section.

2.2.1.3 Single-Switch-Per-Phase Converters

The converters employing the single-switch-per-phase configuration requires total of N switches for an N phase motor. They are appealing specifically to low cost, low performance drives due to their compactness of the converter package and hence a possible reduction in their cost compared to other converters. They have disadvantage of being unable to apply zero voltage across the winding and thus the soft chopping is not achievable, leading to higher current ripple than two-switch-per-phase or N+1 switch converters. There several different configurations in this category.

Suppression resistor (R-dump) converter [23]-[25]: Converters shown in Fig. 2.10 uses an external resistor to generate the suppression voltage across the winding. This has the disadvantage that the energy is dissipated in a resistor, thus reducing the overall efficiency of the drive system. When a zener diode is employed with the dump resistor, a higher value of suppression voltage during the freewheeling period is sustained.

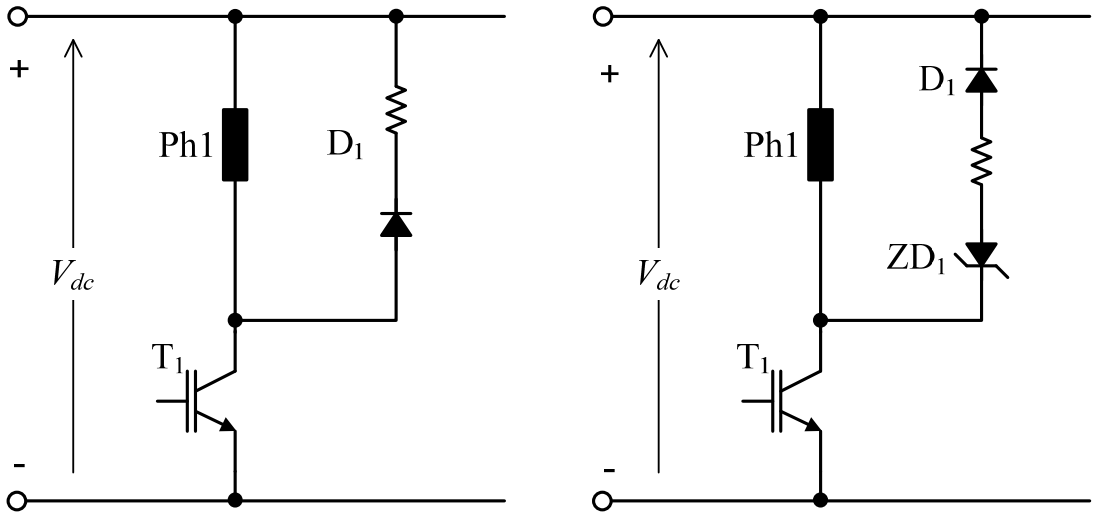

(a) Dump resistor (b) Dump resistor with Zener diode

Fig. 2.10. Suppression resistor (R-dump) converters (only one phase of the motor shown)

Bifilar Winding Converter [18]-[19]: This converter has one transistor and one diode per phase hence employing the single-switch-per-phase (SSPP) configuration (Fig.2.11). The

converter regenerates the stored magnetic energy to the source. This is achieved by having a bifilar winding with opposite polarity between primary and secondary bifilar winding for each phase. The voltage reflected into the main winding is dependent upon the turns ratio of the windings. Although this converter employs a SSPP configuration, a significant drawback of this converter is that the voltage stress seen by the switch is very high and the motor require a bifilar winding.

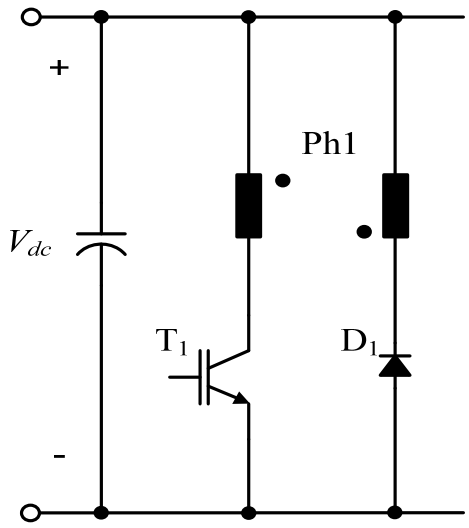

Fig.2.11. Bifilar converter

Split dc Supply Converter [10],[25]

This topology also preserves one switch per phase. As shown in Fig. 2.12, It has two dc capacitors, splitting the dc link. The voltage available for each capacitor is half the full dc link voltage. This converter has drawbacks of having half the dc supply voltage, $V_{dc}/2$ applied to the motor winding and voltage asymmetry between two dc link capacitors. Balancing the charge across the dc link capacitors is very important; the number of machine phases has to be even and not odd. Another drawback of this converter is that freewheeling mode is not possible with this converter. A modified version of this converter is called "Split ac supply" which utilizes the half-bridge rectifier, and the dc link mid-point is tied to ac supply neutral thus splitting ac supply. Therefore, each dc link capacitor is charged at every alternate half cycle of the supply voltage and the capacitor voltage applied to the phase winding is V_{dc} instead of $V_{dc}/2$.

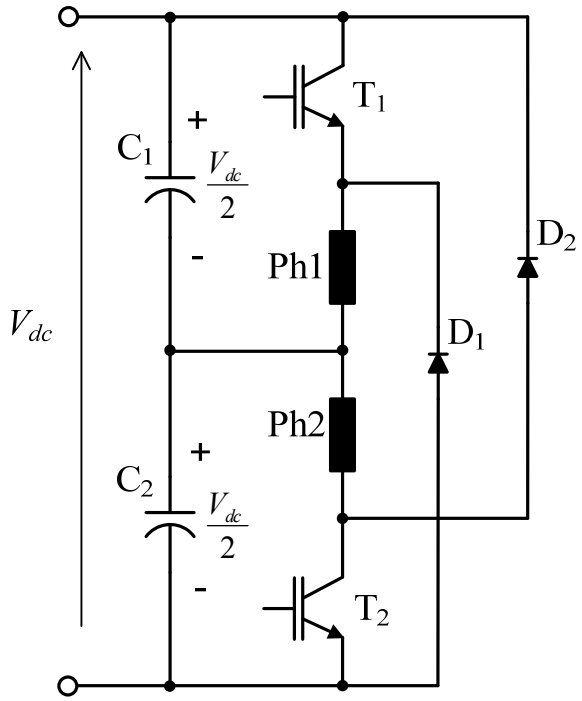

Fig.2.12. Split dc supply converter for two-phase SRM

2.2.2 Classification based on the Energy Recovery

One of the distinguishing factors for the existing converters is the management of the energy stored in the magnetic field of the phase winding and its impact on the efficiency of the drive [15]. Thus, based on how the stored magnetic energy is handled, the converters can be classified into two main groups: 1) Converters with energy dissipation, 2) Converters with energy recovery as shown in Fig. 2.13. In the converters of the first group, the stored energy from each phase winding is simply dissipated, whereas in the converters in the second group, the stored energy is recovered via auxiliary winding or capacitor, then the energy is either returned to the dc supply or used for excitation of other phase winding.

2.2.2.1 Energy Dissipative Converters

The converter in this group, the stored energy is dissipated in a resistor and/or a zener diode as discussed in the above section. The converter configurations are simple as they contain only one switch per phase. The major drawback of this topology is that the energy is simply dumped

during each commutation process resulting in a low efficiency converter. However, this inefficiency is more than compensated by their simplicity, low cost and low component count.

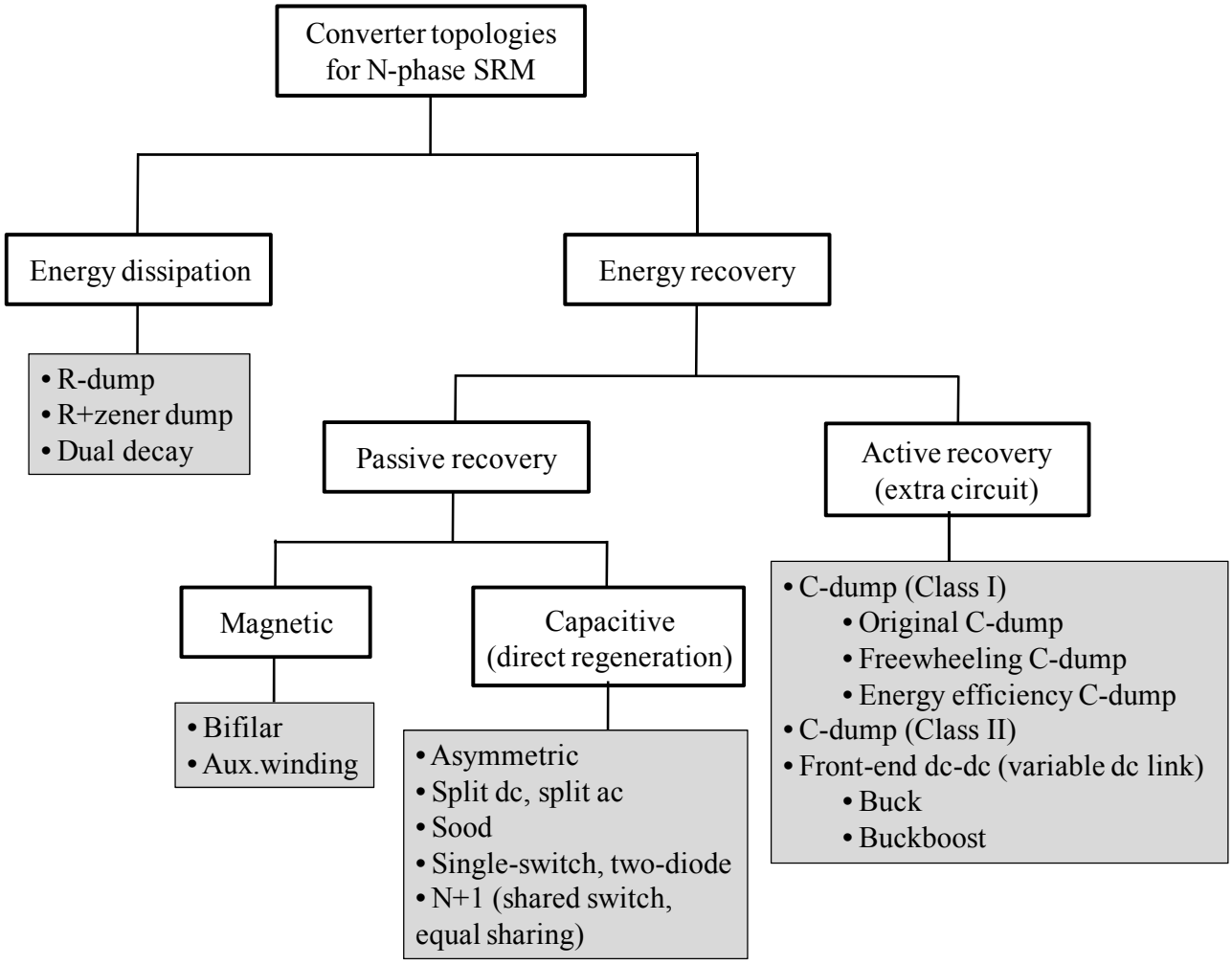

Fig.2.13. Classification of the SRM converters based on energy recovery

2.2.2.2 Energy Recovery (Regeneration) Converters

As shown in Fig.2.13, the converters in this group are divided into two categories: 1) passive recovery, 2) active recovery converters. The passive recovery converters can be further split into two groups: i) magnetic regeneration – The converters in which the energy is regenerated via bifilar windings or auxiliary windings and then is returned to the source, ii)

capacitive regeneration – The converters in which the stored energy is regenerated via the boost or storage converter or directly to the dc link capacitor. Active recovery converters with integrated dc–dc energy recovery circuits transfer energy stored in the magnetic field of the phase winding to an auxiliary capacitor. A dc–dc converter is used to transfer energy from the auxiliary capacitor of the system and ensure that no capacitor becomes under or overcharged. The disadvantages of these converters are control complexity and extra components required for the chopper circuit, leading to increased cost and size. The power semiconductor devices must be rated for the boost voltage. The active recovery converters can be further classified into two categories: C-dump converters and variable dc link converters.

C-dump Converter – Class I [20],[27],[28]: The original C-dump converter and other variants of this topology are shown in Fig. 2.14. The stored magnetic energy is partially diverted to the dump capacitor and recovered from it by the single quadrant chopper and sent to the dc source. The main disadvantage of this circuit is that the current commutation is limited by the difference between voltage across dump capacitor, output voltage, and the dc link voltage. Fast commutation of currents requires high voltage, which results in increasing the voltage rating of the power devices. Further, the energy circulating in spite of the advantages of full regenerative capability and faster demagnetization, the regenerative C-dump converter has disadvantages of complicated control and extra cost for additional components making this converter less competitive for low cost application. Even though this converter uses a fewer number of devices, the circulating energy in the chopper circuit is a large fraction of the total throughput. Therefore, chopper components are not small and the losses in these components reduce the efficiency of the converter.

C-dump Converter – Class II [13],[17],[29]: The auxiliary inductance might be replaced by a motor phase, so that instead of recovered energy from all motor phases being circulated back to dc link capacitor through a chopper circuit the recovered energy can be used to energize the remaining phases of the SRM; hence all or part of recovered energy is retained with the machine, leading to higher efficiency compared to conventional C-dump converters. Fig. 2.15 shows two types of converters which fall in this category.

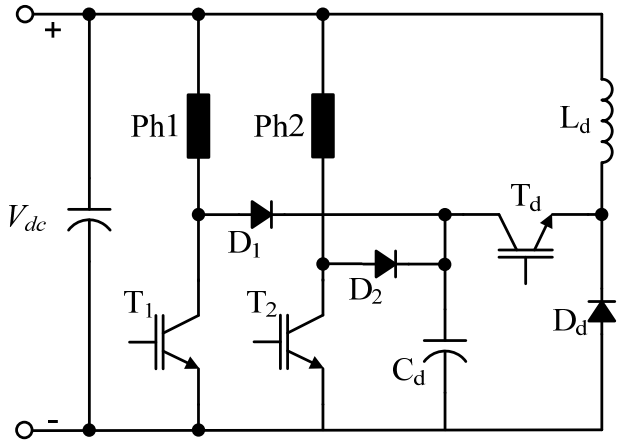

(a) Original C-dump converter

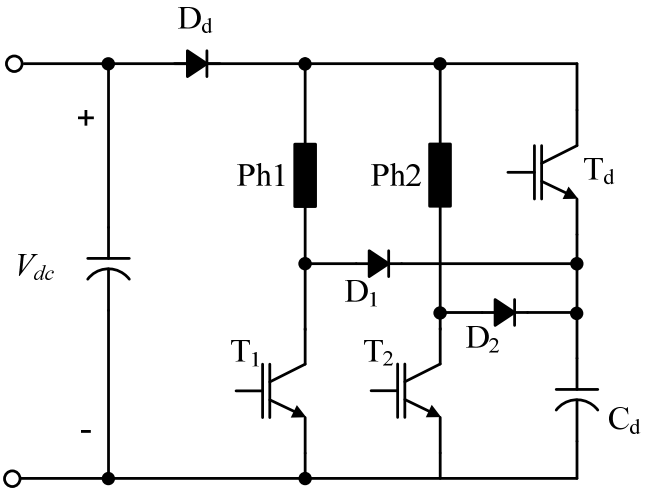

(b) Freewheeling C-dump converter (without auxiliary inductor)

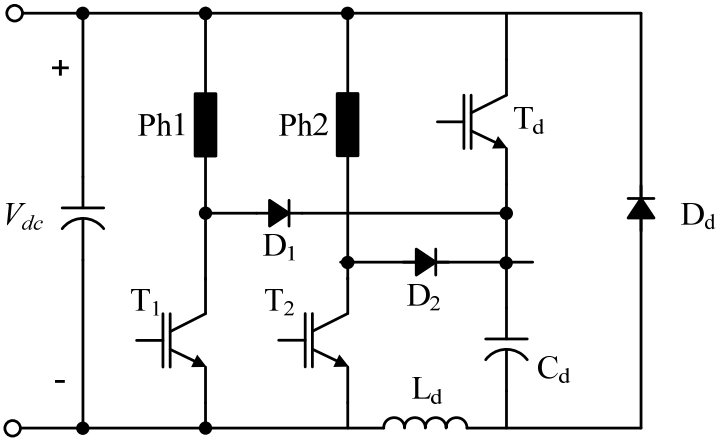

(c) Energy-efficient C-dump converter

Fig. 2.14. C-dump converters with the stored energy circulated to dc link (class I)

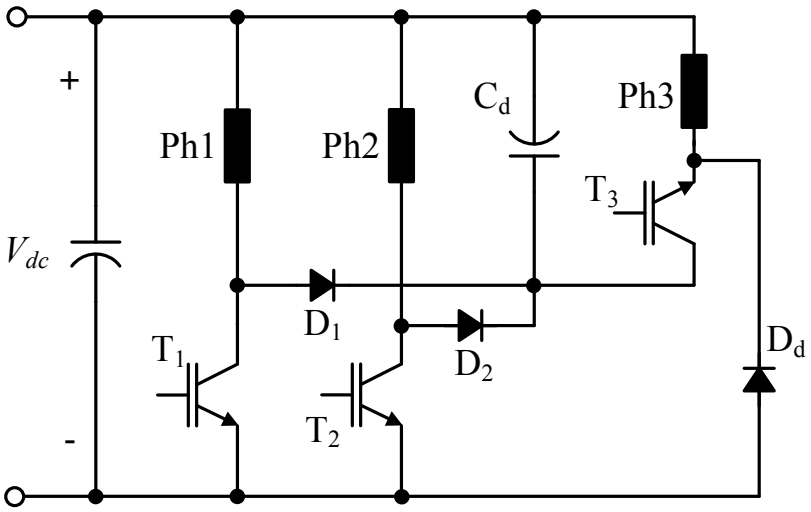

(a) Type 1

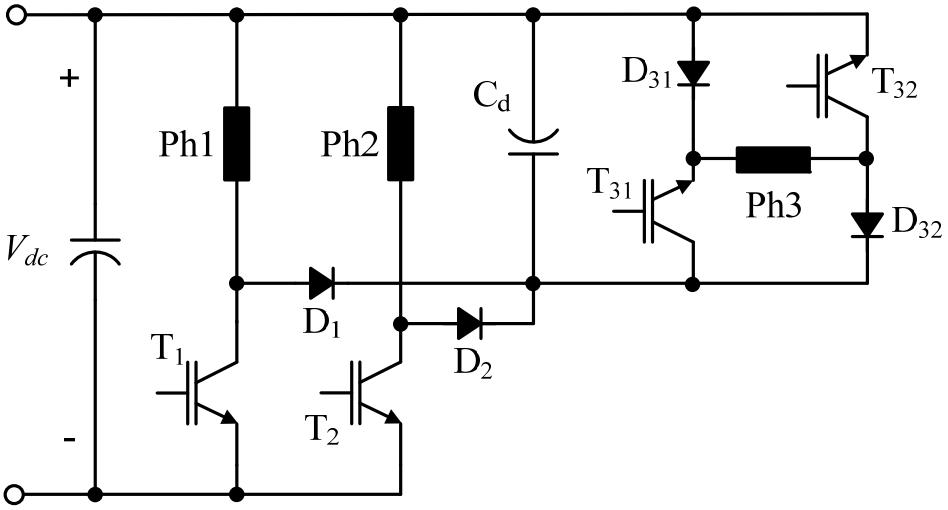

(b) Type 2

Fig.2.15. C-dump converters with the auxiliary inductor replaced by the phase winding (class II)
(Recovered energy is used to energize the remaining phase.)

Variable dc link converter with an integrated dc-dc converter [10],[13]: The converters in this category employ the single-switch-per-phase configuration with an integrated dc-dc buck or buckboost converter at the front-end and thus, the variable dc link voltage is achievable. For an N phase SRM, only N+1 switches and diodes are required but unlike the shared switch N+1 converter, independent operation of the machine phases is guaranteed. These converters are also applicable to half-wave controlled PM brushless dc motor drives which make them attractive for creating a set of universal converter drives for a line of variable speed drives [10].

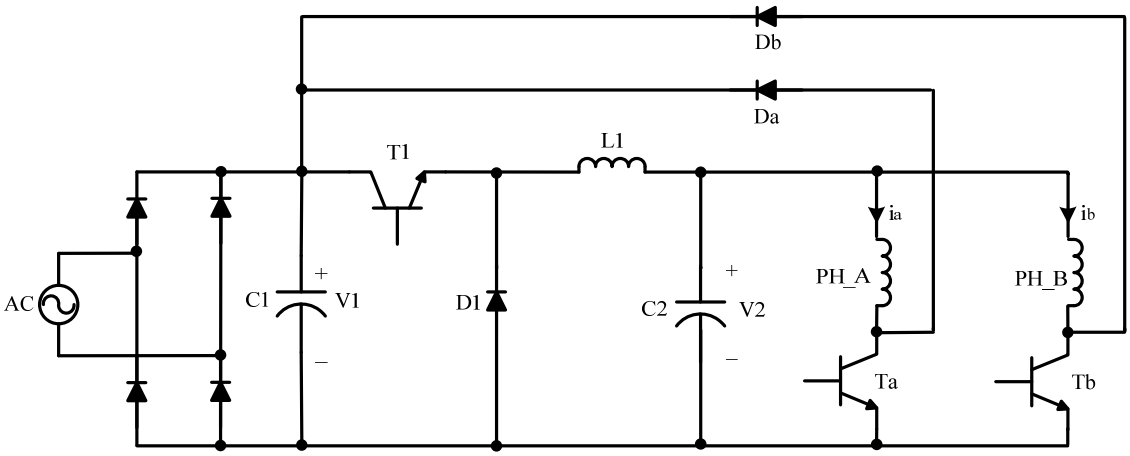

Fig. 2.16. Variable dc link front-end buck converter

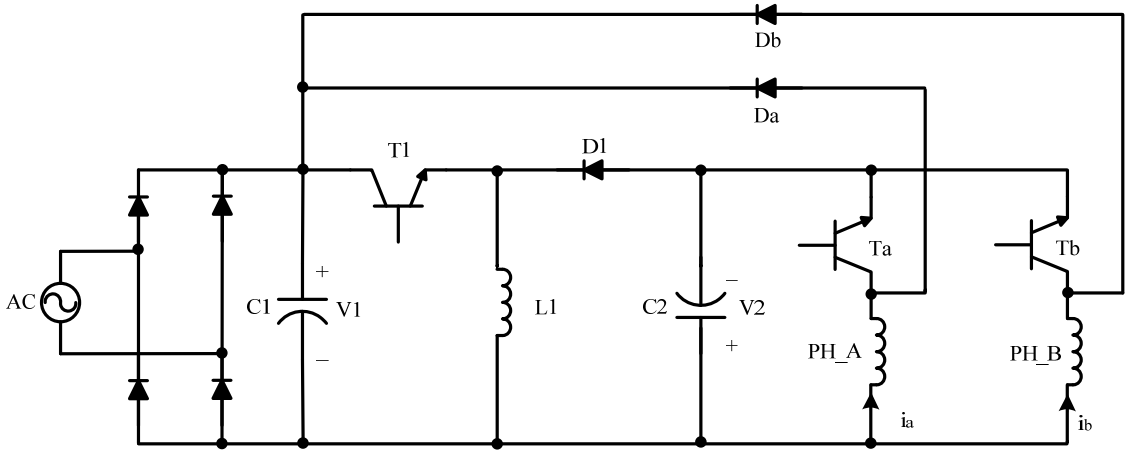

Fig. 2.17. Variable dc link front-end buckboost converter

Chapter 3

Proposed Drive System 1: Single-Controllable-Switch-Based SRM Drive

3.1 Introduction

A new low-cost, brushless variable-speed drive requiring only a single controllable switch is presented in this chapter. The proposed converter (referred to as new single-switch converter) overcomes the drawback of the original single-switch-based four-quadrant motor drive [30], [31] in terms of recovery energy circulation. The drive system is realized using an asymmetric two-phase switched reluctance motor (SRM) and the proposed converter. The new converter (Fig.3.2) invention [32] presented in this paper belong to a class of single switch converters as the original converter but with a fundamental difference that lies in recovered energy circulation. In the original converter, the recovered energy from the main winding stored in the recovery capacitor is circulated back to the dc link capacitor, whereas in the new converter, the recovered energy from the main winding is retained and utilized within the motor instead of being returned to the source. The energy circulation between the motor and source can cause extra losses and result in a need for a larger dc link capacitor and its reduced lifetime. In the previous studies, commutation problem and design optimization were not clearly addressed and therefore negative torque production due to continuous commutation of main phase affecting the system efficiency was the major drawback. A modification of the existing topology in terms of capacitor size as well as machine configuration can bring better current commutation and hence better efficiency.

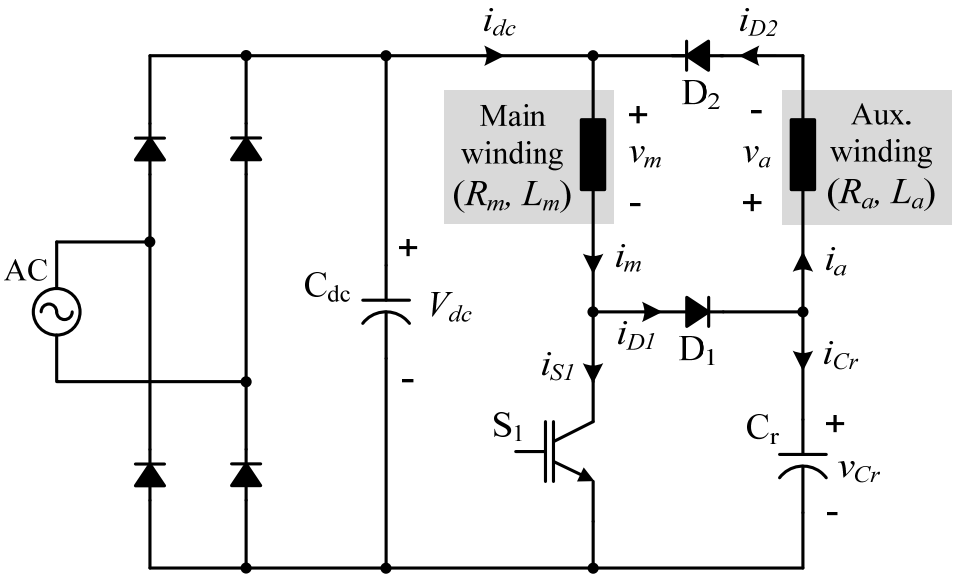

Fig. 3.1. Original single-controllable-switch converter

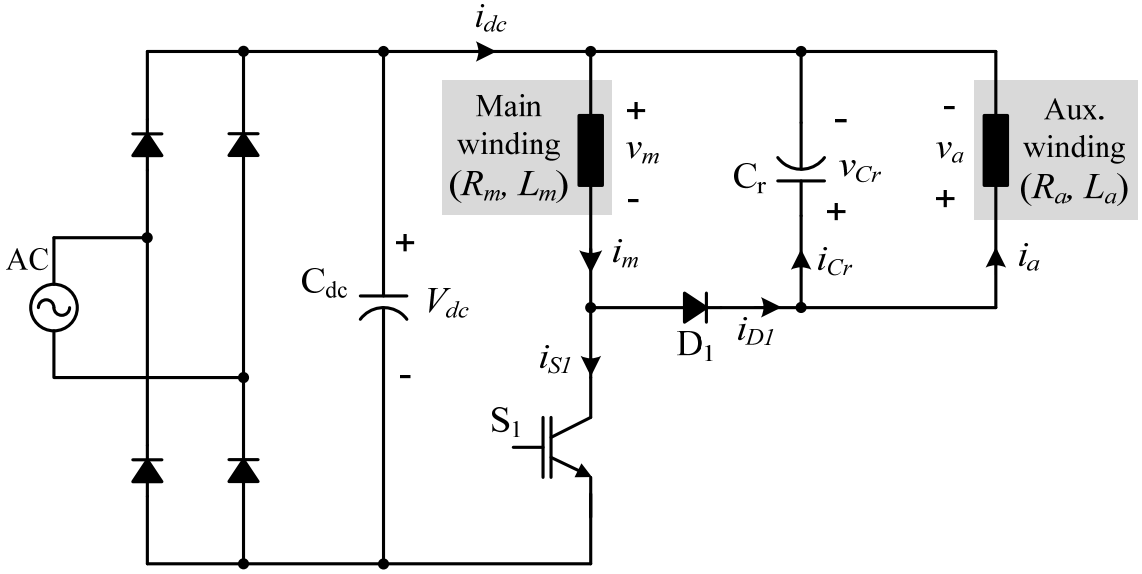

Fig. 3.2. New single-controllable-switch converter

The new single-switch converter has the advantage over the previous converter in term of less capacitor rating while preserving all the advantages of the original circuit is proposed. The key design aspects of the converter as well as optimal commutation strategy are presented. The new drive system retains the unique features of self-starting for all rotor position and four quadrant operation of the original single-switch-based switched reluctance motor drive system.

This chapter paper presents the operation principle and modeling of the new converter coupled with the considered motor, the design consideration for optimal commutation in single-pulse mode, and comparison with other conventional converters and the original converter. Simulation results are based on a nonlinear model of the motor drive system. A prototype drive has been built and tested to verify its practical viability. The experimental results correlate well with the simulation, and demonstrate a performance comparable to conventional asymmetric bridge converter based drive with two switches per phase. The market relevance of this new drive system is primarily due to its lowest cost structure, packaging compactness, self-starting feature, variable-speed operation and four-quadrant capability. Because of these features, the new drive system offers a viable alternative for conventional fixed speed brush-commutator motors and variable- speed permanent magnet brushless dc motor drives in many high volume applications in the low-cost, energy efficient, high-volume categories such as fans, blowers, hand tools and home appliances.

3.2 Proposed Drive System

3.2.1 Asymmetric 8/4 SRM Configuration

Figs. 3.3(a) and 3.3(b) show the configuration of the SRM along with the stator windings, employed in the proposed drive system. The motor has a unique structure such that it has eight salient poles (four main and four auxiliary) on its stator and four salient poles on its rotor, hence referred to as asymmetric two-phase 8/4 SRM. Four large poles with series connected windings form a main phase and two sets of diagonally opposite small poles with the series–connected windings form two auxiliary phases. The stator inner diameter and the back iron diameter are 74.5 mm (2.933 in) ands 102 mm (4.016 in) respectively. The outer stator width is 75 mm (2.953 in)

and the rotor outer diameter is 73.8 mm (2.906 in). The rotor poles are slightly larger with a width of 26.5 mm (1.043 in) and a radius of curvature of 40 degrees. The rotor stack length is 18 mm (0.709 in). The rotor shaft diameter is 6.25 mm (0.246 in). The case of the machine is square with a side length of 135 mm (5.315 in). The stack length is 10 millimeters (0.394 in). While this motor has two phases, they are not identical. The main phase produces most of the torque in the machine, whereas the auxiliary phase is mainly intended for energy recovery for commutation of the main phase current and also aids in self-starting and speed reversal for four-quadrant operation. The reliable self-starting is achieved by supplying the auxiliary windings with a small pulsed current that will pull the nearest rotor poles to complete alignment with the auxiliary poles. Note that in this position the rotor poles are completely unaligned with respect to the main stator poles. Then excitation of the main stator poles at this time will generate an air gap torque turning the rotor. The pole size and number of turns for each phase are optimized for the cost and performance of the drive system. In the current experimental system, only one set of diametrically opposite auxiliary windings are utilized. This reduces the machine into an equivalent of a two phase SRM. The motor is designed to run at a rated speed of 5000 r/min and maximum speed of 10,000 r/min. The parameters and specification for this motor are available in Appendix A.

The major features of the proposed machine include:

- Provides starting capability in both directions unlike other single-phase SRM configurations and, therefore, this is the only single-phase configuration capable of four-quadrant operation.
- Does not use permanent magnets thus reducing the manufacturing complexity and cost
- The auxiliary pole windings can be used, in addition to self-starting, for probing to determine the rotor position or as an inactive phase.
- After starting, the auxiliary poles need not be used for continuous operation of the machine as the main winding itself, and can be used for sensing the rotor position.
- Since the interpole winding is only used for a small amount of time (during starting), it can be designed to have a very small volume of copper thereby reducing its cost. During the sensing part of the cycle, its current is very small even if its duty cycle is high and, therefore, a small copper volume design is adequate.

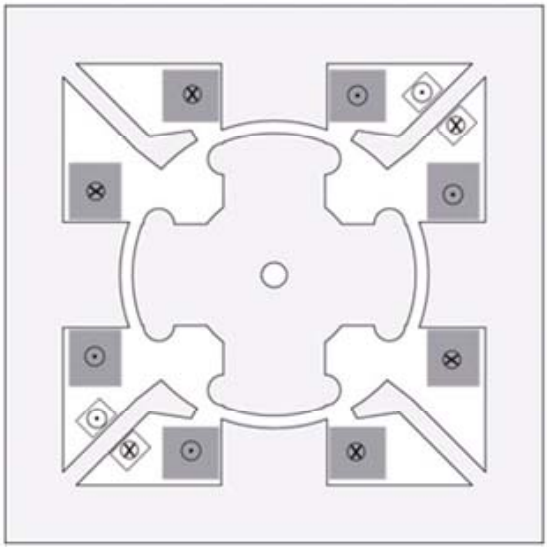

(a)

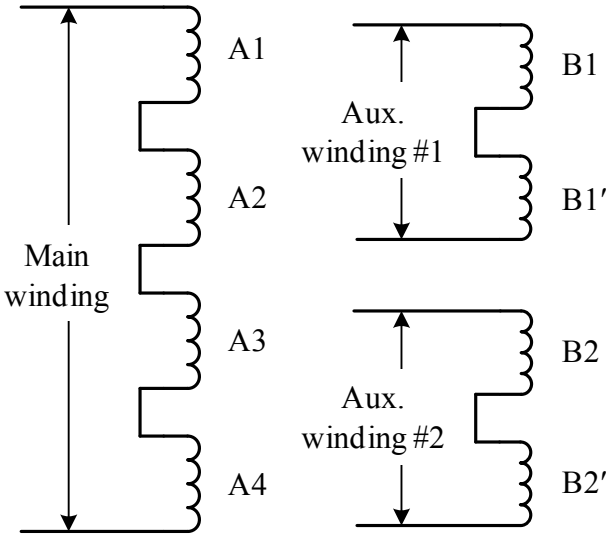

(b)

Fig. 3.3. Asymmetric 8/4 SRM. (a) Stator and rotor lamination and (b) phase winding configuration

3.2.2 Asymmetric 8/4 SRM Model Characterizations

The SRM is a highly nonlinear system. The nonlinear theory describing the behavior of the motor has been developed. Based on the theory, a mathematical model can be created. On one hand it enables simulation of the SRM system and, on the other hand, development and implementation of sophisticated algorithms for controlling the SRM is feasible. The electromagnetic circuit of the SRM is characterized by non-linear magnetization. Thus, for analysis, simulation, and control of the proposed drive system, the nonlinear electromagnetic characteristics of the motor are obtained using two-dimensional finite element analysis (FEA).

The magnetization characteristics, inductance profiles, and torque profiles for each phase at some different current levels are shown in Figs. 3.4, 3.5, and 3.6, respectively. The flux lines for the main phase with 4A excitation and those for the auxiliary phase with 1A excitation are also plotted in Fig. 3.7. Fig. 3.4 illustrates a magnetization characteristic for the proposed SRM. It is a function between the magnetic flux linkage, the phase current, and the rotor position. The magnetization characteristic curve defines the nonlinearity of the motor. The influence of the phase current is most apparent in the aligned position, where saturation effects can be observed. The inductance profiles for both main and auxiliary phase at different excitation currents are plotted over a commutation cycle in Fig. 3.5(a) and 3.5(b) respectively. The torque generated by the motor phase is a function of the magnetic flux. Hence, the phase torque is not constant for constant phase current for different rotor positions resulting as shown in Fig. 3.6.

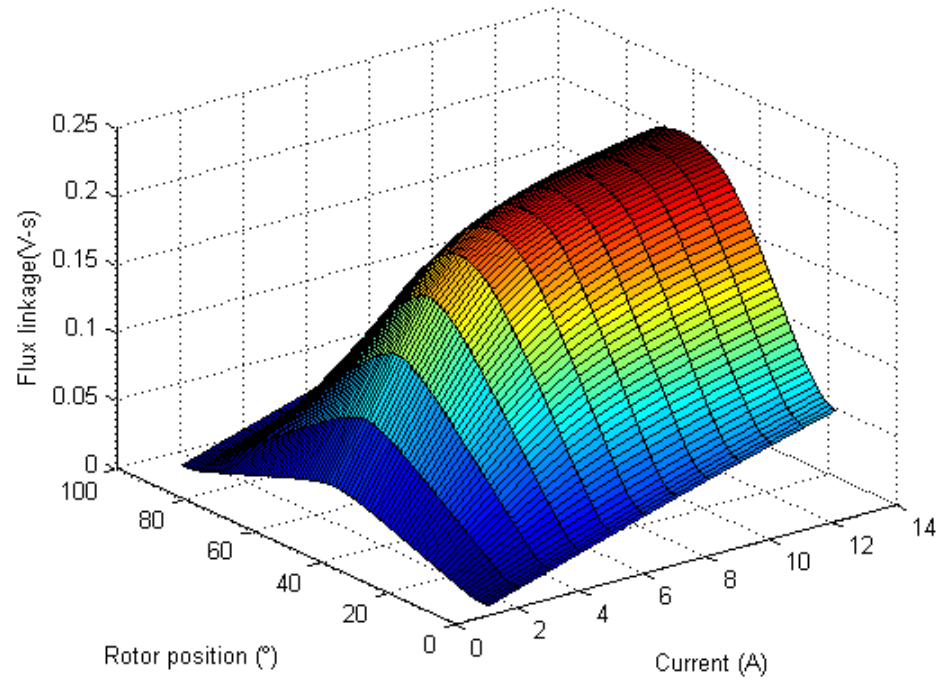

(a) Main phase

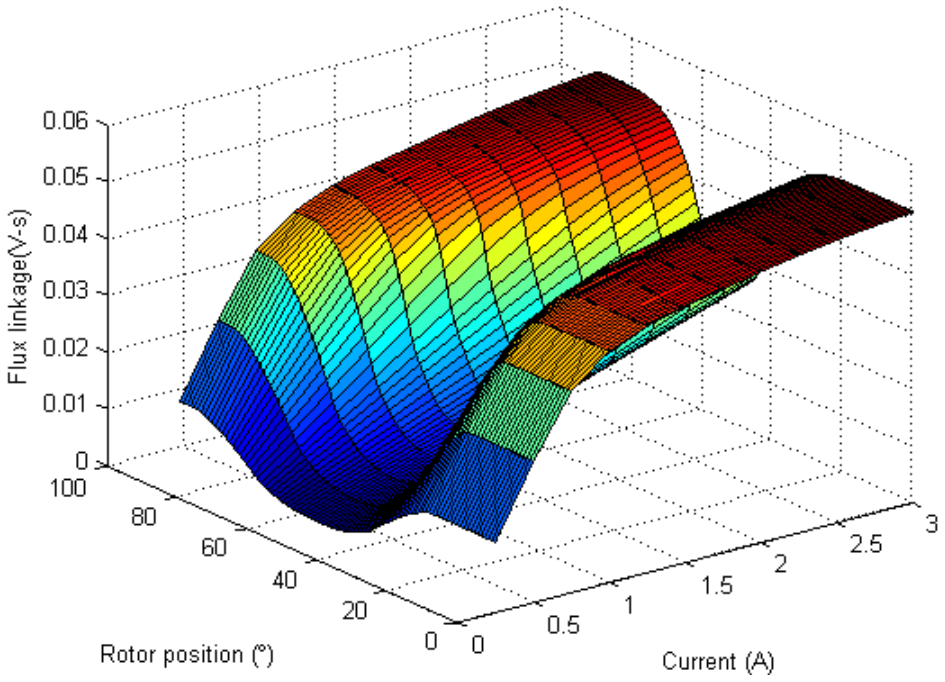

(b) Auxiliary phase

Fig. 3.4. Magnetization characteristics for the asymmetric two-phase SRM obtained from two-dimensional finite element analysis (FEA) simulation

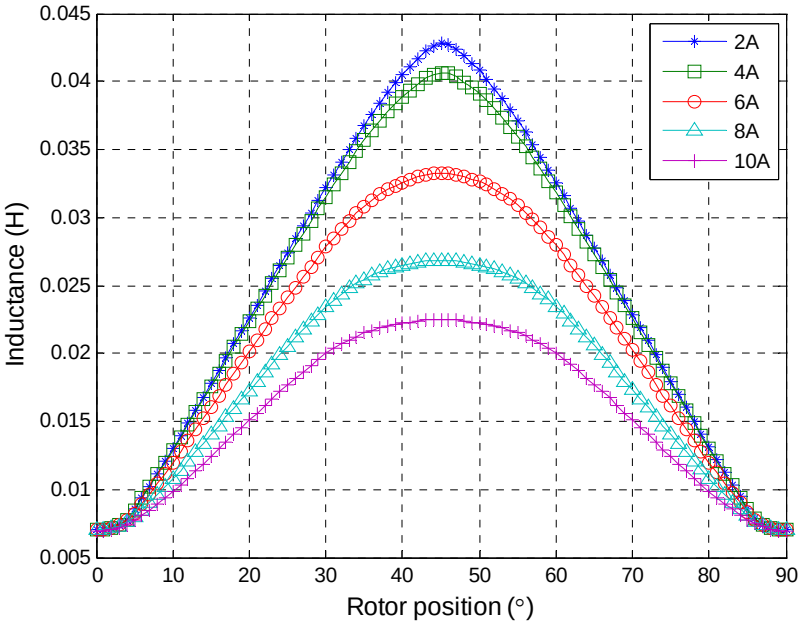

(a) Main phase

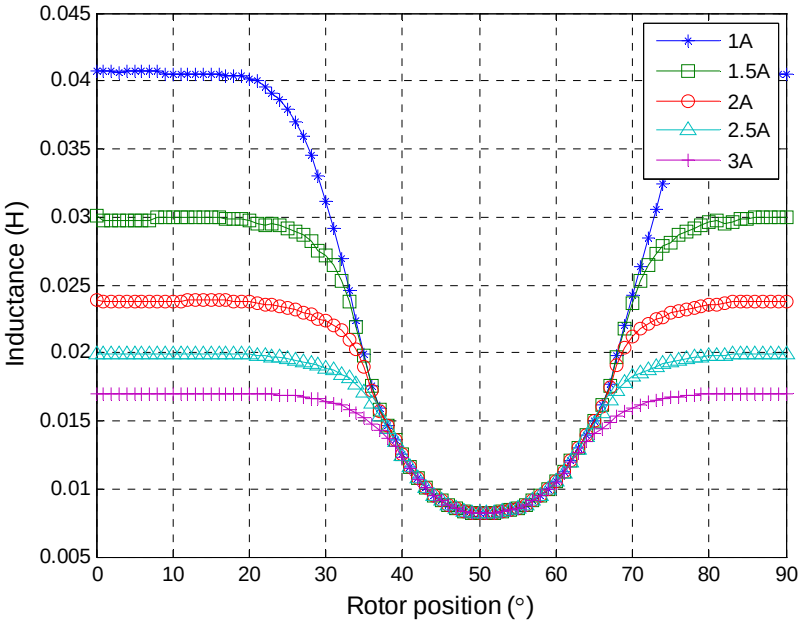

(b) Auxiliary phase

Fig. 3.5. Inductance for the two-phase 444 SRM obtained from two-dimensional finite element analysis (FEA) simulation

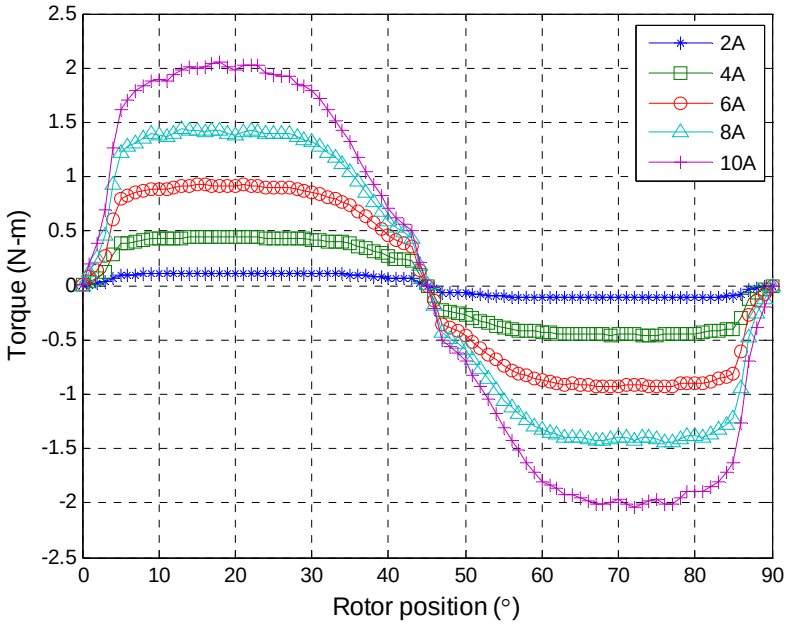

(a) Main phase

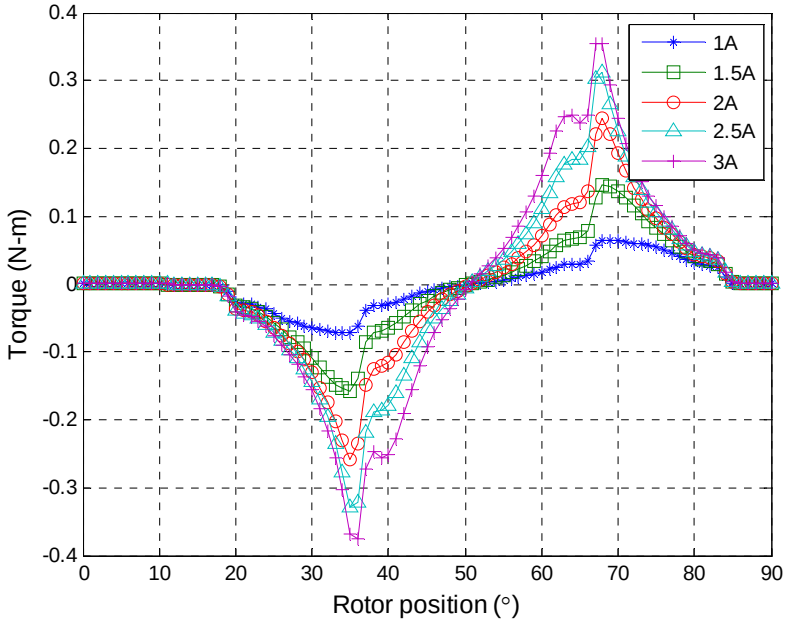

(b) Auxiliary phase

Fig. 3.6. Torque for the two-phase 444 SRM obtained from two-dimensional finite element analysis (FEA) simulation

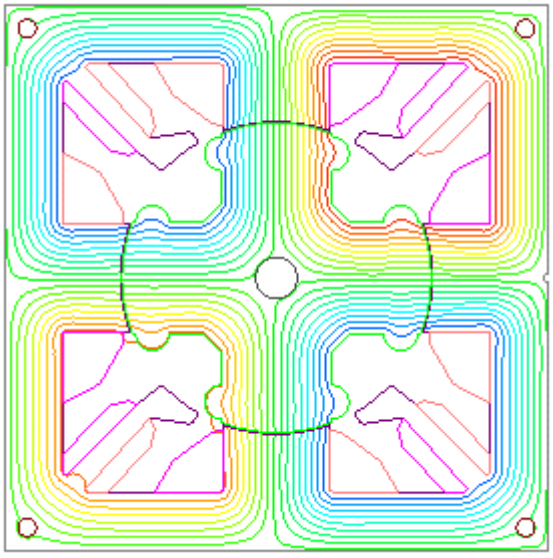

(a) Flux line of the main phase energized with 4A excitation at aligned position

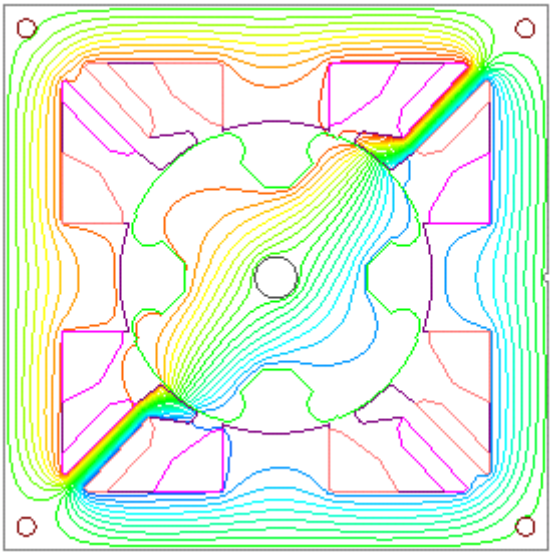

(b) Flux lines of the auxiliary phase energized with 1A excitation at aligned position

Fig. 3.7. Flux lines for main and auxiliary phase at aligned positions

3.2.3 Power Converter

The key features of the proposed converter are described as follows.

1) The converter has only one controllable switch and one diode total, making the drive electronics very compact and inexpensive and thus requiring little PCB footprint.
2) A bridge rectifier with a filter capacitor C_{dc} forms a dc link to supply energy to the main phase winding.
3) Isolation for the gate drive circuit can be avoided since the switch S1 is tied with the negative dc rail.
4) For low-performance deployment, a resistive current sensor can be employed between the switch S_1 and negative dc rail, hence eliminating the need for high cost sensors with galvanic isolation.
5) The converters are inherently suited for two-phase SRMs having asymmetric stator phases to realize self- starting as well as speed reversal.
6) The recovery capacitor, C_r along with the auxiliary winding, is for handling recovery energy from the main phase. During the commutation of the main phase current, the current flows to charge C_r and to a small extent goes through the auxiliary winding.
7) During the main phase commutation, in the original converter shown in Fig. 3.1, $-(v_{Cr} - V_{dc})$ appears across the main winding resulting in the capacitor voltage v_{Cr} being maintained in the range of 1.5-2 times V_{dc}; however, in the new converter, the voltage across the main winding equals $-v_{Cr}$, resulting in v_{Cr} being much less than V_{dc} .
8) In the original converter, the recovered energy stored in the capacitor C_r is returned back to the dc link capacitor and this energy exchange between the motor and source causes extra losses leading to a larger dc link capacitor and active devices' rating. In the new converter, however, the recovered energy is retained and utilized within the motor windings instead of being returned to the source.
9) Commutation time, a critical operation/control variable, is dependent on the size of the recovery capacitor as well as the parameters of the main and auxiliary phases, as both phases are tightly coupled along with the capacitor C_r during the commutation. Therefore, optimal selection of C_r as well as auxiliary winding parameters is of prime importance for successful commutation of each phase current.

3.3 Derivation of Drive System Equations

Drive system equations to model the operation of the converter combined with the machine are derived in this section. The analytic modeling of each converter is obtained based on the switching state of the controller switch, S_1. Two sets of state equations for each converter can be derived as below. Note that the dc link and the power devices are assumed to be ideal; hence, the dc link voltage is constant and the device voltage drops are ignored.

When the switch S_1 is turned on, the state equations for main and auxiliary phases as well as the capacitor C_r are given by

$$\frac{d\lambda_m}{dt} = V_{dc} - R_m i_m \tag{3.1}$$

$$\frac{d\lambda_a}{dt} = v_{Cr} - R_a i_a \tag{3.2}$$

$$\frac{dv_{Cr}}{dt} = \frac{i_{Cr}}{C_r} = \frac{-i_a}{C_r} \tag{3.3}$$

where λ_m and λ_a are the main and auxiliary phase flux linkages, i_m and i_a are main and auxiliary phase currents, R_m and R_a are the main and auxiliary phase resistances, V_{dc} and v_{Cr} are the dc link and the capacitor C_r voltages, respectively. Likewise, when the switch S_1 is turned off, the state equations for main and auxiliary phases as well as the capacitor C_r voltage are given by

$$\frac{d\lambda_m}{dt} = -v_{Cr} - R_m i_m \tag{3.4}$$

$$\frac{d\lambda_a}{dt} = v_{Cr} - R_a i_a \tag{3.5}$$

$$\frac{dv_{Cr}}{dt} = \frac{i_{Cr}}{C_r} = \frac{i_m - i_a}{C_r} \tag{3.6}$$

Therefore, the state equations using the switching function, S for the switch S_1 (S= 0(off) or S =1(on)) are given by

$$\frac{d\lambda_m}{dt} = \overbrace{S\left(V_{dc} - R_m i_m\right)}^{S_1\ ON} + \overbrace{\left(1-S\right)\left(-v_{Cr} - R_m i_m\right)}^{S_1\ OFF} = SV_{dc} - (1-S)v_{Cr} - R_m i_m \tag{3.7}$$

$$\frac{d\lambda_a}{dt} = \overbrace{S\left(v_{Cr} - R_a i_a\right)}^{S_1\ ON} + \overbrace{\left(1-S\right)\left(v_{Cr} - R_a i_a\right)}^{S_1\ OFF} = v_{Cr} - R_a i_a \tag{3.8}$$

$$\frac{dv_{Cr}}{dt} = \frac{i_{Cr}}{C_r} = \frac{\overbrace{S\left(-i_a\right)}^{S_1\ ON} + \overbrace{\left(1-S\right)\left(i_m - i_a\right)}^{S_1\ OFF}}{C_r} = \frac{(1-S)i_m - i_a}{C_r} \tag{3.9}$$

where the obtained phase currents and the switching function of S_1 (= 0(off) or =1(on)),

The phase currents can be obtained from a lookup table of flux-current-position (λ–i–θ) data along with flux linkage calculated by solving (3.7) and (3.8). From the obtained phase currents, the currents flowing through the switch (i_{S1}), diode (i_{D1}), and dc link (i_{dc}) are also derived using the switching function, S by

$$i_{S1} = Si_m \tag{3.10}$$

$$i_{D1} = \left(1 - S_1\right)i_m \tag{3.11}$$

$$i_{dc} = i_{S1} = Si_m \tag{3.12}$$

The load dynamic equation of the motor is also given by

$$\frac{d\omega_r}{dt} = \frac{T_e - B\omega_r - T_L}{J} \tag{3.13}$$

where ω_r, T_e, B, J, and T_L are the rotor speed, electromagnetic torque, friction coefficient, rotor and load inertia, and load torque, respectively.

3.4 Converter Modes of Operation

Proper understanding of the operation of the converter coupled with the motor is crucial to design and control of the drive system. Although the converter topology looks simple, their operation may not be straight forward due to the tight coupling among the main winding, capacitor C_r, and auxiliary winding during the operation. From evaluation of all the possible combinations of the switching states of the switch and the diode, as well as the phase current commutation, five meaningful modes of operations emerge as illustrated in Fig. 3.8. Descriptions for each mode are discussed as follows and summarized in Table 3.1.

Mode 1: When the switch S_1 is turned on, the main winding is energized with energy from the dc link. The auxiliary winding is also energized from the capacitor C_r if there is a charge in C_r.

Mode 2: When S_1 is still turned on, the main winding continues to be energized. If C_r is completely discharged, then there is no current flow between C_r and the auxiliary winding.

Mode 3: When S_1 is turned off, the current in main winding flows through D_1 and C_r as well as the auxiliary phase, hence transferring energy in part to C_r and in part to auxiliary winding.

Mode 4: When S_1 is turned off, both the main winding current and C_r supply the auxiliary winding.

Mode 5: When the switch S_1 is turned off, and the main winding is successfully commutated, and C_r exclusively supplies the auxiliary winding current.

Table 3.1. Summary of Modes of operation for the new single-switch converter

Mode	S1	D1	i_{dc}	i_m	i_a	i_{Cr}	v_m	v_a
1	On	Off	> 0	> 0	> 0	< 0	V_{dc}	v_{Cr}
2	On	Off	> 0	> 0	$= 0$	$= 0$	V_{dc}	0
3	Off	On	$= 0$	> 0	> 0	> 0	$-v_{Cr}$	v_{Cr}
4	Off	On	$= 0$	> 0	> 0	< 0	$-v_{Cr}$	v_{Cr}
5	Off	Off	$= 0$	$= 0$	> 0	< 0	$-v_{Cr}$	v_{Cr}

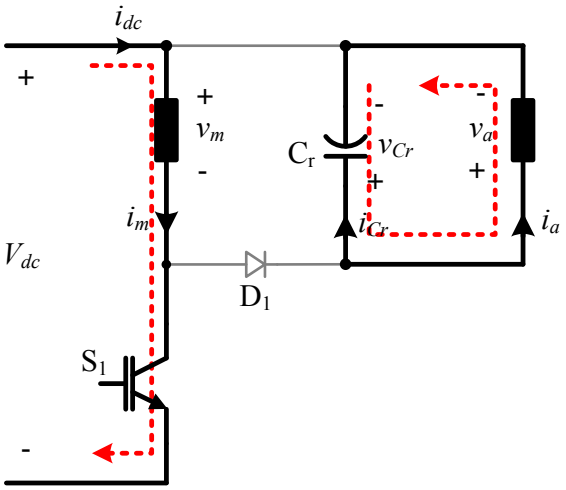

(a) Mode 1

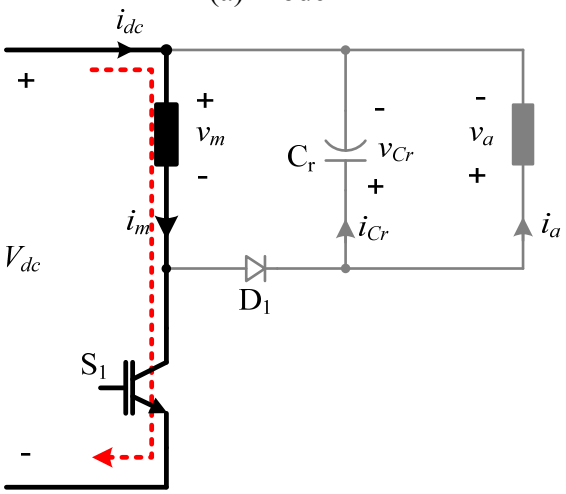

(b) Mode 2

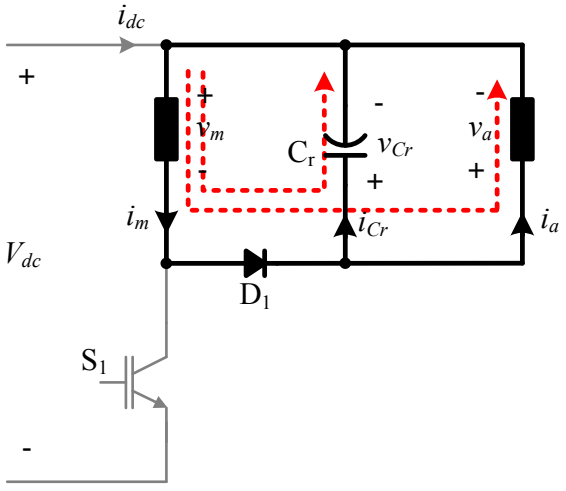

(c) Mode 3

Fig. 3.8. Converter modes of operation

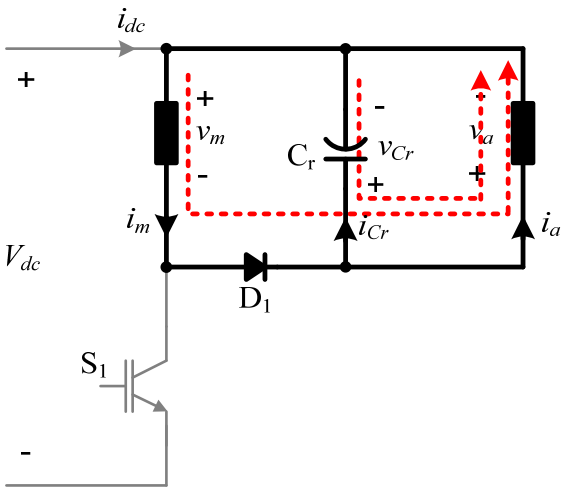

(d) Mode 4

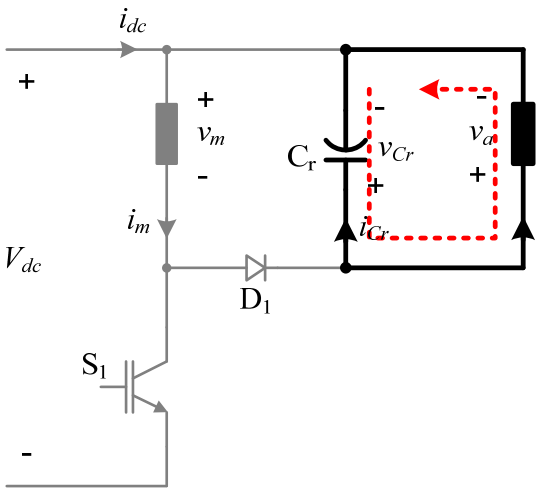

(e) Mode 5

Fig. 3.8. Converter modes of operation - Continued

3.5 Performance Constraints and Design Consideration

The critical performance variables of interest in the design of the converter are the commutation time of the current and the voltage rise in the recovery capacitor C_r due to the energy being transferred between the machine windings and the capacitor. Both of these effects are quantified in this section to assess the control boundaries of the converter and the total drive system and to specify the rating of C_r.

3.5.1 Commutation of Main and Auxiliary Phase Currents

The commutation of the main winding current is achieved through both the recovery capacitor and the auxiliary winding. In PWM operation, the voltage across the main winding switches back and forth between the positive (V_{dc}) and the negative voltage ($-v_{Cr}$). Note that v_{Cr} is not constant throughout the stroke period as it is dependent on the energy transferred from the main winding and the energy drained into the auxiliary winding. The current in the main winding also circulates through the auxiliary winding, transferring energy back and forth between the main and auxiliary winding resulting in continuous conduction of the auxiliary winding current as shown in Fig. 3.9. Although the net torque generated by the auxiliary phase is almost zero, current in the auxiliary winding during the main phase stroke generates negative torque, thus resulting in reduced efficiency and increased acoustic noise. This problem, however, can be obviated if a voltage-fed, single-pulse control is employed. Although finer current control is not achievable with the single-pulse control, this is not a significant drawback since the target low-performance fan type applications do not require finer current control. Furthermore, the motor will run mostly at top speed where single-pulse control is best suited.

The optimal commutation in single-pulse mode is illustrated in Fig. 3.10, which shows the desired waveforms: main and auxiliary winding currents (i_m, i_a), and the voltage of the capacitor C_r (v_{Cr}). Once the switch S_1 is turned off at t_0, the main current flows through both C_r and the auxiliary winding. Thus, v_{Cr} and i_a increases, which corresponds to mode 3. Once C_r is fully charged at t_1, C_r starts being discharged. Thus energy from both main winding and C_r is transferred to the auxiliary winding (mode 4). When the main winding current decays to zero at t_2, it is then only the capacitor that transfers energy to the auxiliary winding (mode 5). Therefore, it is of prime importance to achieve the commutation such that both main and auxiliary winding

currents fall to zero as soon as possible within the current stroke cycle (T_{ph}) to avoid negative torque generation. .

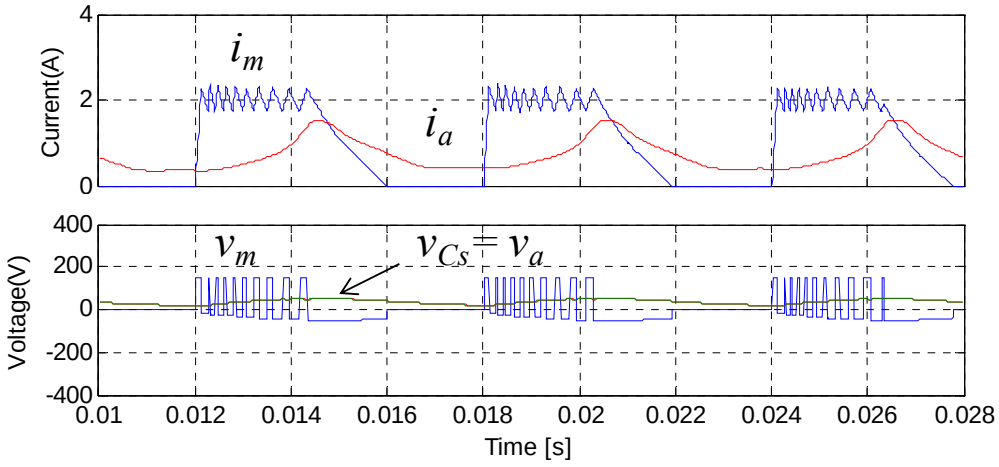

Fig. 3.9. Main and auxiliary current waveforms in PWM chopping mode

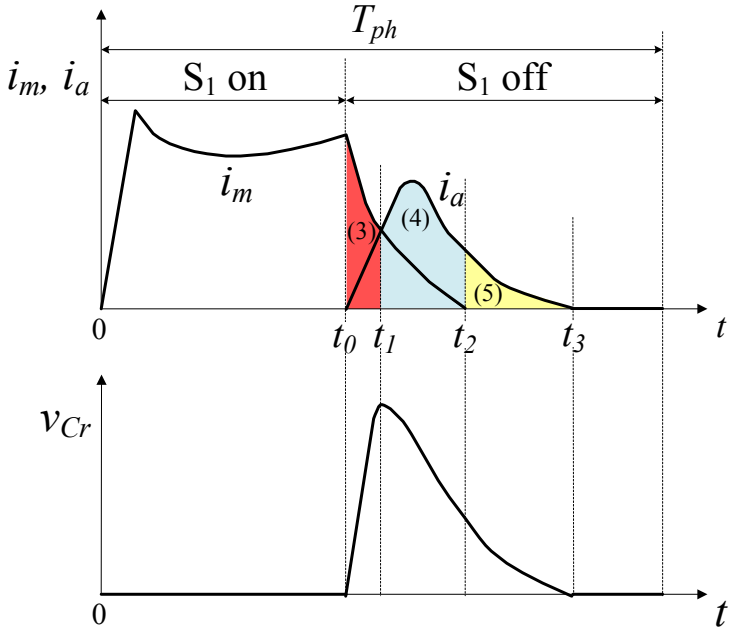

Fig. 3.10. Desired waveforms for the current commutation within a stroke cycle (T_{ph}) in single-pulse mode. (Main and auxiliary winding currents (i_m, i_a), capacitor current (i_{Cr}), capacitor voltage (v_{Cr}))

3.5.2 Design Consideration for Optimal Commutation

The commutation time is highly dependent on the parameters (resistance and inductance) of both main and auxiliary windings as well as the size of C_r. Assuming that the main phase is optimally designed for the machine's power specification, the key design parameters are then the size of C_r and the resistance and inductance of the auxiliary winding, which are determined mainly by the number of turns on a given machine structure. The calculation of the commutation time is as follows. The voltage equation of an SRM phase is expressed as

$$\begin{aligned} v &= R_s + \frac{d\lambda}{di} \\ &= R + \frac{\partial \lambda}{\partial i}\frac{di}{dt} + \frac{\partial \lambda}{\partial \theta}\omega_r \\ &\cong \left(R + \omega_r \frac{dL}{d\theta} \right) i + L\frac{di}{dt} \\ &= R_{eq} i + L\frac{di}{dt} \end{aligned} \tag{3.14}$$

where v, i, R, λ, L, ω_r, and θ_r are phase voltage, phase current, winding resistance, phase flux linkage, phase self-inductance, rotor speed, and rotor position respectively. The equivalent resistance of winding (R_{eq}) consists of the winding resistance and the constant associated with the induced back-EMF of the motor winding at constant speed. Note that the phase flux linkage, $\lambda = L(\theta,i)i$ is a nonlinear function of the phase current and rotor position. During commutation, the converter can be considered as an RLC circuit with the initial conditions. Therefore, the system equations for the equivalent RLC circuit are given by

$$R_{eqm} i_m + L_{eqm}\frac{di_m}{dt} = -v_{Cr} \tag{3.15}$$

$$R_{eqa} i_a + L_a \frac{di_a}{dt} = -v_{Cr} \tag{3.16}$$

$$C_r \frac{dv_{Cr}}{dt} = i_m - i_a \tag{3.17}$$

where R_{eqm} and R_{eqa} are the equivalent resistances for main and auxiliary windings, respectively, and L_m and L_a are the self-inductances of the main and auxiliary windings, respectively. The required commutation times (t_1, t_2, t_3) as well as the peak voltage rise of C_r can be obtained by solving (3.15), (3.16), and (3.17) for $i_m(t)$, $i_a(t)$, and $v_{Cr}(t)$. However, solving the three simultaneous differential equations for an exact expression of i_m(t) is quite cumbersome. Therefore, by examining the piecewise waveforms in Fig.3.10 with an assumption that $i_m \approx i_{Cr}$ during the initial capacitor charging period, (3.15) can be rewritten as

$$R_{eqm} i_m + L_m \frac{di_m}{dt} + \frac{1}{C_r} \int i_m dt = 0 \tag{3.18}$$

Then, the main winding current is derived as

$$i_m(t) = I_{m0} e^{-\alpha t} \cos \beta t + \left(\frac{V_{C0}}{\beta L_m} - \frac{\alpha I_{m0}}{\beta} \right) e^{-\alpha t} \sin \beta t \tag{3.19}$$

where

$$\alpha = \frac{R_{eqm}}{2L_m} \tag{3.20}$$

$$\beta = \sqrt{\frac{1}{L_m C_r} - \left(\frac{R_{eqm}}{2L_m} \right)^2} \tag{3.21}$$

I_{m0} is the initial current in the main winding at the beginning of commutation (t=t_o). During mode 3 region, the equation for the equivalent circuit between t_2 and t_3 can be expressed as

$$R_{eqa} i_a + L_a \frac{di_a}{dt} + \frac{1}{C_r} \int i_a dt + V_{C0} = 0 \tag{3.22}$$

Then, the auxiliary winding current is derived as

$$i_a(t) = I_{a0}e^{-\alpha t}\cos\beta t + \left(\frac{V_{C0}}{\beta L_a} - \frac{\alpha I_{a0}}{\beta}\right)e^{-\alpha t}\sin\beta t \tag{3.23}$$

where

$$\alpha = \frac{R_{eqa}}{2L_a} \tag{3.24}$$

$$\beta = \sqrt{\frac{1}{L_a C_r} - \left(\frac{R_{eqa}}{2L_a}\right)^2} \tag{3.25}$$

I_{a0} is the initial current in the auxiliary winding at the beginning of commutation ($t = t_2$). The current commutation time t_c for each winding current is obtained by solving (3.19) and (3.23) using the conditions that $i_m(t_c)= 0$ and $i_a(t_c) = 0$:

$$t_c = \frac{\pi}{\beta} - \frac{1}{\beta}\tan^{-1}\left(I_{a0}\Big/\left(\frac{V_{C0}}{\beta L_a} - \frac{\alpha I_{a0}}{\beta}\right)\right) \tag{3.26}$$

An approximate equation for C_r voltage is also obtained by solving (3.15), (3.16), and (3.17) for $v_{Cr}(t)$:

$$v_{Cr}(t) = \frac{I_{m0}\alpha + \gamma\beta}{C_r(\alpha^2 + \beta^2)}\left\{1 - e^{-\alpha t}\cos\beta t + \left(\frac{I_{m0}\beta - \gamma\alpha}{\alpha^2 + \beta^2}\right)e^{-\alpha t}\sin\beta t\right\} \tag{3.27}$$

where

$$\alpha = \sqrt{\frac{R_{eqm} + R_{eqa}}{C_r R_{eqa} L_a}} - \frac{R_{eqm}}{L_m} \tag{3.28}$$

$$\beta = \sqrt{\frac{R_{eqm} + R_{eqa}}{C_s R_{eqa} L_a} - \left(\frac{L_m + L_a C_s R_{eqm} R_{eqa}}{2C_s R_{eqa} L_a}\right)^2} - \frac{R_{eqm}}{L_m} \tag{3.29}$$

$$\gamma = \frac{V_{C0}}{\beta L_a} - \frac{\alpha I_{a0}}{\beta} \tag{3.30}$$

The key parameters in the calculation of the commutation time from (3.26) and peak voltage ripple from (3.27) are the equivalent resistance and inductance of the winding and the capacitance of C_r. At constant speed, the equivalent resistance is mainly determined by the inductance slope, which in turn is determined by aligned and unaligned inductances with the rotor pole arc. For the current motor setup, the inductance for the auxiliary phase is varied by changing the number of turns. Therefore, the relationship between the inductance, capacitor, and commutation time as well as the relationship between inductance, capacitor, and voltage ripple are investigated as illustrated in Figs.3.11 and 3.12, respectively. The equivalent inductance is selected by the inductance at aligned position, i.e., at the start of the commutation. The commutation time is normalized by choosing the base time equal to half the stroke period at the maximum speed and the equivalent inductance for the auxiliary phase is normalized by the main phase inductance.

Impact of recovery capacitor size: A smaller capacitance tends to charge and discharge faster with fast commutation and perforce accompanied by higher voltage ripple and possible ringing of the current. The effects of the capacitor size on the commutation time and voltage ripple are also investigated from the simulation as shown in Fig. 3.13 and Fig. 3.14, respectively. Since the smaller capacitor absorbs and drains the energy faster, faster commutation can be achieved. However, highly pulsating voltage increases voltage rating of the capacitor. When the size of C_r increases, the machine current and capacitor voltage smooth out but the available commutation voltage decreases. There, considering these trade-offs, the optimal capacitor size should be determined.

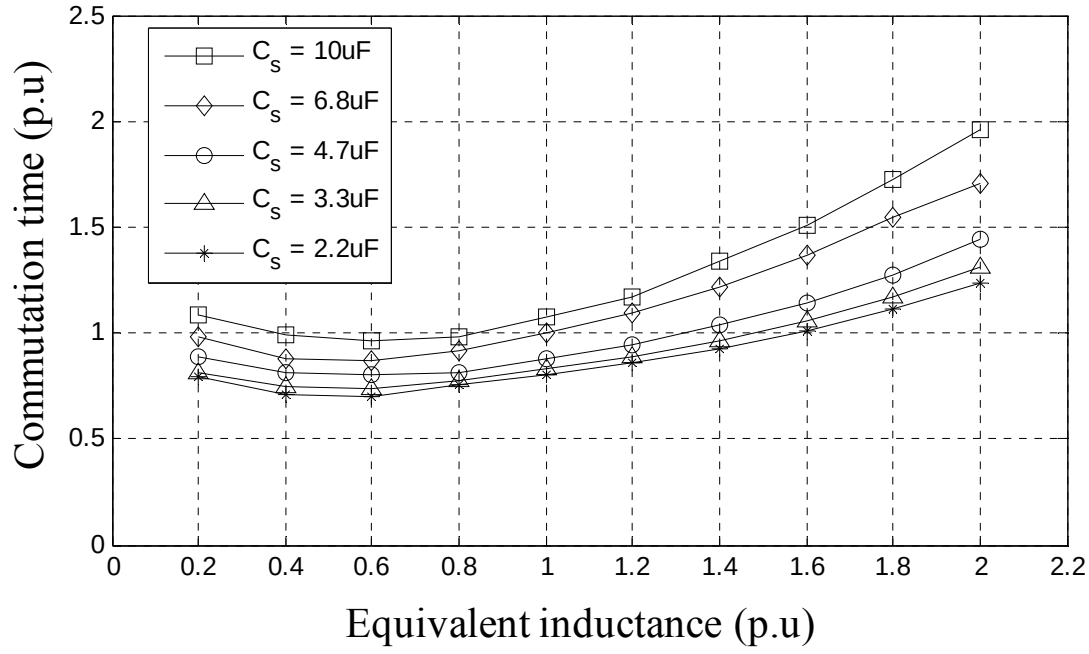

Fig. 3.11. Commutation time vs. capacitance vs. inductance

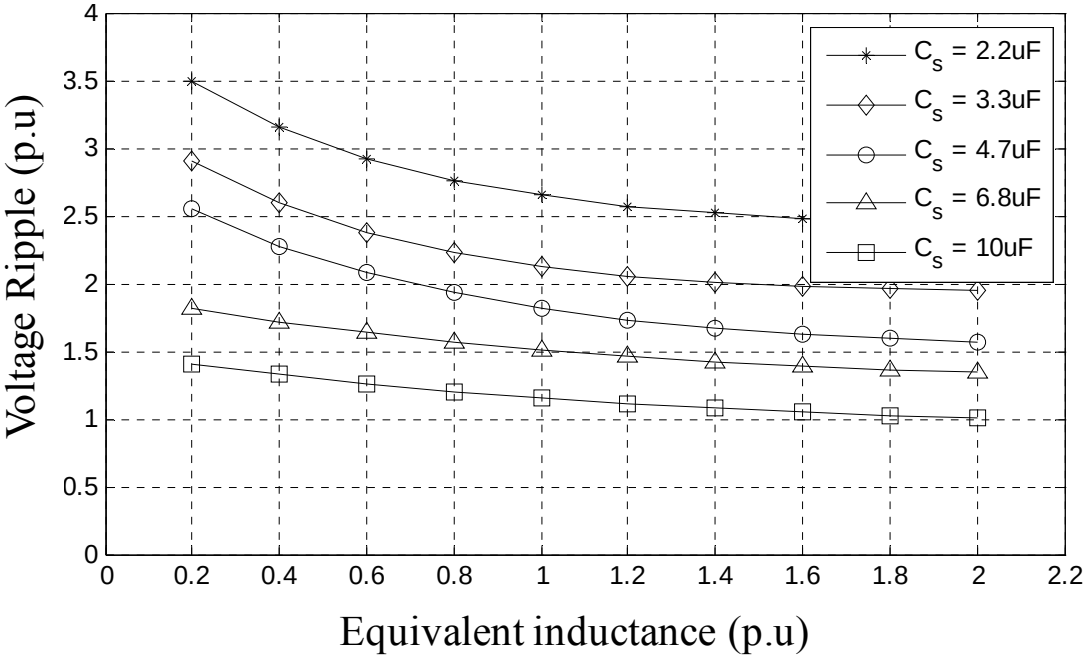

Fig. 3.12. Voltages ripple vs. capacitance vs. inductance.

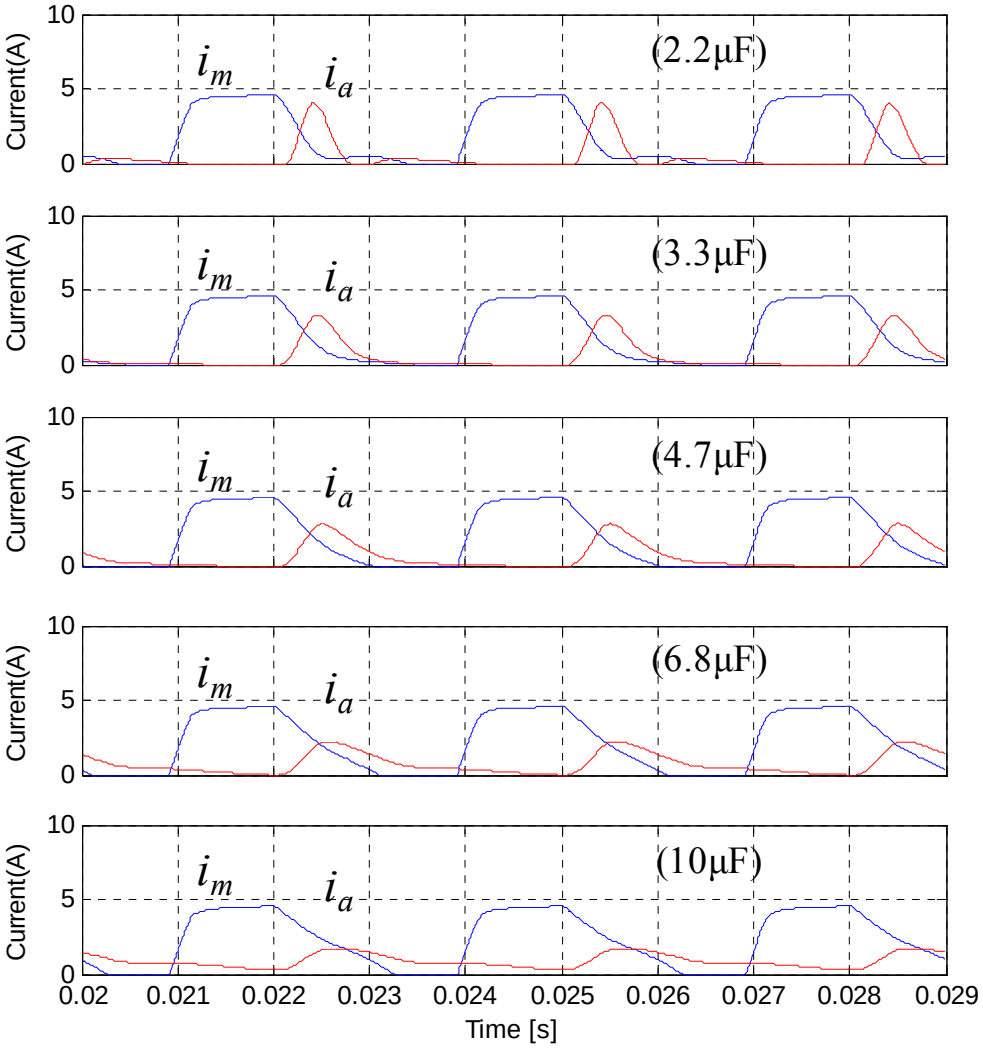

Fig. 3.13. Main and auxiliary winding currents for different sizes of capacitor C_r

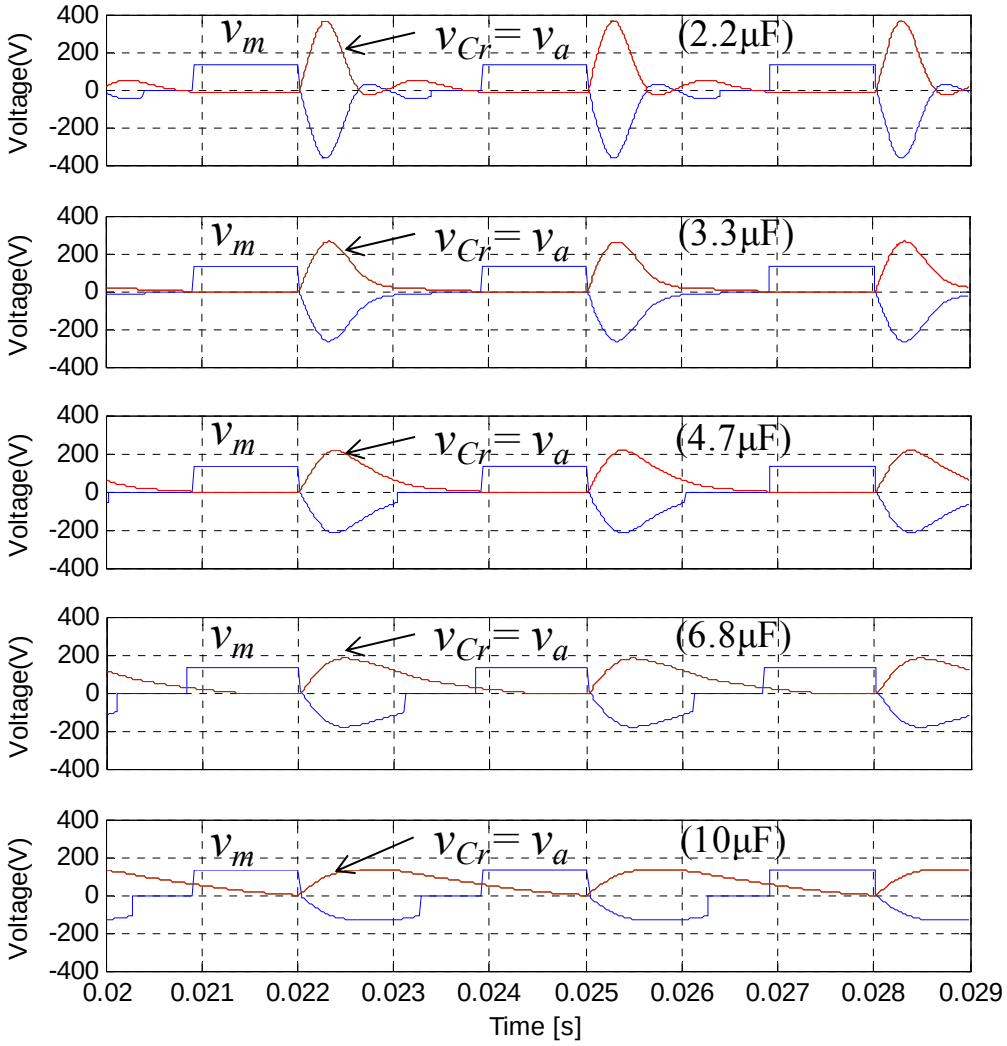

Fig. 3.14. Voltages across the main winding, auxiliary winding, and the capacitor C_r for different size of C_r.

3.6 Comparison of the Proposed Converter With Other Converters

The comparison of the new single-switch converter with the original single-switch converter, the conventional asymmetric bridge converter for driving a single-phase machine, and the full-wave bridge inverter for a three-phase ac machine is summarized in Table 3.2. The comparison is made in terms of the component count, device ratings, and losses to provide a clear demarcation from the original single-switch drive system and the prevalent three-phase inverter-based ac system to assess the merits and demerits of the new drive system. For safety operation, the power switches and diodes are chosen based on their peak and rms current and voltage ratings. Although the considered motor has two phases, it functions as a single-phase motor, as most of the torque is produced from the main phase. Hence, the current ratings are the same as the single-phase motor with the asymmetric converter. However, the switch voltage rating of the proposed converter is larger than that of the asymmetric converter.

Table 3.2 Comparison of the new converter with other converters

Criteria	Full-wave Inverter	Asymmetric Bridge	Original Converter	New Converter
No. of power switches	6	2	1	1
No. of diodes	6	2	1	1
No. of gate drives	6	2	1	1
No. of power supplies for isolated gate drivers (min)	4	2	1	1
Switch voltage rating (min)	V_{dc}	V_{dc}	$2V_{dc}$	$2V_{dc}$
Switch current rating (peak)	I_p	I_p	I_p	I_p
Switch current rating (rms)	$I_p/\sqrt{3}$	$I_p/\sqrt{2}$	$I_p/\sqrt{2}$	$I_p/\sqrt{2}$
Converter VA rating (peak)	$6V_{dc}I_p$	$2V_{dc}I_p$	$2V_{dc}I_p$	$2V_{dc}I_p$
Switch conduction losses	$2d_sI_p$	$2d_sI_p$	d_sI_p	d_sI_p
Diode conduction losses	$2(1-d_s)I_p$	$2(1-d_s)I_p$	$(1-d_s)I_p$	$(1-d_s)I_p$
Recovery capacitor rating	N/A	N/A	$2.5V_{dc}$	$1.5V_{dc}$
Heat sink size (p.u)	2	1	0.5	0.5

Note: I_p is the peak rated motor phase current and d_s is the switch duty ratio.

Although the asymmetric converter is known for its high performance, high cost is its major disadvantage. Among the advantages of the proposed converter compared to asymmetric bridge converters are less switching devices hence less driving circuits and less conduction losses. When compared to the original single-switch converter, the new converter has less voltage rating for the recovery capacitor. Regardless of their superior performance, the highest parts count and cost are the major deterrent for the widely-used standard inverter-fed ac drives to be embraced into the target low cost applications. The selection of power semiconductor devices including controllable switches and freewheeling diodes takes an important place in designing a converter. The devices are carefully selected based on several factors but mainly considering a trade-off among their power handling capability, transient characteristics, and cost.

3.7 Drive System Control

3.7.1 Self-starting

At standstill, when S1 is turned on for a preset period of time to induce a large current pulse in the main phase winding. This current, along with the current through the auxiliary phase winding when S1 is turned off, results in torque production and causes the rotor to move. Note that the number and period of the applied starting pulses are predetermined based on required starting torque.

3.7.2 Four-quadrant Operation

Significant features peculiar to this converter are limited direct current control of the main phase and its heavy dependence on the auxiliary phase winding and auxiliary capacitor state. Likewise, the auxiliary winding current control is dependent on the duty cycle of the controllable switch, motor speed and load, and state of the auxiliary capacitor. These constraints have to be managed very tightly in order to implement a four-quadrant variable-speed operation in this motor drive.

The disadvantages of this drive are: (i) At the time of starting, there is no directional control but once it is started, the directional and speed control are achieved which is not very different from many microwave oven drive systems. (ii) Torque ripple free operation is not feasible with this drive as it functions mostly as a single phase SRM drive system. But this drive

has many suitable applications in blenders, hair dryers, vacuum cleaners and other high volume products that are immensely cost sensitive.

3.7.3 Position Sensorless Operation

Further cost saving of the drive system can be achieved by employing the operation without a position sensor, hence making the proposed drive system even more attractive to highly cost-sensitive applications. A large variety of control algorithms for rotor position sensorless operation have been published so far and selection of a proper scheme is primarily dependent on the applications and the drive cost. A novel simple position sensorless control scheme is proposed and implemented on the single-switch converter. This will be discussed in detail in Chapter 6.

3.8 Dynamic Simulation

To validate the operation principle and analysis of the proposed drive system discussed in the previous sections, dynamic simulation was performed based on the analytic model derived in Section II. The nonlinear magnetic and torque characteristics of the machine were obtained from finite element analysis. The simulation results are given in Fig. 3.15. The waveforms depicted in Fig.3.15 include the currents of the main and auxiliary windings, voltages across the main and auxiliary windings, voltage across the capacitor Cr, and the electromagnetic torque. The motor is running at its rated speed of 5000 r/min supplied from the rectified single-phase ac main (120Vrms). As shown in Fig.3.15, the commutation of both main and auxiliary winding currents is achieved effectively without generating a negative torque for a positive load torque.

The proposed drive system shows good commutation of main and auxiliary currents unlike the previous system where both main and auxiliary currents are continuous as the current command increases. In single-pulse operation, it is seen that no significant negative torque by the auxiliary current maximizing the system efficiency.

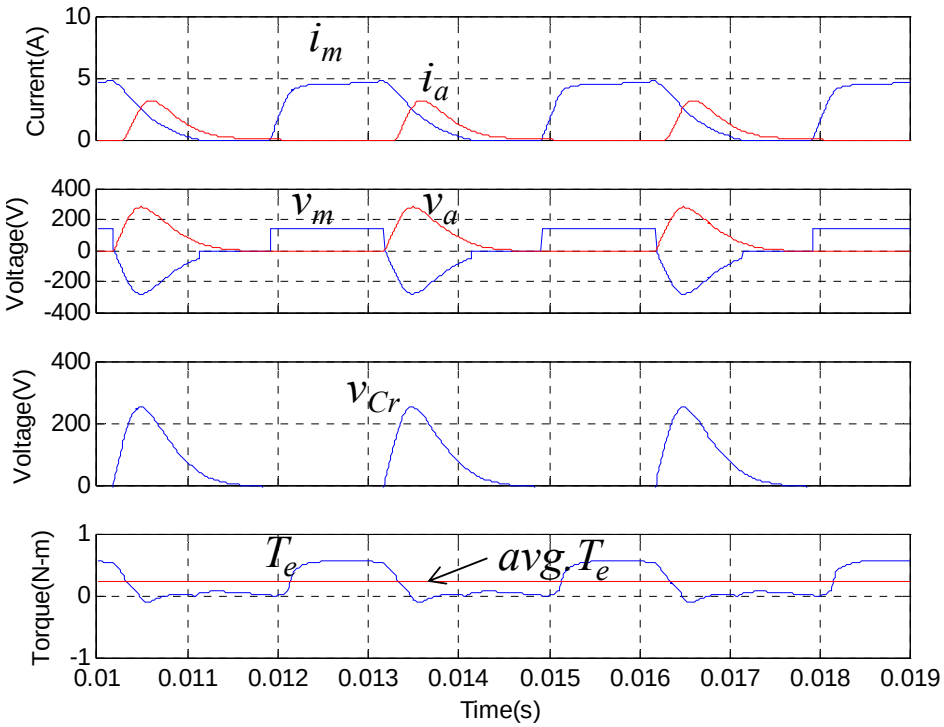

Fig. 3.15. Simulated waveforms for the drive system running at 5000r/min with the 3.3μF recovery capacitor

3.9 Experimental Verification

The prototype single-controllable converter for experiments is shown in Fig. 3.16. The main converter board has a compact 5"x3" footprint that includes the power stage, gate drive, analog signal interface, and logic power supply. A DSP controller, TMS320F2808 has been employed to implement the drive control algorithm. The speed and position are estimated using two hall-effect sensors mounted on the each of two adjacent stator poles. Device control is accomplished with an ezDSP evaluation board with a TI C2000F2808 microcontroller. The MCU is a 32-bit fixed point controller with 100MHz clock and dsp type MAC operations. Although the F28x series are general purpose chips, they are especially designed for use in high performance motor controllers. Built-in peripherals include a highly configurable set of 16 PWMs and 6 high resolution PWMS, 16 12-bit ADCs, 3 32-bit CPU timers, 6 32-bit timers and 2 quadrature encoder interfaces. Code development was composed in C++ with the Code Composer StudioTM IDE and processor programming was enabled by the JTAG-Jet Tms

emulator. Precompiled header files and libraries from the TI site were used to configure and interface with peripherals, particularly the ADC, PWM and quadrature encoder. Fig. 3.17 shows the prototype machine utilized for experiments. The minimization of component parts is obvious for this machine construction and that is an asset in applications.

Experimental testing conducted to validate the performance of the proposed drive system are described as follows. The execution of the self-starting algorithm is shown in Fig. 3.18. At standstill, S_1 is turned on for a preset period of time to induce a large current pulse in the main phase winding. This current, along with the current through the auxiliary phase winding when S_1 is turned off, results in torque production causing the rotor to move. Note that the number and period of the applied starting pulses are predetermined based on required starting torque to achieve reliable starting at any rotor position. Once the motor starts, the controller executes the normal commutation algorithm for the main phase and the motor is driven to the desired speed. Only during the short period of initial acceleration, the PWM chopping mode is employed and then the control transitions to the single-pulse mode, reaching its rated speed quickly. The commutation angle control for the main phase is based on the optimized turn-on and turn-off angles for different speed ranges, estimated from dynamic simulations. Fig. 3.19 shows the measured waveforms of the main and auxiliary winding currents as well as the recovery capacitor voltage for the drive system operating at its base speed of 5000 r/min. The optimal size of the recovery capacitor for the prototype drive was selected based on the analytic estimation and the simulation results discussed in Section 3.5. It can be seen that the measured waveforms in Fig. 319 are very similar to those from the simulation in Fig. 3.15, i.e., the commutation of the main phase is achieved successfully through the auxiliary winding and recovery capacitor, which correlates well with the simulation results. Unlike the continuous conduction in PWM operation shown in Fig.3.9, the desirable commutation of the auxiliary winding in single-pulse mode is also achieved.

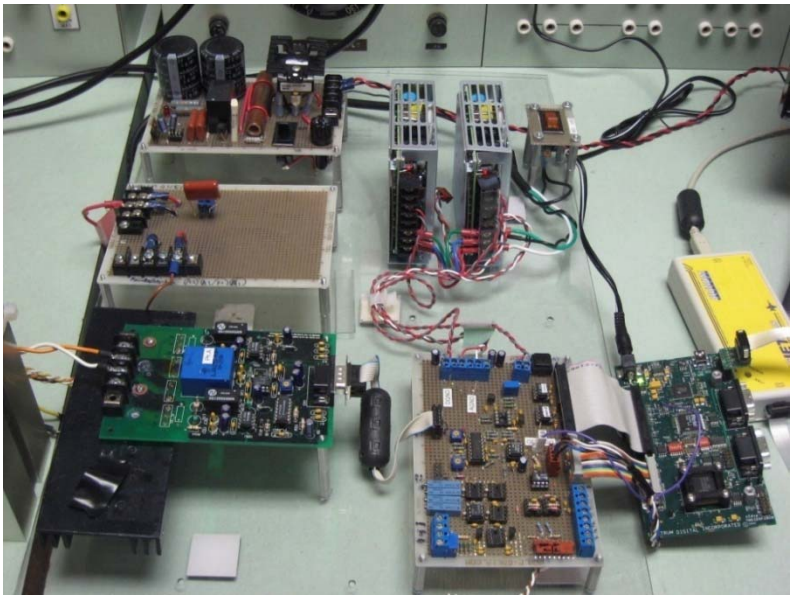

Fig. 3.16. Prototype single-controllable switch converter and control interface electronics.

(a) Front view

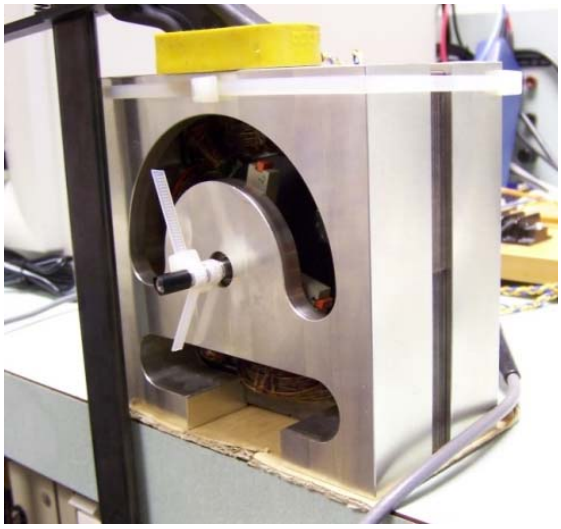

(b) angled view

Fig. 3.17. Prototype asymmetric 8/4 SRM

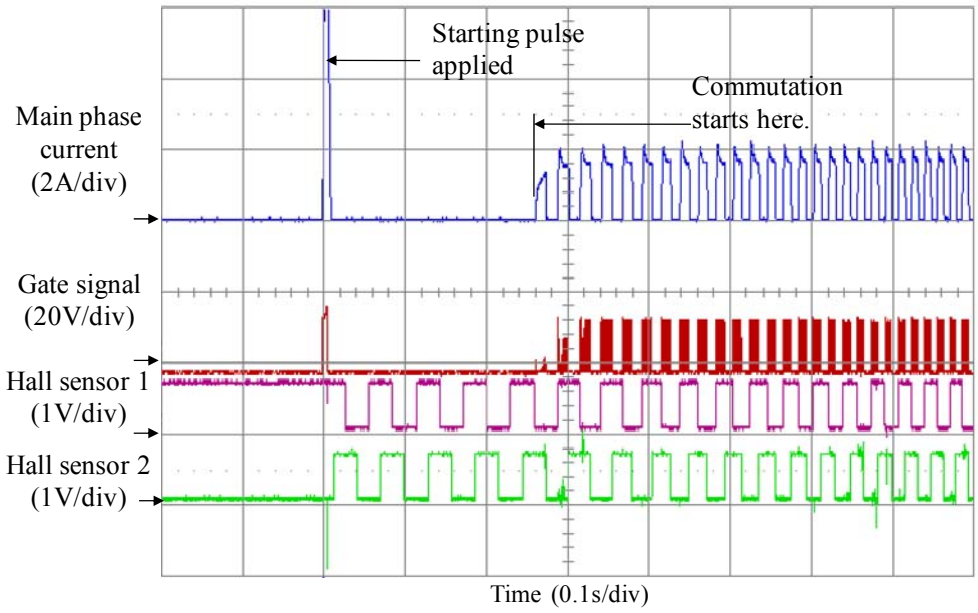

Fig. 3.18. Execution of self-starting of the motor from standstill

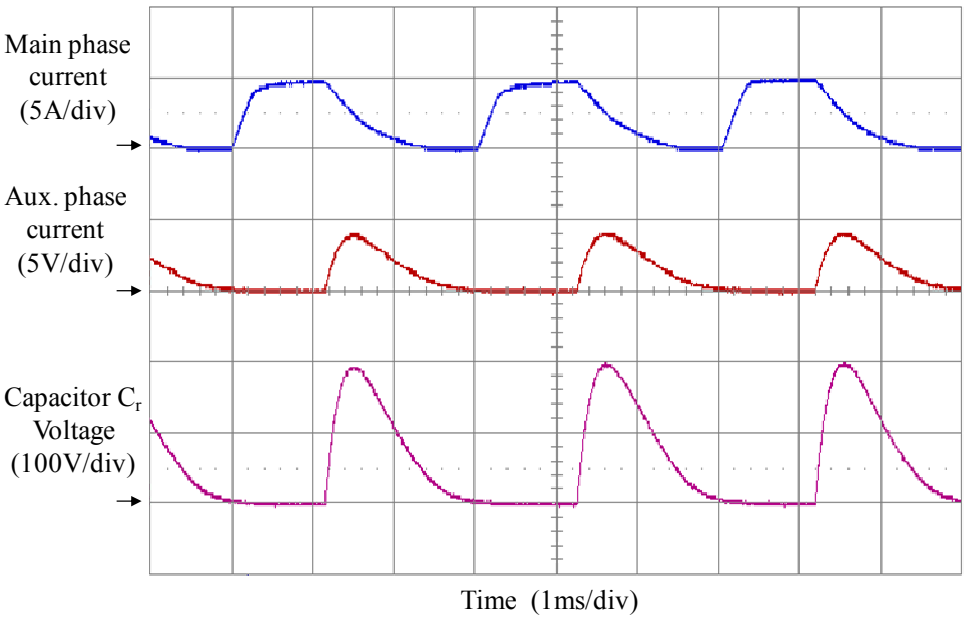

Fig. 3.19. Measured waveforms: main and auxiliary winding currents, recovery capacitor voltage (C_r =3.3μF) when the motor is running at 5000r/min

Acoustic noise is a serious concern in SRM drives and particularly so in the single phase category because of the inherent discontinuous torque generation. The least noise is produced by the SRM driven with asymmetric converter as it has tremendous control latitude. In order to ascertain the control quality offered by the new converter, it is important to compare the noise performance with that of the asymmetric converter based single phase SRM drive. The acoustic noise measurement results on the laboratory prototype are given in Table 3.3. In order to accurately measure the audible noise caused by vibrations in electrical machines, it usually is made in an anechoic chamber after calibrating the measuring equipments and measuring sound pressure at several points. However, an anechoic chamber is not available in the normal laboratory environment and, therefore, measurements can be made in an ordinary large room after measuring the ambient noise. The measurement was conducted in a laboratory with 49.5dBA ambient noise. The new converter produces slightly less noise level than the original converter. At 2000r/min with PWM control, the both single-switch converters generate more noise than the asymmetric converter due to the continuous conduction in auxiliary winding causing negative torque. In the single-pulse mode (5000r/min), however, the single-switch converters generate the noise level comparable to that of the asymmetric converter-based drive and note that this is the intended control strategy for targeted applications.

Table 3.3. Measured acoustic noise

	Asymmetric converter	Original converter	New converter
PWM mode	56.5	60.7	60.2
Single-pulse mode	65.4	66.1	65.8

Note: The unit is dB and the ambient noise is 49.2dBA.

3.10 Summary

The converter coupled with the two-phase SRM has bidirectional starting and four-quadrant capability. Due to the low cost compact design and high-speed operation, the proposed drive system can be a viable solution for industrial and domestic applications such as fans, pumps, and home appliances.

A new low-cost, brushless variable-speed drive requiring only a single controllable switch and a diode that overcomes the drawbacks of the original single-switch converter is presented. The key results of the study are:

- The most minimum number of passive and active devices of the original single switch drive is retained in the present invention but their ratings are sized down to achieve the most compact and low cost drive system. It is believed, as of date, that this is the most viable low cost brushless variable speed drive system for high volume applications.
- The operation, modeling, simulation, analysis, design and prototype testing of the new drive system are presented.
- Design consideration for optimal commutation of the phase currents is studied based on the analytic estimation. This is justified by both dynamic simulation and experimental results
- Experimental work correlates the simulation counterpart well and the drive system's working over its full speed range demonstrates the suitability of the new drive system for targeted applications.
- The drive is contrasted with the asymmetric bridge based single phase SRM drive, the original single controllable switch drive and also a brushless motor drive with a six-controllable switch based inverter. The proposed drive is superior to all others both in number of active devices used, their ratings, packaging size and inferred cost.
- Acoustic noise measurements on the new converter based laboratory prototype demonstrate the parity in performance of the asymmetric based SRM drive thereby proving that the control latitude of the new converter is on par with the best converter available for SRM drive systems. Also the noise is within the bounds of acceptable levels in the targeted applications.

Chapter 4

Proposed Drive System 2: Two-Controllable-Switch-Based SRM Drive

4.1 Introduction

Although the single-controllable-switch-based SRM drive presented in the previous chapter can be a strong candidate for low cost high volume applications, precise control of the main phase winding current is not possible at all levels of current and lack of control of the auxiliary phase winding current results in increased torque ripple and reduced system efficiency. Therefore, a new two-switch converter [33] that improves performance while still preserving the advantages of the single-switch drive is presented and studied in detail in this chapter.

The proposed power converter employs a single-switch-per-phase configuration, hence requiring only two controllable switches in total to drive a two-phase SRM. Therefore, the converter is still cost-effective compared to the conventional asymmetric converter which requires a total of four controllable switches to drive a two-phase SRM.

The converter is unique in that it has two capacitors for energization of each phase. The primary capacitor, C1 functions mainly as a stiff voltage source to energize phase A (main winding), and the main phase winding is used as an energy storage for the secondary capacitor, C2 which, in turn, is used for phase B (auxiliary winding) energization as well as energy

recovery of phase A winding. The converter is inherently suited for a two-phase motor having asymmetry in its stator to realize self-starting and speed reversal.

The drive system presented in this chapter is realized using the proposed converter and the two-phase SRM presented in chapter 3. The motor is capable of self-starting at any rotor position and four-quadrant operation. The proposed two-controllable-switch-based SRM drive can provide reliable starting, better utilization of machine capability, and better control of the winding currents compared to the single-controllable-switch-based SRM drive presented in the previous chapter.

This chapter first describes the basic analysis of the converter including topology, derivation of system equations, as well as principle of operations. Then, steady-state analysis in terms of voltage balance and energy transfer between the primary and secondary capacitors is described. Then, drive control algorithm including simple starting and capacitor C2 voltage control schemes are presented. Design consideration for a prototype drive system is also presented. Dynamic simulation for overall drive system is performed to predict the drive performance, followed by experimental tests in correlation with the simulation results. The proposed drive system offers a low-cost brushless variable speed drive that is a potential alternative for conventional brush-commutator motors in high volume applications such as home appliances, fans, hand tools, etc.

4.2 Proposed Drive System

4.2.1 Machine

The motor employed in the proposed drive system is the same as the one employed in the drive system in chapter 3. With the single-controllable-switch converter in chapter 3, the active control of the auxiliary phase is not possible and thus negative torque production of auxiliary phase is unavoidable. With the two-controllable-switch converter, however, active control of the auxiliary phase is feasible with an additional controllable switch. Therefore, the auxiliary phase can be controlled so that it can contribute not only the starting but also torque production during the normal operation both in PWM chopping and single-pulse controlled operation. In the current

experimental system, only one set of diametrically opposite auxiliary windings are utilized. This reduces the machine into an equivalent of a two phase motor. Additional information on magnetization characteristics and performance is presented in chapter 2.

4.2.2 Power Converter

The topology of the novel power converter is shown in Fig. 4.1. The converter has two capacitors contributing to each phase's magnetization, i.e. the primary capacitor, C1 for phase A (main winding) and the secondary capacitor, C2 for phase B (auxiliary winding). During demagnetization of the phase windings, capacitors C1 and C2 are charged by energy from the complementary phase. In this regard, the converter has a similarity with the split dc source converter for a two-phase SRM. The key features of the proposed converter can be deduced by observations and they are:

1) The converter has a low cost single-switch-per-phase (SSPP) configuration. Therefore, packaging of drive electronics can be compact resulting in smaller heat sink, lower number of gate drives, and lower number of isolated power supplies for gate drives.
2) Having only one switch per phase yields only one switch voltage drop per phase. This makes the converter suitable for low supply voltage applications.
3) There is no freewheeling mode available in this converter. Only two modes, magnetization and demagnetization of the machine phase windings are available and they are realized by switching the transistors T1 and T2.
4) Due to the absence of the freewheeling mode, soft chopping scheme cannot be employed. Thus, finer control of the current in terms of its ripple may not be feasible.
5) While C1 is a stiff voltage source fed by the rectified AC main, C2 is a dependent voltage source fed only by demagnetization energy from phase A.
6) Although C2 is dependent on phase A excitation, with careful selection of this capacitor, the average voltage and ripple of C2 can be maintained within an acceptable range over the entire speed range. The unequal voltages of C1 and C2 do not affect significantly the operation of the drive system.
7) The converter is inherently suited for two-phase SRMs having asymmetric stator phases to realize self-starting as well as speed reversal.

8) By directly controlling the auxiliary phase winding (phase B) current, the negative torque affecting efficiency and noise when the drive system is realized with the single-switch converter can be improved. Hence, the drive can achieve better utilization of the electromagnetic capability of the motor.

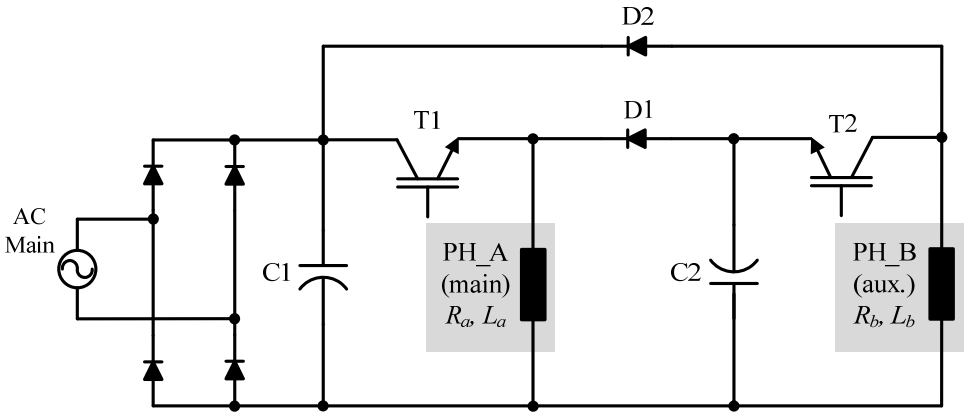

Fig. 4.1. Proposed two-controllable-switch converter

4.3 Derivation of System Equations and Principle of Operation

In every switching period, each phase encounters two main modes: magnetization and demagnetization. Hence, four main modes in addition to two auxiliary modes are available as illustrated from Figs. 4.2 through 4.7. Each mode of operation is described with corresponding voltage and current equations, respectively. Note that each phase winding has different number of turns and thus different resistance and inductance.

Mode A-1 : Phase A Magnetization

When T1 is turned on, the dc link voltage, V_{C1} is applied to phase A winding. Current flows through C1 and T1 thus magnetizing the phase A winding. The voltage and current equation equations for this mode are given by

$$v_a = V_{C1} = R_a i_a + L_a \frac{di_a}{dt} + i_a \frac{dL_a}{d\theta}\omega_r = \left(R_a + \frac{dL_a}{d\theta}\omega_r \right) i_a + L_a \frac{di_a}{dt} \tag{4.1}$$

$$i_a(t) = I_{a1} e^{-t/\tau_a} + \frac{V_{C1}}{R_{eq\_a}}\left(1 - e^{-t/\tau_a}\right) \tag{4.2}$$

where

$$R_{eq\_a} = R_a + (dL_a/d\theta)\omega_r \tag{4.3}$$

$$\tau_a = L_a / R_{eq\_a} \tag{4.4}$$

R_a is phase A winding resistance, L_a is phase A's self-inductance, ω_r is the rotor speed, and I_{a1} is the initial current in phase A for this mode.

Mode A-2 : Phase A Demagnetization

When T1 is turned off, negative voltage, $-V_{C2}$ is applied to phase A winding. The current continues to flow but through a different path, phase A, C2, and D1 resulting in demagnetization of phase A, hence charging C2. The voltage and current equations for this mode are given by

$$v_a = -V_{C2} = R_a i_a + L_a \frac{di_a}{dt} + i_a \frac{dL_a}{d\theta}\omega_r = \left(R_a + \frac{dL_a}{d\theta}\omega_r \right) i_a + L_a \frac{di_a}{dt} \tag{4.5}$$

$$i_a(t) = I_{a2} e^{-t/\tau_a} - \frac{V_{C1}}{R_{eq\_a}}\left(1 - e^{-t/\tau_a}\right) \tag{4.6}$$

where I_{a2} is the initial current in phase A current for this mode.

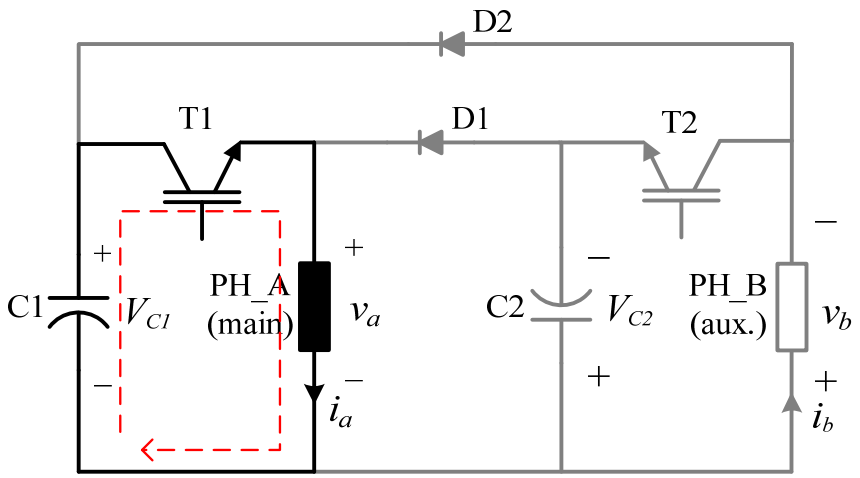

Fig. 4.2 Mode A-1 (T1: on, T2: off, D1: off, D2: off)

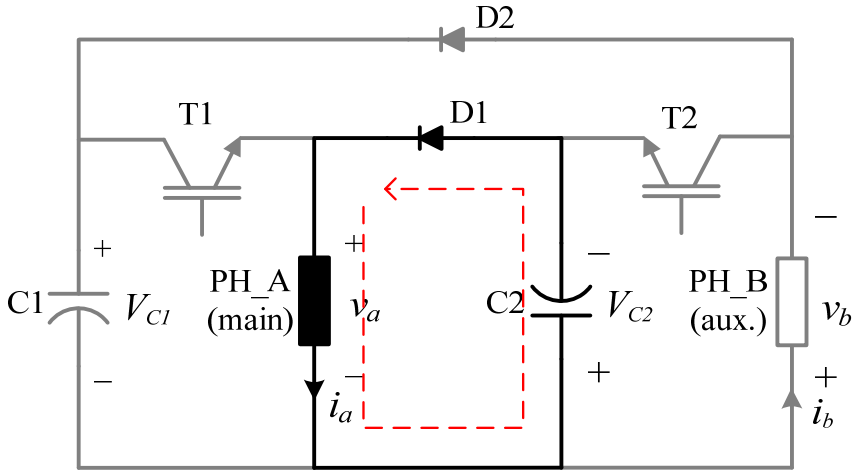

Fig. 4.3 Mode A-2 (T1: off, T2: off, D1: on, D2: off)

Mode B-1: Phase B Magnetization

When T2 is turned on, the capacitor C2 voltage V_{C2} is applied across phase B. Current circulates through C2, phase B, and T2 thereby supplying energy to magnetize the phase B winding. The voltage and current equations for this mode can be derived similarly to those of phase A and they are

$$v_b = V_{C2} = R_b i_b + L_b \frac{di_b}{dt} + i_b \frac{dL_b}{d\theta}\omega_r$$
$$= \left(R_b + \frac{dL_b}{d\theta}\omega_r \right) i_b + L_b \frac{di_b}{dt} \tag{4.7}$$

$$i_b(t) = I_{b1} e^{-t/\tau_b} + \frac{V_{C2}}{R_{eq\_b}} \left(1 - e^{-t/\tau_b}\right) \tag{4.8}$$

where

$$R_{eq\_b} = R_b + (dL_b/d\theta)\omega_r \tag{4.9}$$

$$\tau_b = L_b / R_{eq\_b} \tag{4.10}$$

where R_b is phase B winding resistance, L_b is the phase B self-inductance, and I_{b1} is the initial current of phase B winding, respectively.

Mode B-2 : Phase B Demagnetization

When T2 is turned off, the current continues to flow but through phase B, D2, and C1. The voltage applied to phase B winding is -V_{C2}, and phase B begins to demagnetize. The voltage and current equations for this mode are given by

$$v_b = -V_{C1} = R_b i_b + L_b \frac{di_b}{dt} + i_b \frac{dL_b}{d\theta}\omega_r$$
$$= \left(R_b + \frac{dL_b}{d\theta}\omega_r \right) i_b + L_b \frac{di_b}{dt} \tag{4.11}$$

$$i_b(t) = I_{b2} e^{-t/\tau_a} - \frac{V_{C1}}{R_{eq\_b}} \left(1 - e^{-t/\tau_b}\right) \tag{4.12}$$

where I_{b2} is the initial condition on phase B current for this mode. During the commutation of each phase current there is a phase current overlaps, i.e. the both phase in Figs.4.6 and 4.7 Although it might be negligible the mutual coupling

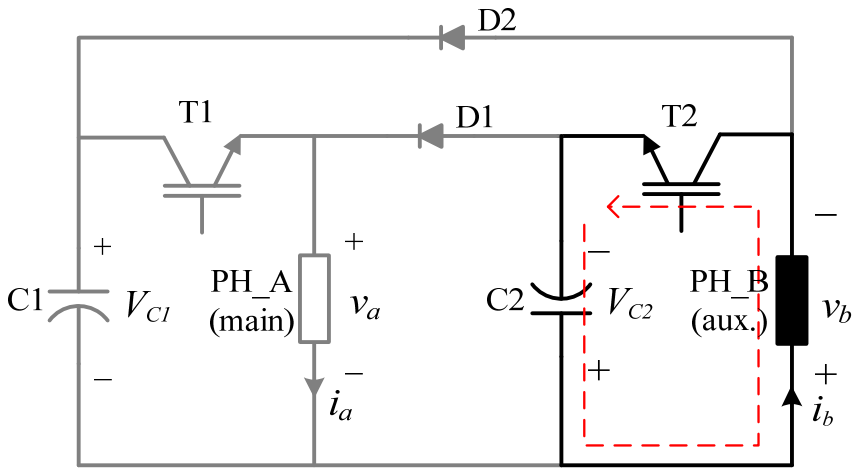

Fig. 4.4 Mode B-1 (T1: off, T2: on, D1: off, D2: off)

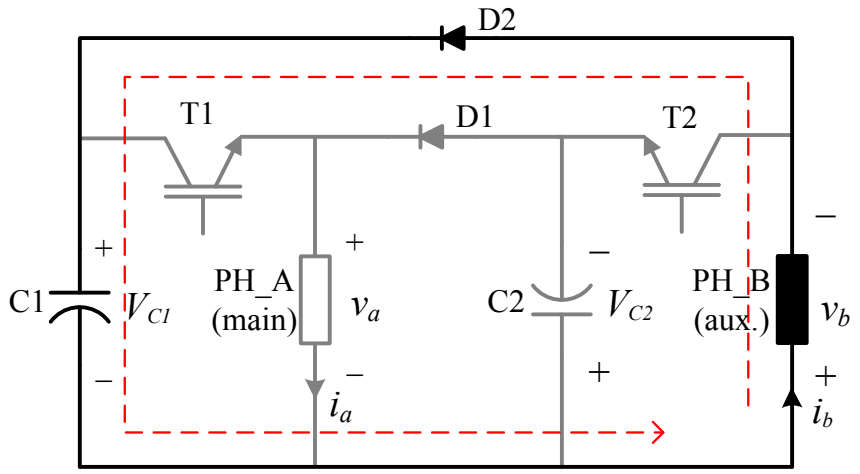

Fig. 4.5 Mode B-2 (T1: off, T2: off, D1: off, D2: on)

Mode C-1 and C-2 : Phase current overlap during commutation

These modes of operation occur when excitation of one phase is established during the other phase's commutation. Thus, the currents of both phases overlap each other. Figs. 4.6 and 4.7 depict phase current overlap during phase A commutation and phase B commutation respectively.

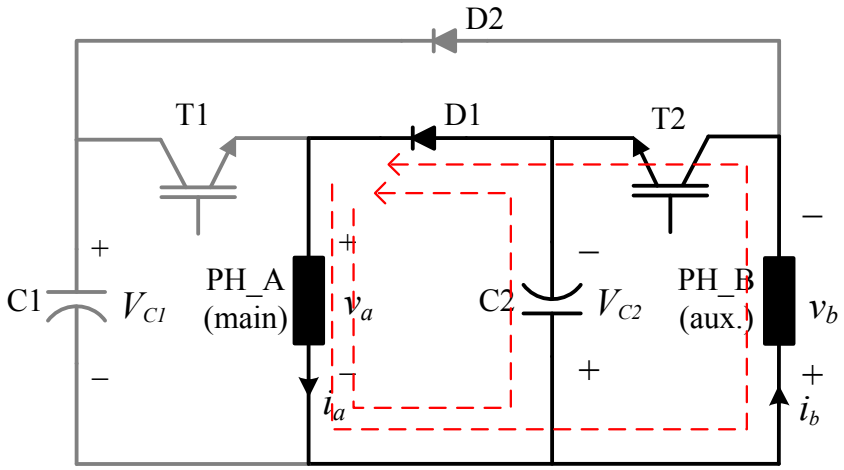

Fig. 4.6. Mode C-1: Current overlap during the phase A commutation

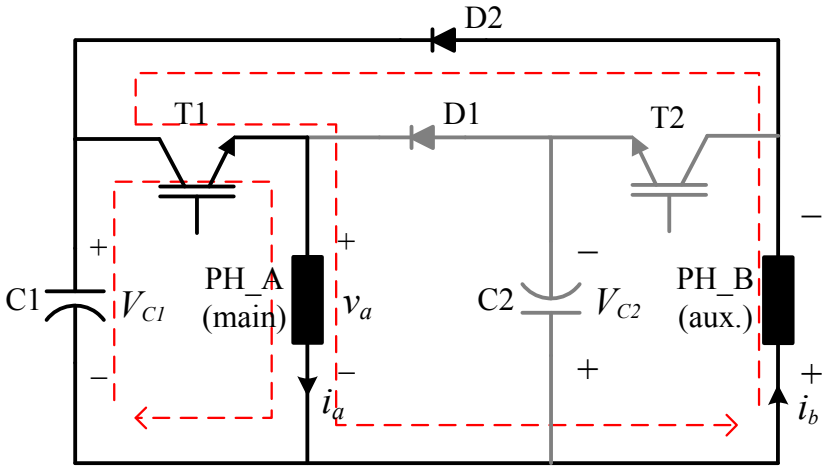

Fig. 4.7. Mode C-2: Current overlap during the phase B commutation

4.4 Steady State Analysis

4.4.1 Estimation of Capacitor C2 Voltage

The charging of C2 is dependent on the amount of energy recovered from phase A, and the discharging of C2 is determined by the amount of energy required for phase B excitation.

Therefore, C2 voltage, V_{C2} varies with operating conditions and it is difficult to estimate and control it at the same level as C1 voltage, V_{C1}.

The voltage imbalance between C1 and C2 results in unequal excitation and commutation for each phase. However, this imbalance does not affect the drive performance significantly due to the unique machine structure of which the stator phases are asymmetric. Phase B (auxiliary winding) is much smaller in stator pole size and in winding copper volume compared to the phase A (main winding), optimized for the cost of the drive system. Phase A contributes to most of the generated torque, while phase B aids in starting and speed reversal. Therefore, as long as V_{C2} can be maintained within a level sufficient to produce self-starting and contribute to motoring and speed reversal, the voltage imbalance cannot be a hindrance to operation of the drive since the target applications are not torque ripple sensitive. However, reasonable estimation of V_{C2} is important for the proper design and operation of the drive system and it can be estimated as follows.

The proposed converter can be considered as a buck-boost topology assuming phase A winding as an energy storage inductor and phase B winding with T2 and D2 as an equivalent load as shown in Fig. 4.8. However, unlike the conventional dc-dc converter, the machine phase should be modeled by winding resistance, self-inductance, and induced back-EMF in series in the motor winding. The equivalent load for phase B can be given by

$$Z_{eq} = \frac{R_b i_{eq,\max} + K_e \omega_r + v_{L_b}}{i_{eq,\max}} \tag{4.13}$$

where $i_{eq,max}$ is the maximum current required by phase B, $K_e = dL_b/d\theta$, is the back-EMF constant of phase B, and $v_{Lb} = L_b(di_b/dt)$ is the inductive voltage drop in phase B winding, respectively. It is assumed that during steady-state operation all voltages and currents are periodic, and the speed and back-EMF are constant.

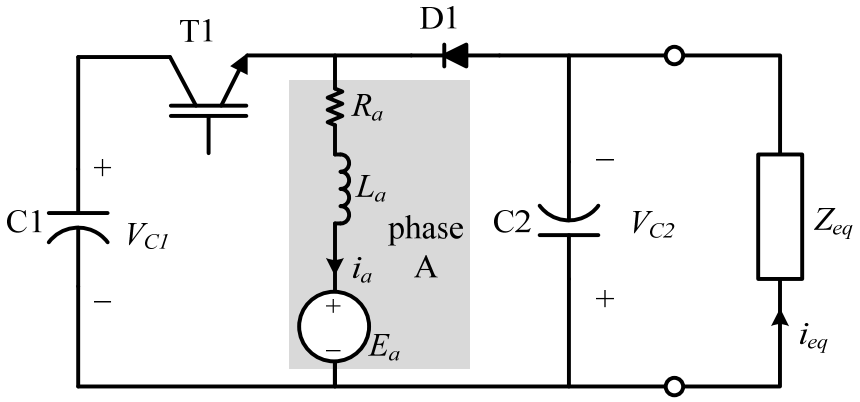

Fig. 4.8. Equivalent converter circuit for capacitor C2 voltage estimation

In the ideal case of a buck-boost converter, V_{C2} can simply be estimated as a function of switch T1 duty ratio, d_1:

$$V_{C2} = \frac{d_1}{1-d_1} V_{C1} \tag{4.14}$$

In the SRM converters, however, the effect of winding resistance, back-EMF, as well as loading should be considered. Note that the average voltage across the winding inductance over a switching period must be zero [35], i.e.

$$\begin{aligned} \frac{1}{T_s}\int_0^{T_s} v_L dt &= \frac{1}{T_s}\int_0^{t_{on}} v_L dt + \frac{1}{T_s}\int_{t_{on}}^{T_s} v_L dt \\ &= \underbrace{\left(V_{C1} - R_a I_a - e_a\right) d_1}_{T1\,on} + \underbrace{\left(-V_{C2} - R_a I_a - e_a\right)\left(1-d_1\right)}_{T1\,off} = 0 \end{aligned} \tag{4.15}$$

where T_s and t_{on} are switching period and on-time of T1 respectively. At constant speed, the back-EMF for phase A winding can be approximated as

$$e_a = \frac{dL_a}{d\theta}\omega_r I_a = \left(K_e \omega_r\right) I_a = K_e' I_a \tag{4.16}$$

and the average phase A current over the dwell time, I_a can be calculated using d_1 :

$$I_a = \frac{I_{eq}}{1-d_1} = \frac{V_{C2}}{Z_{eq}(1-d_1)} \tag{4.17}$$

Then, V_{C2} can be estimated by substituting (4.16) and (4.17) into (3.15):

$$V_{C2} \cong \frac{d_1 k_d}{1-d_1+\frac{(R_a+K'_e)}{Z_{eq}(1-d_1)}} V_{C1} \tag{4.18}$$

where k_d is the ratio of dwell-time to phase commutation cycle.

Using (4.18), Fig. 4.9 shows the plots of V_{C2} as a function of d_1 for different Z_{eq}, keeping V_{C1}, R_a, and K'_e constant. The dc link voltage, V_{C1}, is assumed to be 155V. As shown in Fig. 4.8, under given Z_{eq}, as d_1 increases, V_{C2} increases. However, the rate of increase of V_{C2} reduces as d_1 increases due to the effect of $(R_a+K'_e)/\{Z_{eq}(1-d_1)\}$ term in the denominator in (4.18), and when d_1 increases further, V_{C2} starts decreasing as $(R_a+K'_e)/\{Z_{eq}(1-d_1)\}$term becomes dominant. The effect of Z_{eq} can also be observed in Fig. 4.9. As Z_{eq} decreases, i.e. heavier load, the plot is shifted down. Therefore, it is found that V_{C2} varies with the operating condition and V_{C2} is likely to be less than V_{C1}.

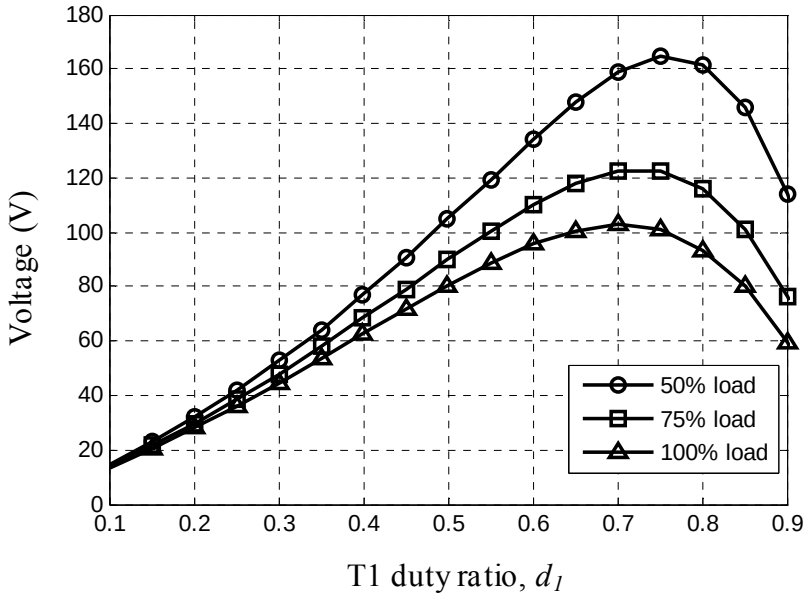

Fig. 4.9. Estimation of C2 voltage as a function of d1 for different Z_{eq}

4.4.2 Power Transfer Between C1 and C2

During the magnetization and demagnetization of the machine windings, power is transferred between the two capacitors via the phase windings as shown in Figs. 4.10 and 4.11 The converter can be seen as a conventional buck-boost converter in term of power transfer from C1 to C2 via phase A winding (Fig. 4.10) and from C2 to C1 via phase B winding (Fig. 4.11). The average power transfer between the capacitors can be calculated using averaging technique as illustrated in Fig. 4.12. This is important in that from this calculation, we can find the required power for phase B supplied by C2 and a critical C2 voltage for C2 selection.

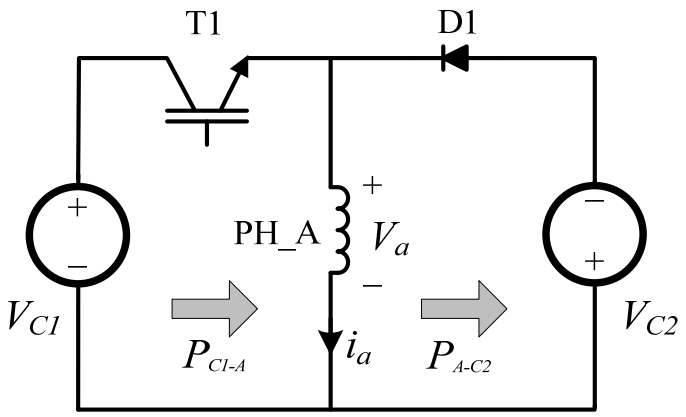

Fig. 4.10. Power transfer from capacitor C1 to C2 via phase A winding

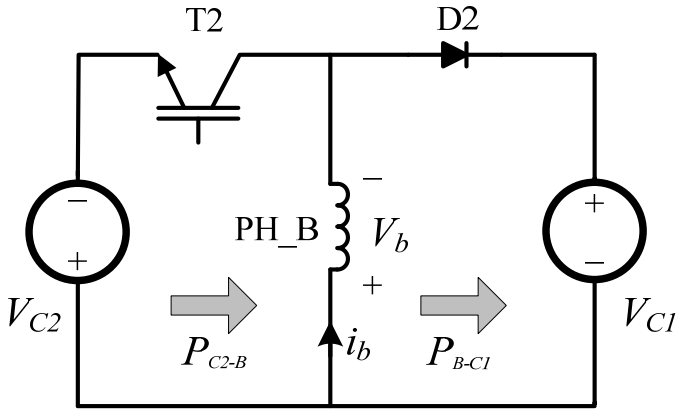

Fig. 4.11. Power transfer from capacitor C2 to C1 via phase B winding

When T1 is turned on during the motoring region, the phase A winding is magnetized. Part of the energy from C1 is stored magnetically in phase A winding and part is converted into mechanical output. The power transferred from capacitor C1 to phase A winding during T1 on-time interval is given by

$$\begin{aligned} p_{C1\_A}(t) &= \frac{d}{dt}\left(\frac{1}{2}C_1 v_{C1}^2\right) \\ &= \frac{d}{dt}\left(\frac{1}{2}L_a i_a^2\right) + \frac{i_a^2}{2}\frac{dL_a}{d\theta}\omega_r \end{aligned} \tag{4.19}$$

The first term in the right-hand side of (4.19) is the rate of energy stored in magnetic field and the second term is mechanical power. The average power delivered from C1 to phase A can be calculated by

$$P_{C1\_A} = V_{C1} I_{T1} = V_{C1}\left(d_1 I_a\right) = d_1 V_{C1} I_a \tag{4.20}$$

where I_{T1} is average switch T1 current, d_1 is switching duty ratio of T1, and I_a is average phase A current during excitation.

When T1is is turned off, stored magnetic energy is partly converted to mechanical output and partly supplied to capacitor C2. The power transferred from phase A to C2 is

$$\begin{aligned} p_{A\_C2}(t) &= \frac{d}{dt}\left(\frac{1}{2} L_a i_a^2\right) \\ &= \frac{i_a^2}{2}\frac{dL_a}{d\theta}\omega_r + \frac{d}{dt}\left(\frac{1}{2} C_2 v_{C2}^2\right) \end{aligned} \tag{4.21}$$

The average power delivered to C2 can be calculated by

$$P_{A\_C2} = V_{C2} I_{D1} = V_{C2}\left(1 - d_1\right) I_a = \left(1 - d_1\right) V_{C2} I_a \tag{4.22}$$

where I_{D1} is average diode D1 current. The power transferred from C2 to C1 via phase B winding can also be calculated similarly to above calculations. From (4.20), minimum power required by phase B for critical C2 voltage can be calculated.

Likewise, the average power transferred from C2 to phase B can be calculated by

$$P_{C2\_B} = V_{C2} I_{T2} = V_{C2}\left(d_2 I_b\right) = d_2 V_{C2} I_b \tag{4.23}$$

where I_{T2} is average switch T2 current, d_2 is switching duty ratio of T2, and I_b is the average phase B current during excitation. The power transferred from phase B to C1 can also be calculated by

$$P_{B\_C1} = V_{C1} I_{D2} = V_{C1}(1-d_2) I_b = (1-d_2) V_{C1} I_b \tag{4.24}$$

where I_{D2} is the average D2 current.

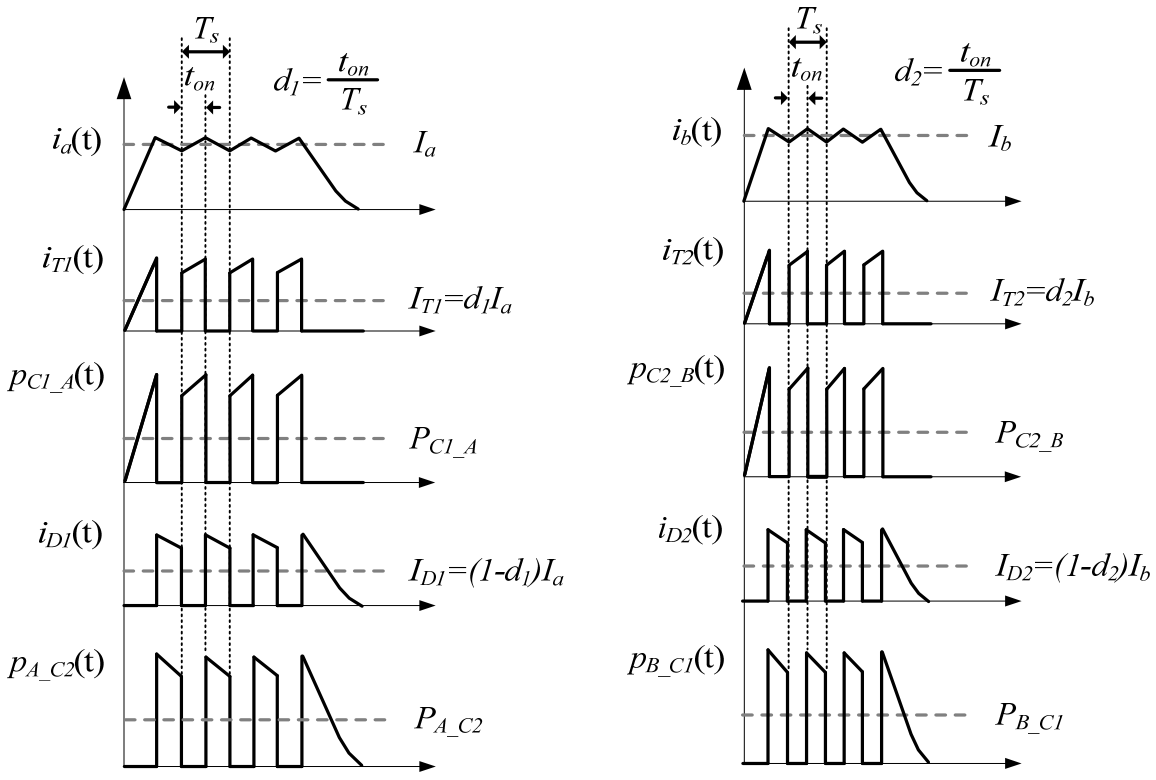

Fig. 4.12. Operational waveforms for power calculation

4.5 Design Consideration

There are several factors to be considered when choosing power switching devices for the SRM converter such as drive power level, supply voltage, current rating, cost, etc. The minimum voltage rating of the power devices is determined by the peak voltage stress applied to the devices. Assuming capacitor C2 is charged up to dc link voltage level, V_{dc}, the peak voltage stress on each switch T1 and T2 at turn-off instant is $2V_{dc}$. Therefore, the minimum voltage

rating for the switches is $2V_{dc}$. The peak voltage stress of the diodes, D1 and D2 is the same as that of T1 and T2.

For the device current rating, two types of current ratings should be considered, namely, peak and continuous current ratings. The current waveforms can be approximated by a periodic pulsed current neglecting the PWM chopping ripple [24]. The peak current rating should be at least equal to the peak reference current corresponding to maximum torque in the current-regulated constant-torque operating region, and it can be calculated as

$$I_p = \frac{P_{in}}{m\eta k_d V_{dc}} \tag{4.25}$$

where P_{in} is the machine input power, m is the number of machine phases, η is the predicted machine efficiency, k_d is the ratio of dwell-time to phase commutation period, and V_{dc} is the nominal dc supply voltage, respectively. The continuous current rating should be equal to or higher than the rms current per phase at maximum torque and is given by

$$I_{rms} = \sqrt{\frac{1}{T_{ph}}\int_0^{t_d} \left(i_{ph}\right)^2 dt} \tag{4.26}$$

where T_{ph}, are t_d are the phase commutation period and dwell time respectively.

The size of C2 has to be determined such that it should be capable of supplying sufficient energy to phase B while meeting the specified voltage ripple and cost constraint. The worst-case voltage ripple appears when C2 is discharged during phase B excitation. Hence, the minimum value of C2 can be calculated using the energy absorbed by phase B winding during phase B conduction:

$$W_c = \frac{1}{2}C\left(V_{C\max}^2 - V_{C\min}^2\right) \tag{4.27}$$

$$C = \frac{2P_c \Delta t}{\left(V_{C\max}^2 - V_{C\min}^2\right)} \tag{4.28}$$

where V_{max} and V_{mim} are the maximum and minimum value of the capacitor C2 voltage considering less than 20% ripple, P_b is power required by phase B, Δt is the maximum phase B conduction time.

4.6 Drive Control and Operation

4.6.1 Starting

The voltage of capacitor C2 is zero at standstill. Therefore, first, C2 has to be charged up to a level that is sufficient for torque production through phase B to facilitate starting. This can be achieved using a starting scheme similar to the scheme proposed in [31]. Applying a single- or multiple pulses to phase A winding for a finite time by switching T1 results in torque production to align the rotor pole with the phase A stator pole. When T1 is turned off, the current decays through C2 and thus charges it. Note that the duration and number of pulses are predetermined based on the required starting torque and required value of C2 voltage. Fig. 4.13 shows the initial charging of C2. The dc link voltage, V_{C1} is 155V. Applying a pulse for a short period of time impresses current in phase A and charges C2 up to 120V.

After rotor alignment and C2 charging, the controller executes an algorithm for commutation of each phase in synchronism with rotor position. It is critical to ensure that the desired direction of rotation is enforced quickly when the self-starting pulse is applied, so that the rotor does not traverse noticeably over a significant angular distance in the unintended direction. If the motor starts in the opposite direction to the desired direction, then the controller quickly reverses the direction to meet the direction requirement. That will involve motion in an undesirable direction for a short rotor movement and it usually is tolerated in low cost applications that this power converter is aimed at.

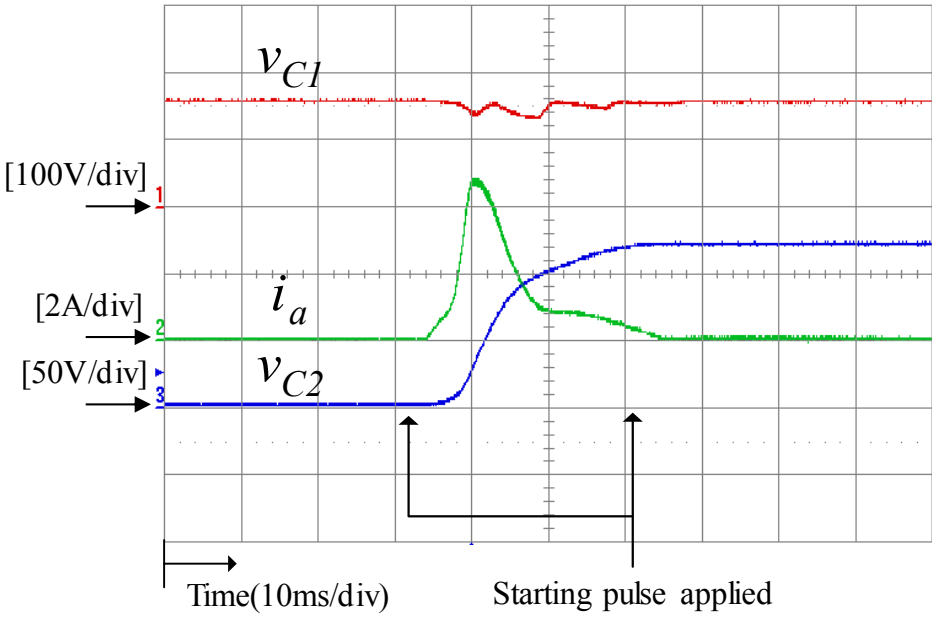

Fig. 4.13. Measured waveforms (v_{C1} : C1 voltage, i_a: phase A current, v_{C1} : C2 voltage) during initial charging of capacitor C2 by applying a starting pulse.

4.6.2 Drive System Control

Figs. 4.14(a) and (b) show the flowcharts of the control algorithms implemented in the proposed drive system. The overall drive system control shown in Fig. 4.14(a) is composed of three main parts: starting, main control loop, and V_{C2} monitoring. Once the motor starts, the controller executes the main control loop. The outermost loop is the speed control executed every 1ms, and the inner control loops are PI current control and phase commutation, which are executed at 20 kHz. Thus, the motor runs at a predefined speed command. Once the motor starts running, V_{C2} begins to decrease from its initially charged value and then reaches a steady-state value determined by the drive operating point. Although it has been experimentally found that V_{C2} settles within an acceptable level in most cases, careful monitoring of V_{C2} may be required in such conditions as low dc supply voltage or very low speed operations, where V_{C2} can be critically small and furthermore, the waveform of V_{C2} can be discontinuous. If V_{C2} becomes too small, C2 may not be able to supply sufficient energy for phase B excitation. In addition, too small V_{C2} means insufficient voltage for demagnetization of phase A; hence, a longer tail current

is present, which requires advancing the turn off position for phase A to prevent negative torque production.

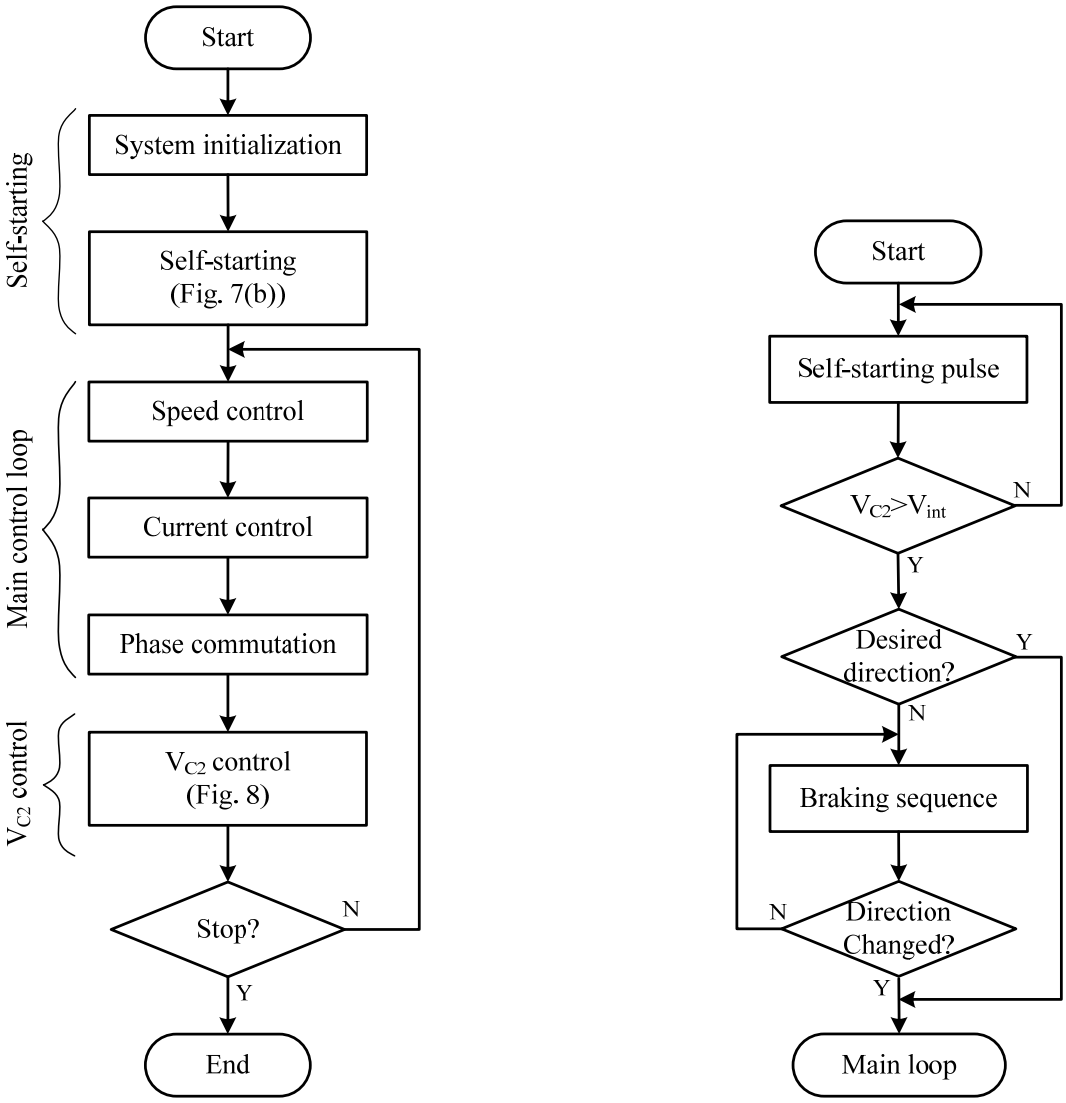

(a) Drive system control (b) Self-starting

Fig. 4.14. Flowcharts for control algorithms

A simple control scheme can be employed to control V_{C2} within a desired level. This scheme is illustrated in Fig. 4.15. When V_{C2} drops below the predetermined minimum value, V_k the difference is fed to a PI controller to generate a command signal which is added to or subtracted from the phase current command signal generated from the speed controller. Therefore, the final current command depends both on the speed command and V_{C2} level. Once V_{C2} becomes larger than the minimum value, the voltage controller is disabled until V_{C2} becomes smaller than V_k again.

Due to the unique machine topology, precise current control in phase B (auxiliary winding) is not essential in increasing the performance of the drive system, and hence the drive can be controlled by either single pulse operation or average voltage control with a fixed PWM chopping. This makes it possible to eliminate the current control of phase B in low cost applications and to some extent, the same may be applicable for phase A too.

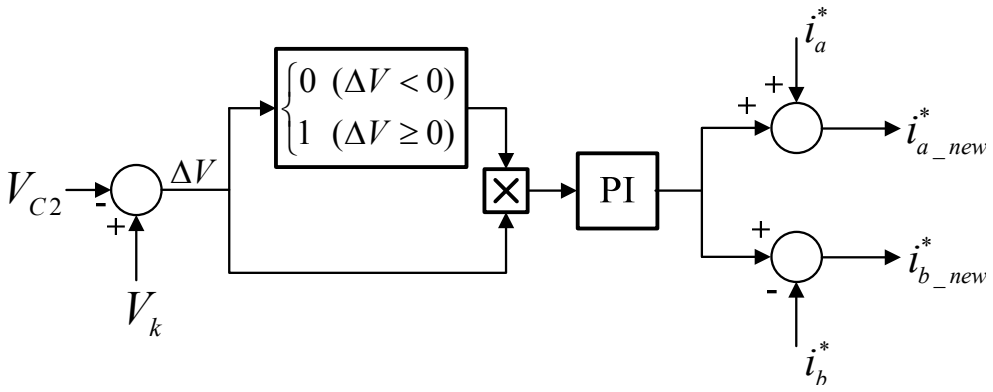

Fig. 4.15. Capcitor C2 voltage control.

4.7 Simulation Verification

The detailed simulation and experimental tests have been made to investigate performance of the proposed drive system. The nonlinear magnetization and torque characteristics of the prototype machine are modeled using finite-element analysis (FEA), and

simulation of the overall drive system including the non-ideal converter modeling and machine modeling interfaced with FEA has been achieved using software, called “Simplorer”. The rms ac main voltage is 120V and the capacitance of C1 and C2 is 1000uF. The simulated waveforms of currents and voltages for each phase running at 2000r/min are shown in Fig. 4.16. Hysteresis current control has been employed to simulate the drive system. As shown in Fig. 4.16, the dwell time for phase B is much shorter than phase A due to the unique machine structure of which the positive motoring region ($dL/d\theta > 0$) for phase B is much smaller than that of phase A. The large switching ripple in phase B current results from the very small time constant of phase B windings compared to phase A.

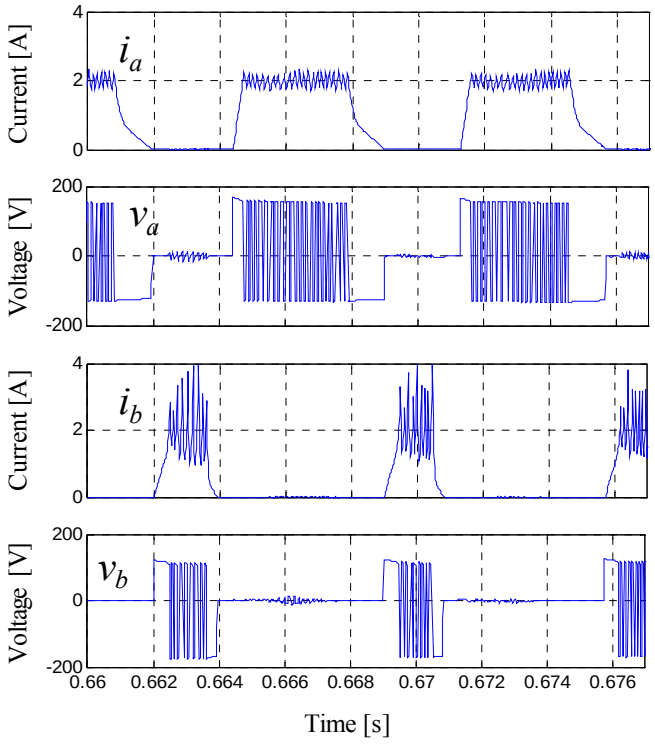

Fig. 4.16. Simulated results: Phase current and voltage waveforms of the drive system operating at 2000 r/min

4.8 Experimental Results

The prototype two-switch converter employed in the proposed drive system is shown in Fig. 4.17 and the experimental configuration to test the proposed drive system is shown in Fig. 4.18. The dc link voltage, V_{C1} is approximately 155V from the rectified ac main. The power switching devices for the converter are realized with 600V-15A ultra-fast IGBTs and fast-recovery diodes. Capacitors C1 and C2 are 1000uF electrolytic capacitors with a voltage rating of 450VDC. TMS320F2808 from Texas Instruments has been utilized to implement the drive control algorithms. Two Hall-effect sensors to estimate the rotor position and speed are mounted on two stator poles: one on a main pole, the other on an adjacent auxiliary pole. PWM based PI current and speed control scheme is employed. The sampling frequency is 20 kHz and speed control loop is executed every 1ms. Fig. 4.19 shows the measured waveforms of phase currents and voltages which are comparable to the simulated waveforms in Fig. 4.16. Waveforms at two operating speeds at 2000 r/min (Fig. 4.19) and at 4500 r/min (Fig. 4.20) were measured.

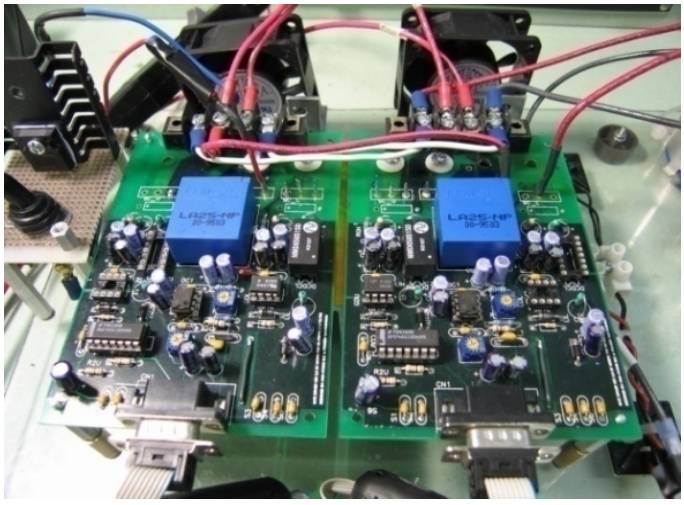

Fig. 4.17. Prototype two-switch-based buckboost converter

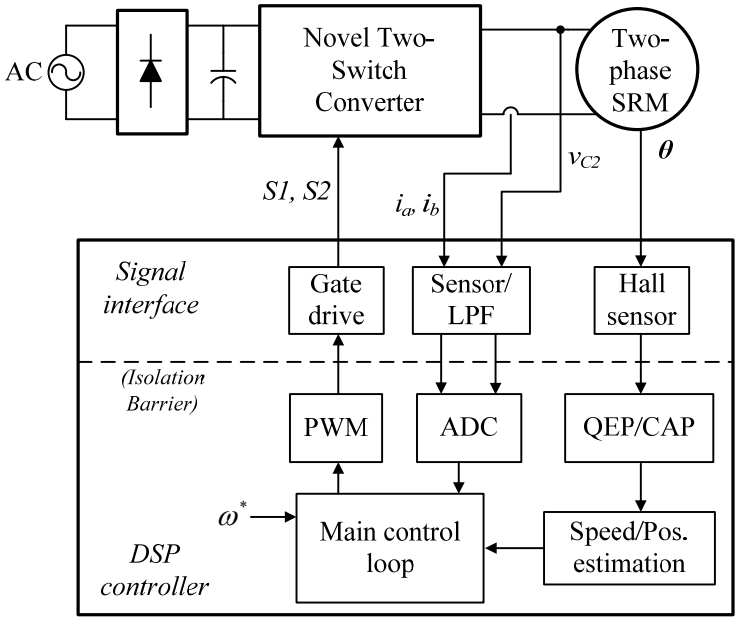

Fig. 4.18. Experimental configuration for prototype drive system

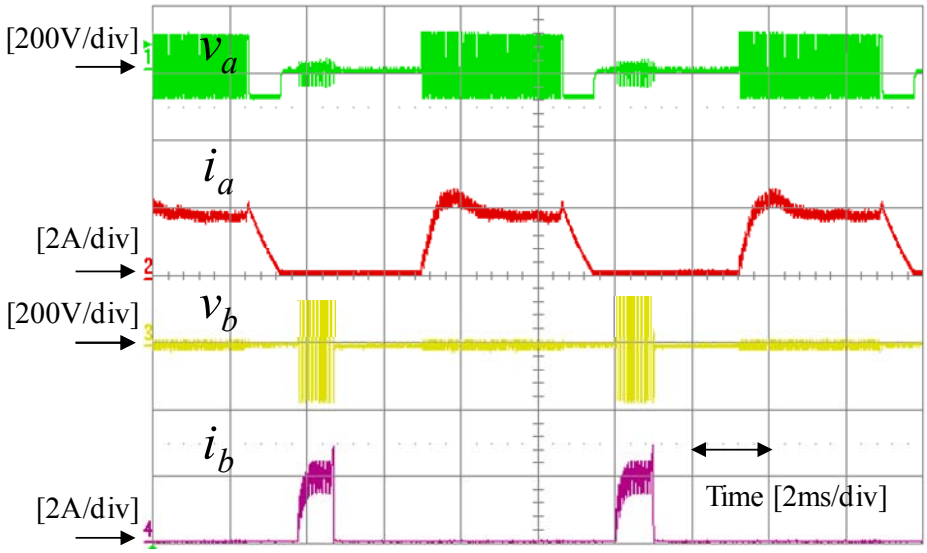

Fig. 4.19. Experimental results: Phase currents and voltages waveforms of the drive system operating at 2000r/min

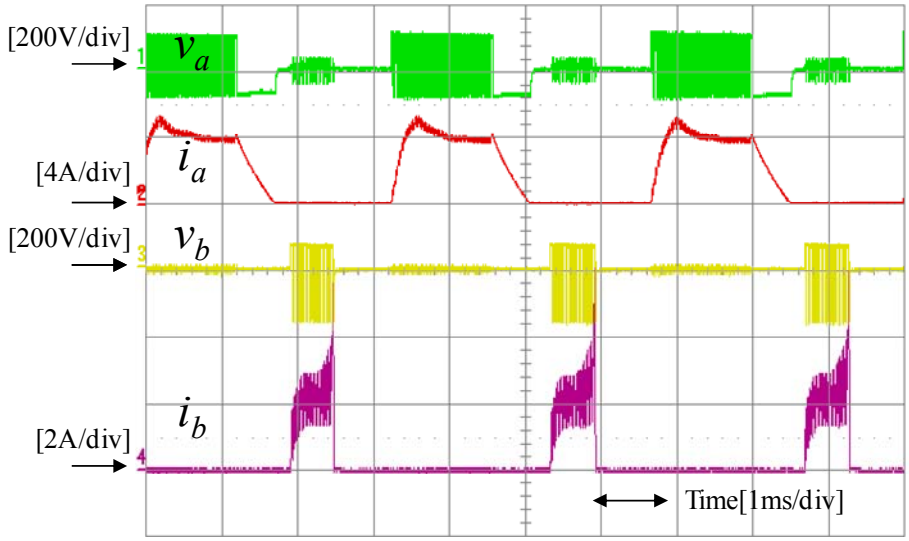

Fig. 4.20. Experimental results: Phase currents and voltages waveforms of the drive system operating at 4500r/min

4.9 Summary

A low cost two-switch based converter for a two-phase SRM has been proposed. The proposed converter drive system has been analyzed, designed, and implemented in a prototype form. The steady-state analysis of the converter has been made including: 1) capacitors voltage imbalance, 2) power transfer between C1 and C2, 3) estimation of C2 voltage. Simple starting and C2 voltage control has been implemented, and the steady-state and dynamic performance of the drive system have been experimentally demonstrated. The proposed converter drive system has following advantages and disadvantages:

Advantages

1) The proposed converter has a very low cost single-switch-per-phase configuration that leads to more compact packaging and cost reduction than conventional two-switch-per-phase converters.
2) Having only one switch per phase yields only one switch voltage drop per phase. This makes the converter suitable for low supply voltage applications.
3) The converter is inherently suited for two-phase SRMs having asymmetry in their

stator phases for self-starting and speed reversal purpose.

4) Compared to the single-switch converter, the proposed converter provides better control of phase currents. Thus, large torque ripple and reduced efficiency due to lack of auxiliary phase control in the single-switch drive can be improved.

Disadvantages

1) Fast current commutation of phase A may be limited by since the capacitor C2 voltage varies with the operation condition, and is likely to be less than V_{C1}.
2) Lower average torque is available than two-phase SRM drives with conventional two-switch-per-phase converter.

Although the proposed drive system has inherent voltage imbalance for each phase excitation and commutation due to the unique machine and converter structure, this will not be a hindrance if the drive is targeted for low cost high volume applications that are tolerant of torque ripple. The proposed low cost converter coupled with the two-phase SRM having four-quadrant-operation capability makes this drive a strong candidate for low cost high volume applications where both cost and performance are of primary concern.

Chapter 5

Proposed Drive System 3: Two-Controllable-Switch-Based SRM Drive For High-Speed Applications

5.1 Introduction

SRMs have been widely studied for low and medium speed applications ranging from servo drives to automotive applications [10]. However, application of SRM technology into the drives with high-speed, low-torque, and mass-production has not been explored in great detail hitherto. In this chapter, a switched reluctance drive targeting high-speed, low-cost, and high-volume applications such as vacuum cleaners, blowers, etc will be presented. SRMs are inherently suited for this kind of applications due to their highly reliable and inexpensive structure along with mechanical robustness and low inertia. The target subset of applications does not require precise torque control and can tolerate relatively large torque ripple while both cost and efficiency are of prime concern.

Due to the high-volume nature of these applications, cost minimization is of immense interest to industry. Conventional AC machines such as induction and permanent magnet (PM) machines are not cost effective in that they require more winding volume and/or permanent magnets when compared to SRMs, which increases their material and manufacturing cost. Although brushed dc- or ac series wound motors (a.k.a. universal motors) are widely used specifically in home appliances, their low efficiency and life-time and environmental issues of

the brush-commutator configuration become serious concerns. SRMs, however, are considered by many to be rugged, inexpensive, fault-tolerant, and capable of high-speed operation, hence opening up new opportunities for their selection into various applications.

This chapter presents the design and implementation of a high efficiency, low cost, brushless, variable speed drive system with high speed capability. The drive system is realized using a two-phase switched reluctance machine driven by a low cost split ac converter. The machine has self-starting capability at any rotor position and is capable of running at a rated speed up to 48,000r/min. The power converter has a low cost single-switch-per-phase (SSPP) configuration.

Accurate mathematical modeling of the drive system including machine and power electronic converter is described. Based on the derived model, the control system is designed and its optimal control strategy in single-pulse operation mode is investigated. To find the optimal switching angles in the single-pulse operation mode, three dimensional characteristics of the machine efficiency as well as electromagnetic torque in terms of the advance and commutation angles are developed from dynamic simulations. Optimization of the winding turns in the stator is an important design aspect for SRMs and thus a study to find the optimal number of winding turns considering motor efficiency and power converter ratings is also presented.

Dynamic simulation results are presented to validate the operation of the proposed drive system. Experimental verification of the prototype drives system and its correlation with analytical and simulation results are presented. First, static measurements of the winding inductance and torque are carried out to correlate the obtained from the FEA simulation. In addition, a full load test with a dynamometer setup has been performed to verify both steady-state and dynamic performance of the proposed drive system.

The proposed drive system offers viable features such as low cost structure, high efficiency, high reliability, and high speed capability and hence it can be a strong candidate for a low cost brushless variable (high) speed application in low-cost, mass-production markets, where both cost and efficiency are valued.

5.2 Proposed Drive System

5.2.1 Machine

Fig. 5.1 shows the prototype two-phase SRM of the proposed drive system. The motor is a two-phase self-starting capable SRM with four stator poles and two rotor poles. It is designed to run at rated speed of 38,000r/min and up to maximum speed of 48,000r/min. Although single-phase SRMs are less expensive, recent research [10]-[13] shows that two-phase SRMs are preferred from the viewpoint of performance, such as self-starting, better air-gap utilization, lower torque ripple, and less acoustic noise. Figs. 5.2(a) and 5.2(b) show the phase inductance and torque profiles, for designed two-phase SRM respectively, for one electrical cycle obtained from finite element analysis (FEA). In order to produce starting torque at every rotor position, at least one phase should be able to produce positive torque at any rotor position, i.e. the positive inductance slope ($dL/d\theta > 0$) region should overlap for both phases, as shown in Figs. 5.2 (a) and 5.2(b). This is achieved by increasing the rotor pole arc and creating a non-uniform air-gap via rotor pole arc shaping.

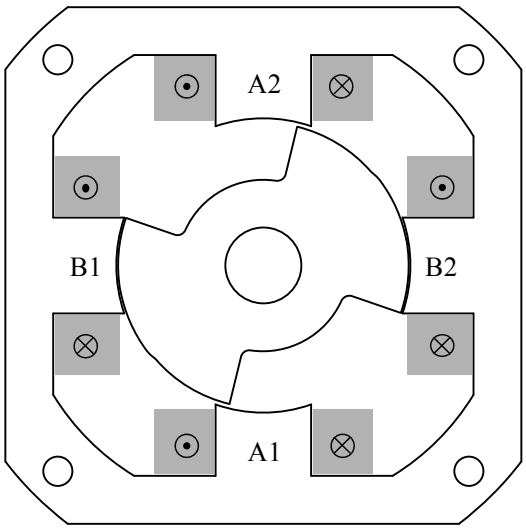

Fig. 5.1 Prototype two-phase 4/2 SRM

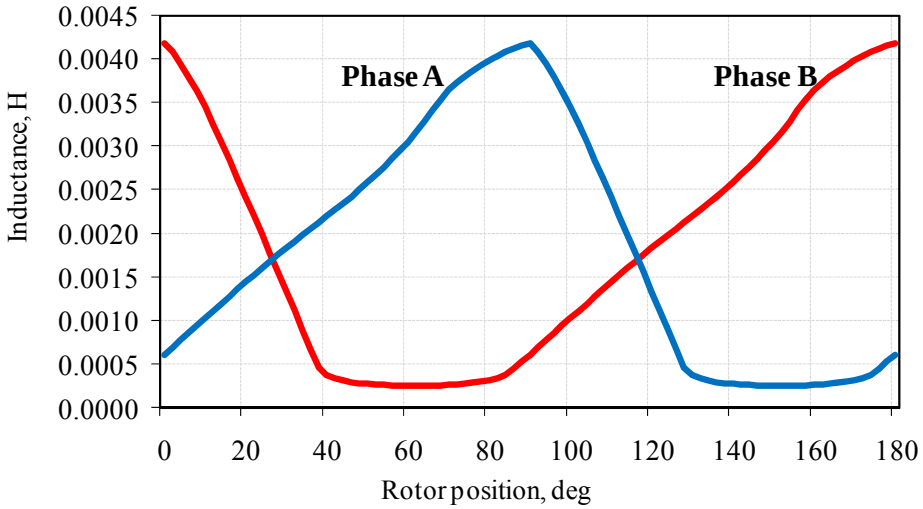

(a) Inductance

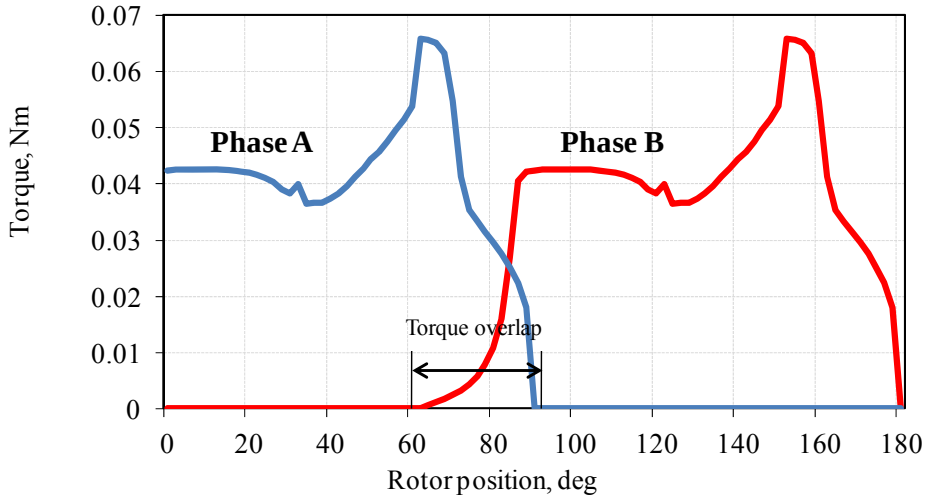

(b) Torque

Fig. 5.2. Static inductance and torque profiles for each phase at 6A current to provide self-starting capability at any position

5.2.2 Power Converter

The low cost split ac supply converter [35], [36] as shown in Fig. 5.3 has been chosen to drive the machine. The converter employs a single-switch-per-phase topology that leads to a reduced heat sink area and compact packaging due to low component count. Originally evolved from the well-known split dc converter, the power converter employs a half-bridge rectifier splitting the ac supply and the dc link mid-point is tied to the ac neutral. Therefore, the dc link

capacitors are charged separately during alternate ac half cycles i.e. one capacitor is charged during the positive ac cycle and the other capacitor is charged during the negative ac cycle. The split ac converter has a better voltage balance between the two capacitors than split dc converter because of independent charging of the two dc capacitors. Moreover, each capacitor has full dc supply voltage as opposed to half supply voltage in the split dc case. These advantages result in better power utilization and faster current commutation in the split ac converter system.

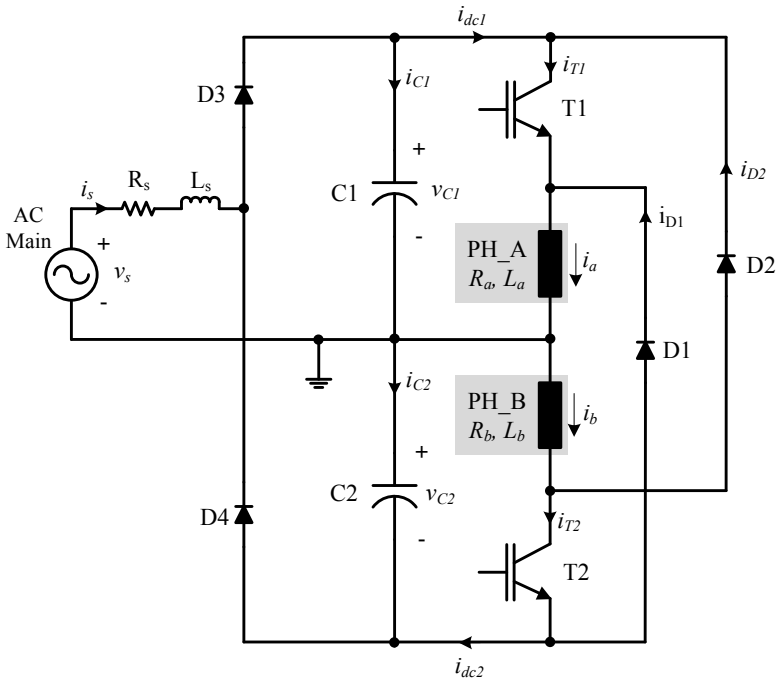

Fig. 5.3 Split ac supply converter.

5.3 Modeling and Derivation of Drive System Equations

The block diagram in Fig. 5.4 shows the overall model of the drive system including input-side electrical systems, magnetic characteristics, torque characteristics, and mechanical system for torque-speed dynamics. Three-dimensional nonlinear characteristics of flux linkage vs. current and rotor position as well as torque vs. current and rotor position are obtained from FEA simulations and they are plotted in Figs. 5.5 and 5.6 respectively. Neglecting mutual coupling between phase windings, the phase voltage equation is given by

$$v_{ph} = R_{ph} i_{ph} + \frac{d\lambda_{ph}(\theta, i_{ph})}{dt} \tag{5.1}$$

where v_{ph} is applied phase voltage, R_{ph} is phase resistance, λ_{ph} is phase flux-linkage, θ is rotor position, and i_{ph} is phase current. From (5.1), the phase flux linkage is expressed by

$$\lambda_{ph} = \int (v_{ph} - R i_{ph}) dt \tag{5.2}$$

With the calculated flux linkage, the current at each rotor position can be obtained from magnetic characteristics in the form of a reverse look-up table, $i(\lambda,\theta)$ as shown in Fig. 5.4. With the phase current known at every rotor position, the air-gap torque is obtained via a torque characteristics look-up table, $T_e(i,\theta)$, therefore flux linkages and torque are known at any rotor position. The model of the mechanical load

$$T_e = J \frac{d\omega_r}{dt} + B\omega_r + T_L \tag{5.3}$$

where J, B, and T_L are the rotor inertia, friction coefficient, and load torque respectively.

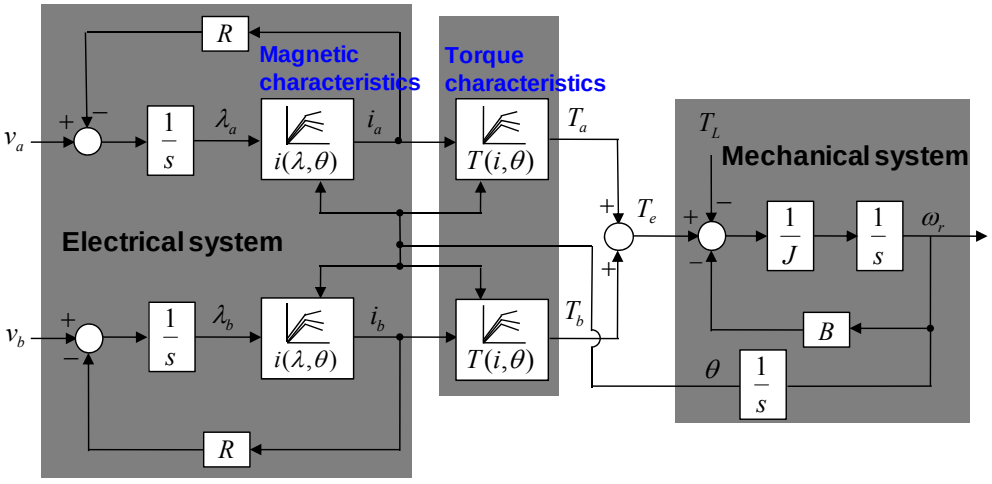

Fig. 5.4. Modeling of the two-phase SRM

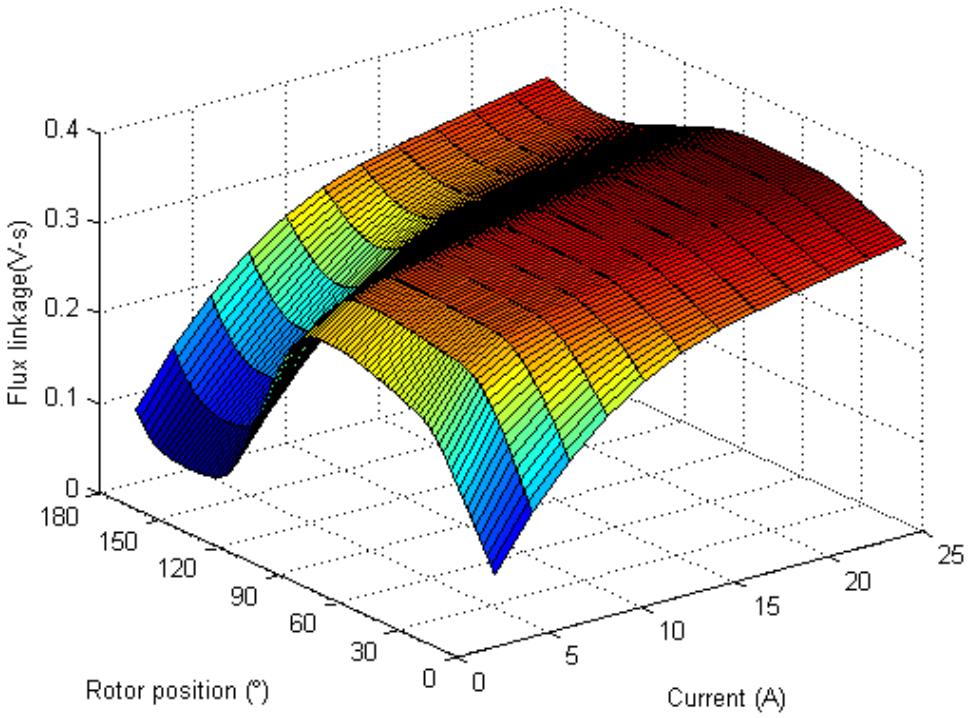

Fig. 5.5. Magnetic characteristics for the two-phase 4/2 SRM

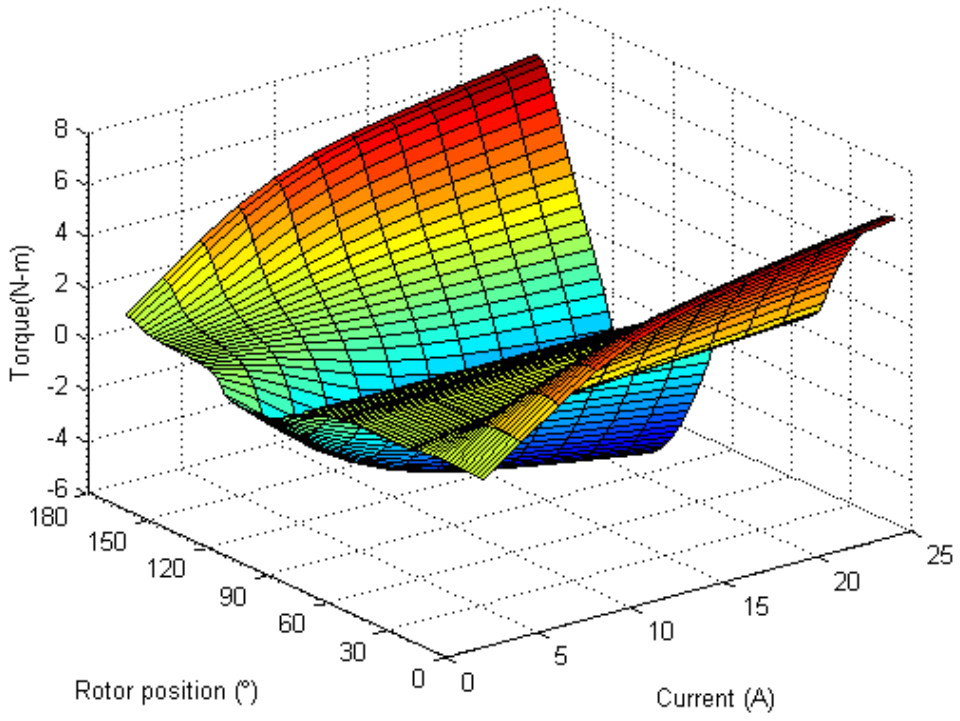

Fig. 5.6. Torque characteristics for the two-phase 4/2 SRM

As shown in Fig. 5.3, the power converter differs from the asymmetric converter in that it has two dc link capacitors supplying energy to each phase independently. The capacitors generally have a larger voltage ripple than that of the asymmetric converter since each capacitor is charged only during the positive or negative ac cycle, respectively. Both capacitors C1 and C2 are also charged from the energy obtained from demagnetization of the opposing phase.

Power converter modeling often considers the circuit to be ideal and constant dc link voltage is used for simplicity. Detailed modeling of the power converter is required for accurate simulations. Analytical modeling of the converter including the input side rectifier stage is described as follows: State equations for capacitors C1 and C2 and source line inductance L_s are given by

$$\frac{dv_{C1}}{dt} = \begin{cases} \frac{1}{C1}\left(\frac{v_s - v_{Ls} - V_D - v_{C1}}{R_s} - i_{dc1} \right) & \left(v_s > v_{C1}\right) \\ -\frac{i_{dc1}}{C1} & \left(v_s \le v_{C1}\right) \end{cases} \tag{5.4}$$

$$\frac{dv_{C2}}{dt} = \begin{cases} \frac{1}{C2}\left(\frac{-v_s - v_{Ls} - V_D - v_{C2}}{R_s} - i_{dc2} \right) & \left((-v_s) > v_{C2}\right) \\ -\frac{i_{dc2}}{C2} & \left((-v_s) \le v_{C2}\right) \end{cases} \tag{5.5}$$

$$\frac{di_s}{dt} = \frac{v_{Ls}}{L_s} \tag{5.6}$$

where v_s is ac input voltage, i_s is ac input current, R_s is ac line resistance, L_s is ac line inductance, v_{Ls} is source inductive voltage drop, V_D is the forward voltage drop of the rectifier diode, v_{C1} and v_{C2} are capacitor C1 and C2 voltages respectively, and i_{dc1} and i_{dc2} are dc link currents respectively. Current equations are given by

$$i_{dc1} = i_{T1} - i_{D2} \tag{5.7}$$

$$i_{dc2} = i_{T2} - i_{D1} \tag{5.8}$$

$$i_{T1} = S_1 i_a \tag{5.9}$$

$$i_{T2} = S_2 i_b \tag{5.10}$$

$$i_{D1} = (1 - S_1) i_a \tag{5.11}$$

$$i_{D2} = (1 - S_1) i_b \tag{5.12}$$

where i_{T1} and i_{T2} are transistor T1 and T2 currents, i_{D1} and i_{D2} are diode D1 and D2 currents, i_a and i_b are phase currents, and $S_1$and S_2 are switching functions of transistors T1 and T2. Turning on T1 and T2 results in v_{C1} and v_{C2} being applied to phase A and B windings, respectively, for magnetization. Turning off T1 and T2 causes -v_{C2} and -v_{C1} to be applied to phase A and B windings, respectively, for demagnetization. Therefore, the terminal voltage applied to each phase is given by

$$v_a = S_1 (v_{C1} - V_T) - (1 - S_1)(v_{C2} - V_D) \tag{5.13}$$

$$v_b = S_2 (v_{C2} - V_T) - (1 - S_2)(v_{C1} - V_D) \tag{5.14}$$

$$S_x = \{0 \quad 1\}, \quad x = 1 \text{ or } 2 \tag{5.15}$$

where V_T is transistor saturation voltage, V_D is the diode forward drop, and S_x is the switching function for transistor T1 or T2.

5.4 Converter Modes of Operation

Although the converter circuit looks simple, thorough understanding of the converter operation may be complicated. Unlike the conventional asymmetric converter with only a single dc link, the split ac converter has two capacitors forming two separate dc link for each phase. The mid-point of these capacitors is tied with the negative ac rail and thus each capacitor is charged during only half ac cycle respectively. In addition, each phase experiences different capacitors for magnetization and demagnetization respectively. All of these add to complexity of the converter operation. Examining all the possible switching states of T1 and T2 as well as the charging and discharging status of C1 and C2 with respect to ac cycle, six different modes of operation can be derived for each phase and they are depicted in Fig. 5.7 and 5.8. Proper understanding of the converter operation is important for capacitor sizing as well as the reliable starting scheme.

	Phase A magnetization (T1 on)	Phase A demagnetization (T1 off)
Positive ac main charging C1	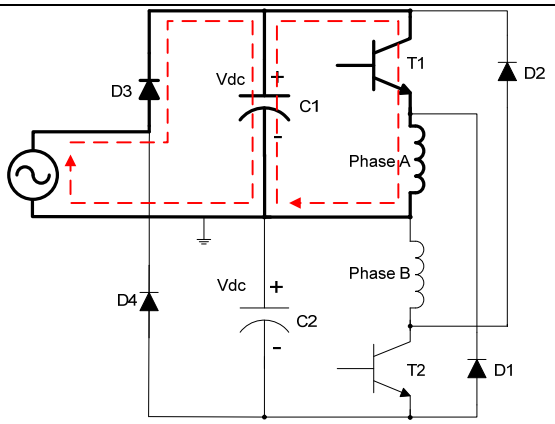 Mode A1 ($v_{in} > v_{C1}$, T1 on)	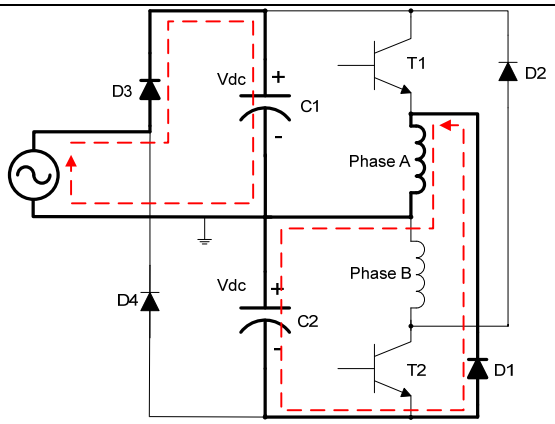 Mode A2 ($v_{in} > v_{C1}$, T1 off)
Negative ac main charging C2	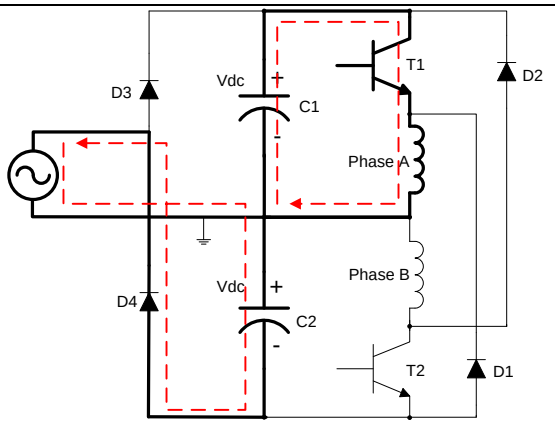 Mode A3 ($-v_{in} > v_{C1}$, T1 on)	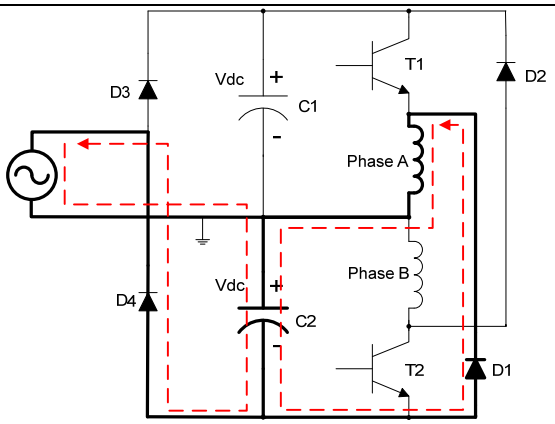 Mode A4 ($-v_{in} > v_{C1}$, T1 off)
Ac main not charing C1 or C2	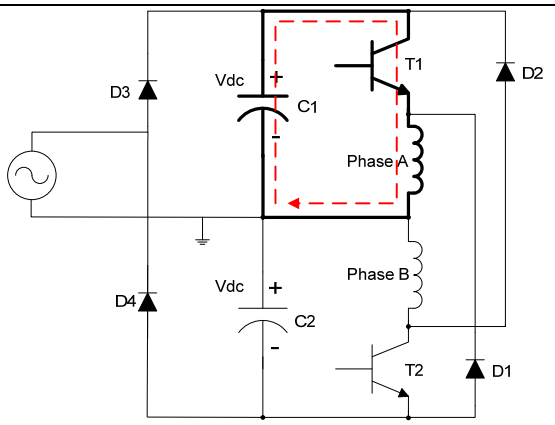 Mode A5 ($\lvert -v_{in}\rvert < v_{C1}$ or $\lvert -v_{in}\rvert < v_{C2}$, T1 on)	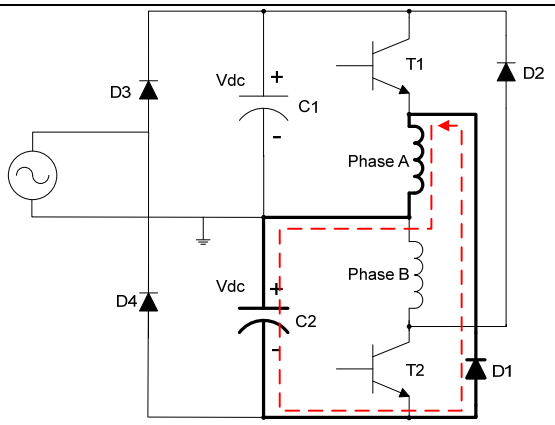 Mode A6 ($\lvert -v_{in}\rvert < v_{C1}$ or $\lvert -v_{in}\rvert < v_{C2}$, T1 off)

Fig. 5.7 Converter modes of operation for phase A excitation

	Phase B magnetization (T2 on)	Phase B demagnetization (T2 off)
Positive ac main charging C1	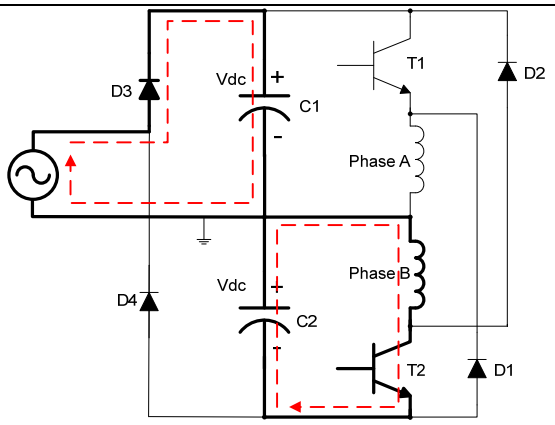 Mode B1 ($v_{in} > v_{C1}$, T2 on)	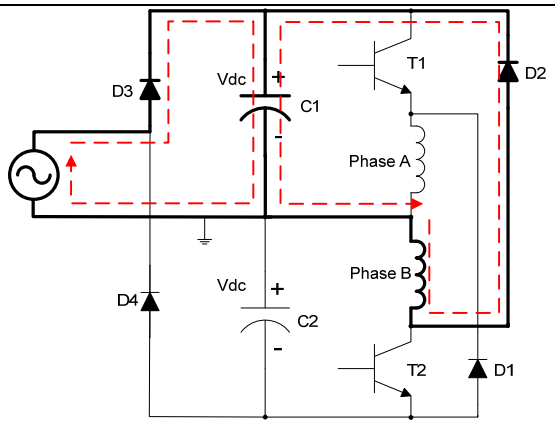 Mode B2 ($v_{in} > v_{C1}$, T2 off)
Negative ac main charging C2	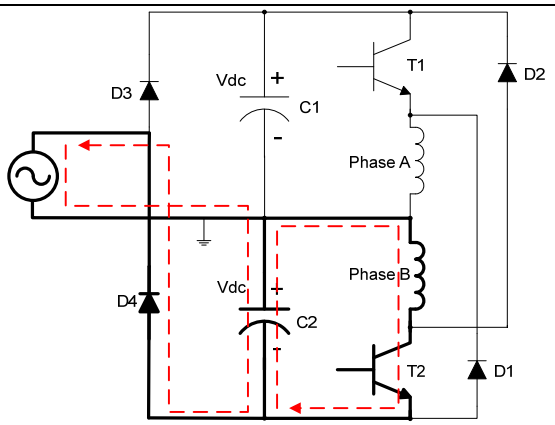 Mode B3 ($-v_{in} > v_{C1}$, T2 on)	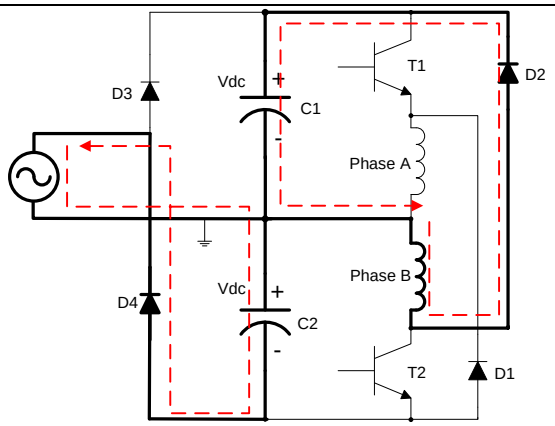 Mode B4 ($-v_{in} > v_{C1}$, T2 off)
Ac main not charing C1 or C2	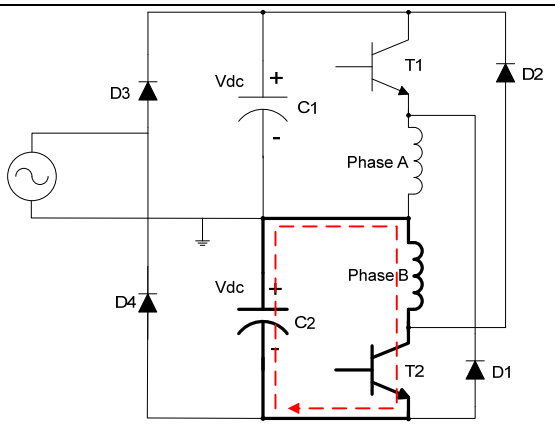 Mode B5 ($\lvert -v_{in}\rvert < v_{C1}$ or $\lvert -v_{in}\rvert < v_{C2}$, T2 on)	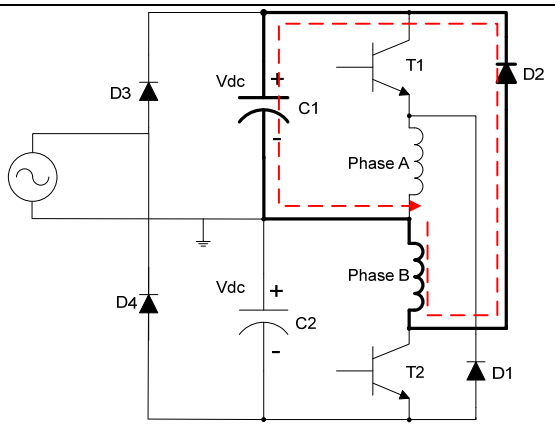 Mode B6 ($\lvert -v_{in}\rvert < v_{C1}$ or $\lvert -v_{in}\rvert < v_{C2}$, T2 off)

Fig. 5.8 Converter modes of operation for phase B excitation

5.5 Optimal Efficiency Control of SRM Drives in Single-Pulse Operation

5.5.1 Switching Angle Control

The control scheme presented here is to achieve optimal efficiency for a given operating condition. The key to achieving optimal efficiency is to maximize the energy conversion per phase excitation, i.e. the ratio of average torque to rms phase current. At given speed, mechanical output is proportional to the average output torque, and the electrical input is proportional to the rms phase current. The motor drive of interest is intended to run at high speeds where current control is infeasible; therefore, the drive system will be running in single-pulse mode. In single-pulse mode, the switching angles (turn-on, turn-off) defined in Fig. 5.9 are the only control parameters and thus, the proper firing of the excitation will play a key role for the optimal efficiency control.

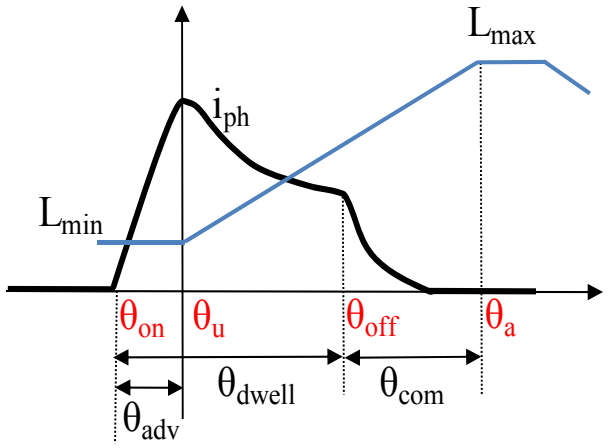

$$\theta_{on} = \theta_u - \theta_{adv}$$

$$\theta_{off} = \theta_a - \theta_{com} = \theta_{on} + \theta_{dwell}$$

θ_u	Aligned rotor position with minimum inductance.
θ_a	Unaligned rotor position with maximum inductance.
θ_{on}	Rotor position at which the switch is turned on.
θ_{off}	Rotor position at which the switch is turned off.
θ_{dwell}	Position interval between turn-on and turn-off angle.
θ_{adv}	Position interval between unaligned and turn-on angle.
θ_{com}	Position interval between aligned and turn-off angle.

Fig. 5.9. Switching angles and typical phase current waveform in single–pulse operation mode

As shown in Fig. 5.7, beyond unaligned position, θ_u, when the back-EMF exceeds the supply voltage the phase current is forced to decrease during conduction. Therefore, in order to produce the desired torque, it is necessary to advance the turn-on of phase excitation substantially and to adjust the turn-off angle before the significant braking torque is produced.

5.5.2 Conventional Switching Angle Control

A conventional method to find an optimal turn-on angle is based on the phase voltage equation [37]. Neglecting mutual coupling between the phases, the phase voltage equation of the SRM is given by

$$v_{ph} = Ri_{ph} + L\frac{di_{ph}}{dt} + i_{ph}\frac{dL}{d\theta}\omega \tag{5.16}$$

The optimal turn-on angle is defined such that advancing the turn-on makes the current builds up fast at unaligned region and reaches its reference value at the start of pole overlap, and it can be calculated using (5.16). The back-EMF is zero at unaligned position and at low speed IR drop of the stator resistor is negligible compared to source voltage. Thus, the voltage equation reduces to

$$v_{ph} = L\frac{di_{ph}}{dt} = L\omega\frac{\Delta I}{\Delta\theta} \tag{5.17}$$

In order for the phase current to reach its reference value, I_{ref} at θ_u, the required advanced angle can be calculated by

$$\theta_{adv} = \frac{\omega L_{\min} I_{ref}}{V_{dc}} \tag{5.18}$$

where L_{min} is the inductance at unaligned position and V_{dc} is dc supply voltage. Therefore, the turn-on angle is

$$\theta_{on} = \theta_u - \frac{\omega L_{\min} I_{ref}}{V_{dc}} \tag{5.19}$$

Above estimation, however, is not accurate at higher speed since the available source voltage is not sufficient to generate the commanded current due to the back-EMF comparable to the source voltage. Therefore, further advancing of turn-on angle is needed. To ensure that the correct advance angle is achieved under higher speed region, several methods in a form of closed-loop angle controller have been developed [37]-[42]. Fig. 5.8 shows one of the simple algorithms for angle compensation methods. With insufficient advancing of excitation, the current cannot reach I_{ref} at θ_u, and it continues to increase beyond θ_u. Then, the angle detector captures the rotor position, θ_p at instant when the measured phase current first matches I_{ref}. Then, the feedback controller fine-tunes θ_p to match θ_u is added to initial estimation of advance angle. However, in high-speed single-pulse operation mode, the above method may not be very accurate since the current cannot be maintained at the reference value beyond θ_u.

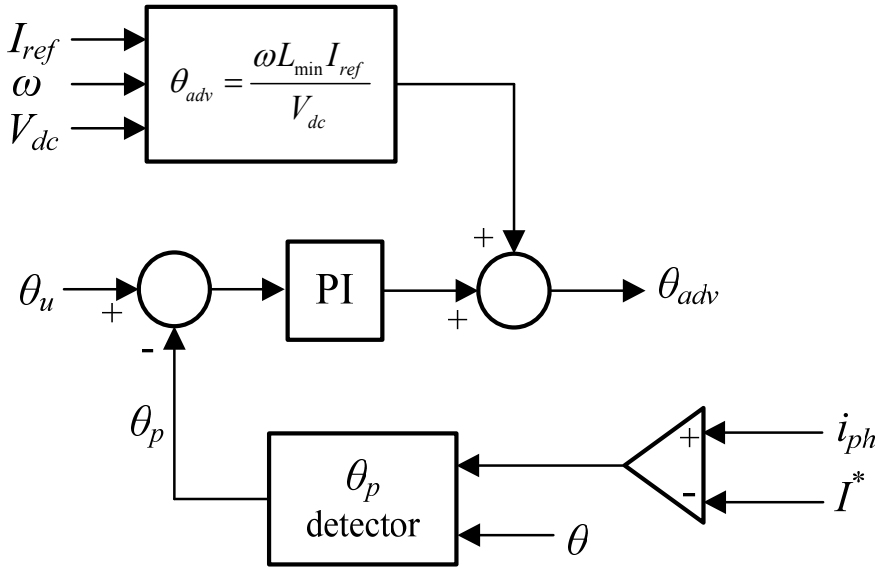

Fig. 5.10. Closed-loop angle controller

The turn-off angle is more difficult to determine directly than turn-on angle and it is often obtained from trial-and-error experimental data or a piece-wise linear model neglecting magnetic saturation. From the experimental or simulation data, the turn-off angle can be represented analytically [41], [42]

$$\theta_{off} = k_1\omega + k_2 I_{ref} + k_3\omega I_{ref} + k_4 \tag{5.20}$$

where k_1, k_2, k_3, and k_4 are curve fit parameters.

5.5.3 Proposed Angle Control Scheme Based on Characterization of Optimal Switching Angles in Single-Pulse Operation

As described in the previous sections, the optimal torque production for maximum efficiency can be achieved by properly selecting both turn-on and turn-off angles. Figs. 5.11 and 5.12 show various phase current waveforms for different switching angles at the same speed. The effect of variation of turn-on angle with a constant turn-off is shown in Fig. 5.11, and the effect of variation of turn-off angle with a constant turn-on is shown in Fig. 5.12, respectively. As shown in Fig. 5.11, the more turn-on angle is advanced, the faster and higher rise of the phase current is possible due to small inductance and negligible back-EMF, hence facilitating torque production. As can be seen from Fig. 5.12, if the turn-off angle is delayed, i.e. increased dwell angle, more torque is produced but not as much as advancing the turn-on angle due to the substantial back-EMF and inductance at this interval. Therefore, it can be inferred that turn-on angle has more impact on torque production than turn-off angle.

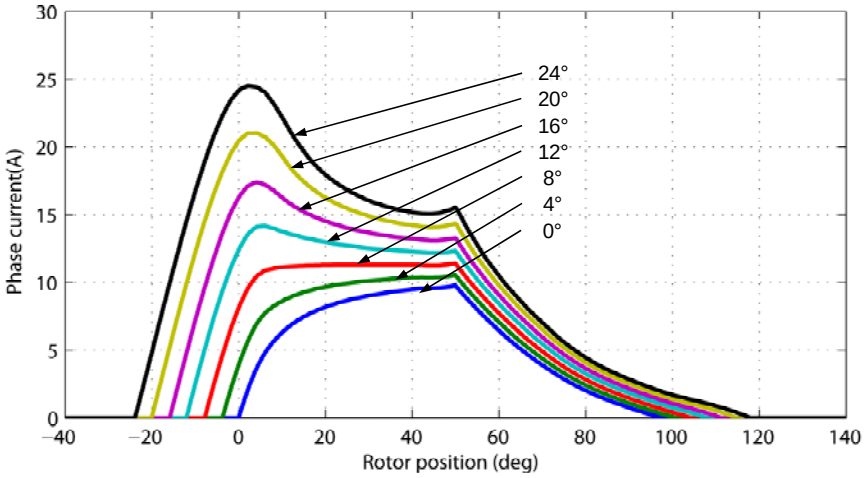

Fig. 5.11. Effect of turn-on angle on phase excitation current

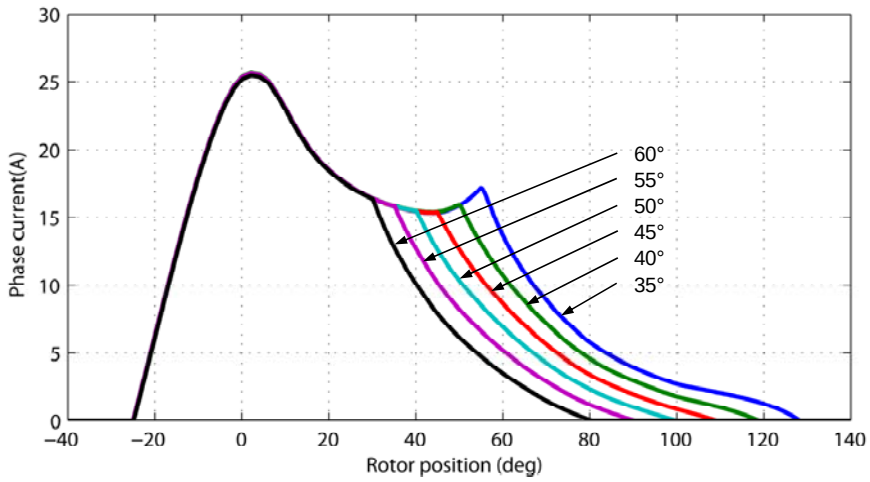

Fig. 5.12. Effect of turn-off angle on phase excitation current

Fig. 5.13 shows several possible choices of switching angles to produce the same average torque. Although they produce the same torque, their rms currents are different. Therefore, an angle combination (turn-on and turn-off) resulting in minimum rms current is the optimal operating condition for maximum efficiency. As can be seen from current waveform, (1) in Fig. 5.13, a substantial advance of turn-on angle allows higher peak current at θ_u facilitating torque

production during the dwell period; however, the current during the advanced angle region does not contribute any torque but increases copper loss. Therefore, advance of turn-on angle needs to be reduced but this requires delay of turn-off angle, i.e. increased dwell interval, to sustain the same torque. However, this may increase peak flux linkage and thereby iron loss [37]. In current waveform, (3), too late turn-off may produce substantial braking torque that will affect the efficiency. Therefore, considering trade-off between case (2) and case (3), the current waveform (3) has been found to have the angles for optimal efficiency.

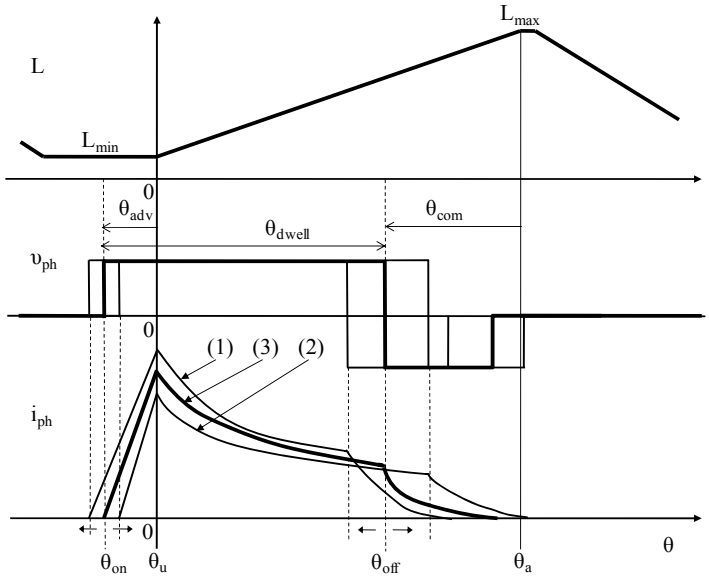

Fig. 5.13. Several possible switching angle sets for the same torque production

However, it is not a simple task to find optimal angles for various operation conditions. Therefore, both torque and efficiency characteristics in term of the switching angles are investigated to find the optimal angles for maximum efficiency at a given operating point. They are obtained from dynamic simulations for various switching angle combinations.

To find the optimal angles for maximum efficiency at the rated operating point, the three-dimensional characteristics of the estimated motor efficiency and torque as functions of the advance and commutation angle are investigated using extensive dynamic simulations and plotted in Fig. 5.14. First, in Fig. 5.14(a), find a set of angles where the same average-torque is

produced. Then, from these angles, the angle that gives the maximum efficiency in Fig. 5.14(b) is identified.

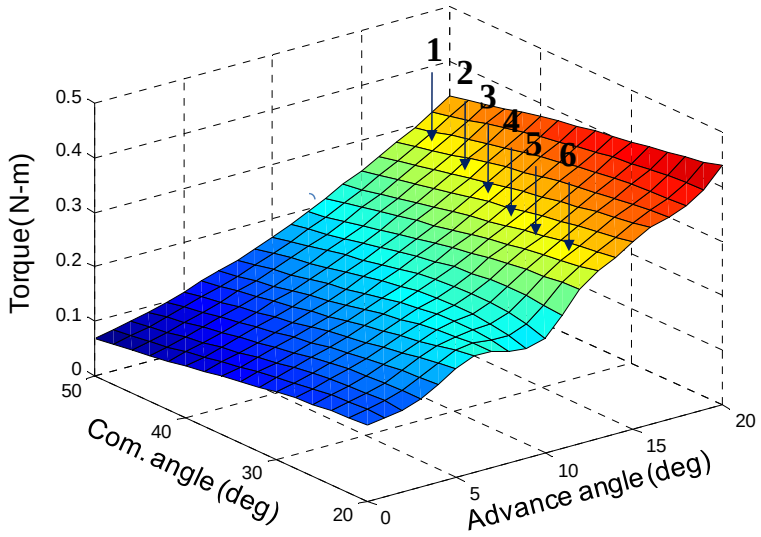

(a)

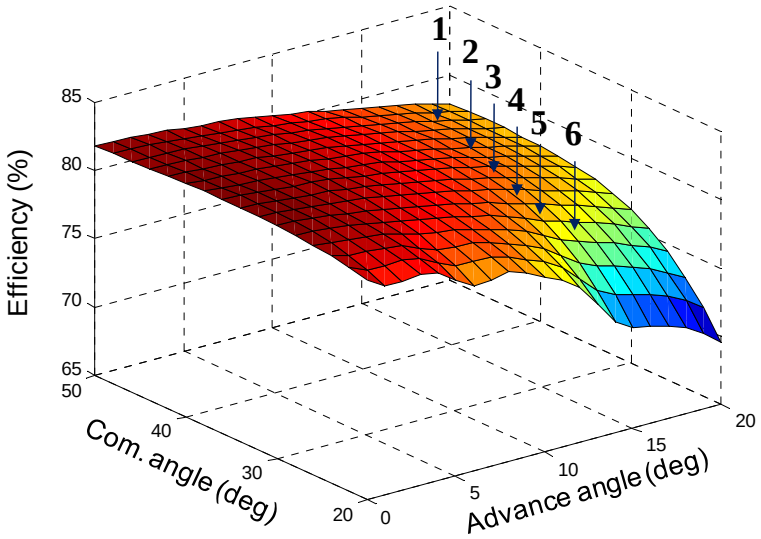

(b)

Fig. 5.14. Three-dimensional characteristics of (a) electromagnetic torque and (b) efficiency with respect advance and commutation angles

In Figs. 5.14(a) and 5.14(b), the three-dimensional characteristics of the estimated motor efficiency and torque as functions of the advance and commutation angle are plotted. Spline interpolation was utilized for curve-fitting to discrete data points. From Fig. 5.14(a), first find a set of angles where the same average-torque is produced. Then, from these angles, the angle that gives the maximum efficiency in Fig. 5.14(b) is identified. This optimum angle produces the required torque with maximum efficiency. For example, the 3D plot in Fig. 5.14(a) indicates 6 sets of switching angles, 1, 2, 3…6, which produce the same average torque. From Fig. 5.14(b), it is observed that angle set #2 ($\theta adv = 16°$, $\theta com = 42°$) has the highest efficiency and that efficiency is more sensitive to advance angle than commutation angle. These angle-torque and angle-efficiency characteristics can be used to design a simple low cost controller that is tuned off-line.

5.6 Drive System Controller

The closed-loop speed controlled drive system is illustrated in Fig. 5.15. Two common modes of operation are used in SRM drives, namely, PWM current control and single pulse control. PWM control is used when the motor speed is below the base speed and single-pulse control is used beyond the base speed as the back-EMF is comparable to the dc supply voltage in this regime. In general, maximum efficiency is achieved in the single-pulse mode around the rated operating point. The targeted operating speed of the proposed SRM is high with maximized efficiency where only average torque is controlled; hence the motor will be operating with single pulse control most of the time. However, both PWM current controller and single-pulse controller have been developed to extend the drive's operational capability.

In Fig. 5.15, the outer loop is a PI speed control and the inner control loop has two alternative controllers implemented, namely, a PWM current controller for low and medium speed regime and a single-pulse controller for high speed regime. The drive controller operates as follows. If the commanded speed is below the base speed, the machine runs under current-control mode as illustrated in the upper part of the inner control loop in Fig. 5.15. The reference torque is achieved by increasing the current amplitude and shifting the switching angles as a function of speed and current command using estimation for advance angle in (5.18). For high

efficiency operation, the advance angle is chosen to be minimum that is required to reach the commanded current at start of the positive torque region.

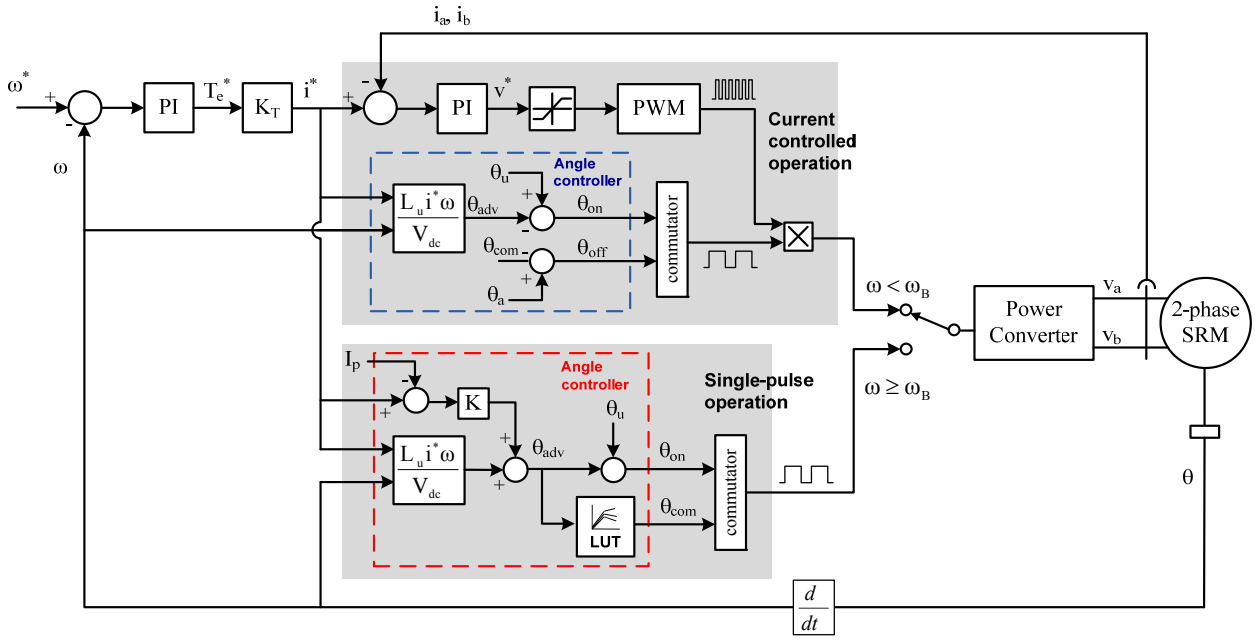

Fig. 5.15. Overall drive system control block diagram

If the commanded speed is larger than the base speed, the drive system goes into single-pulse control mode as the single-pulse controller is more efficient and is illustrated in the lower part of the inner control loop in Fig. 5.15. The output of the speed controller, i.e. the current command is directly fed to the angle controller to calculate the optimal turn-on angle. At high speeds, the available source voltage may be insufficient to generate the required commanded current since the back-EMF approaches the source voltage. Therefore, the turn-on angle estimation in (5.19) is not accurate in the high speed regime. Hence, the advance angle needs to be further increased. A simple compensation method [39] is used to determine the advance angle such that the first phase current peak occurs at the position θ_u by monitoring the phase current and compensating the difference between the peak and the command to adjust the advance angle. The turn-off angle, also an important control parameter is determined such that turning off

sooner allows the current decay fast before preventing the production of excessive braking torque. The turn-off angle for the drive controller is determined by the characterization described in the previous section.

5.7 Selection of Optimal Number of Winding Turns

One of the important SRM design factors which affect motor efficiency is the number of turns in the phase winding and thus the optimal number of turns is determined so that the maximum efficiency is achieved for given rated torque and speed. Fig. 5.16 shows a cross-sectional view of a stator pole and winding mounted around it.

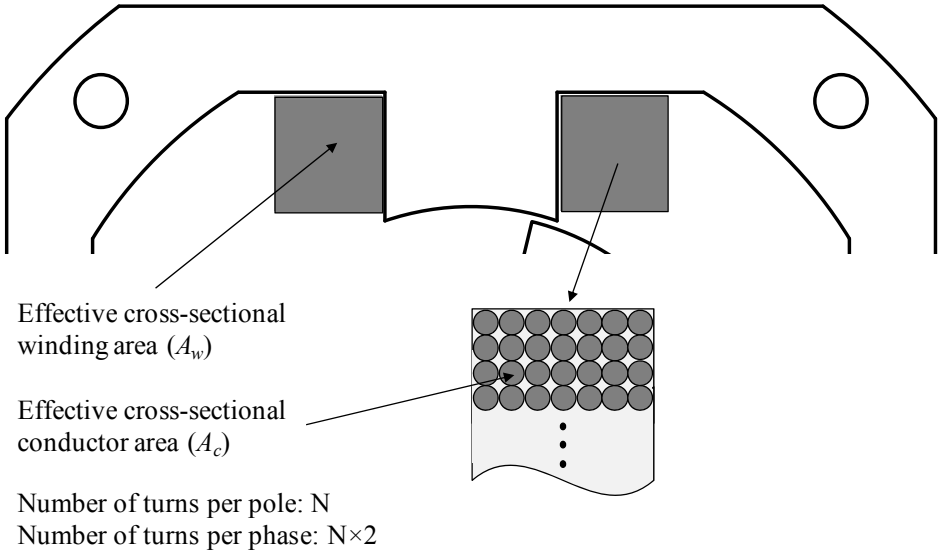

Fig. 5.16. Cross-sectional view of a winding mounted on a stator pole

Assuming that a rectangular cross-sectional area around a stator pole in Fig. 5.16 is the maximum effective winding area, the conductor sizes were chosen such that each combination of size and number provides approximately the same conductor area. The cross-sectional winding area A_W assumes a rectangular winding slot area and is expressed as

$$A_W \approx N \cdot A_C \cdot f_W \tag{5.21}$$

where N, A_C, and f_w are the number of turns, wire cross-sectional area, and fill factor ($0.5 < f_w < 0.8$) respectively. The phase winding resistance is calculated by scaling one turn's resistance by the number of turns.

$$R_{ph} = \left(\rho \frac{l_m}{A_C} \right) \cdot 2 \cdot N \tag{5.22}$$

l_m is a mean-length of one turn. Once the resistance of the initial winding, R_1, is determined, the resistance of different winding numbers, R_2 is calculated using

$$R_2 \approx R_1 \cdot \frac{N_2}{N_1} \cdot \frac{A_{C1}}{A_{C2}} \tag{5.23}$$

The resistances for a range of winding turns were calculated and a single-pulse mode simulation was performed at the rated operating point for each turns count. Table 5.1 shows the predicted performance at the rated operating point obtained from dynamic simulations for different number of turns per stator pole including the phase resistance R_{ph}, phase rms current I_{rms}, converter power loss P_{conv} and winding copper loss P_{cu}. A larger number of turns increases the phase resistance and inductance, and retards the current build-up at turn-on in single pulse mode. As shown in Fig. 5.17, an increase in the advance angle is necessary to increase phase current to compensate for the higher inductance and resistance. Since the excitation occurs where $dL/d\theta \approx 0$, it does not contribute any torque but increases copper loss. Therefore increasing the number of turns at the upper range of turn count is detrimental to the efficiency.

Table 5.1

Predicted losses for different number of turns

Number of turns	R_{ph} [Ω]	I_{rms} [A]	P_{conv} [W]	P_{cu} [W]	Total loss [w]
30	0.248	13.02	28.41	74.9	103.31
35	0.295	12.23	27.36	80.3	107.66
40	0.338	11.37	26.22	87.4	113.62
45	0.426	10.49	25.58	93.8	119.38
50	0.532	9.70	24.16	100.1	124.26
55	0.661	9.33	23.23	115.1	138.33

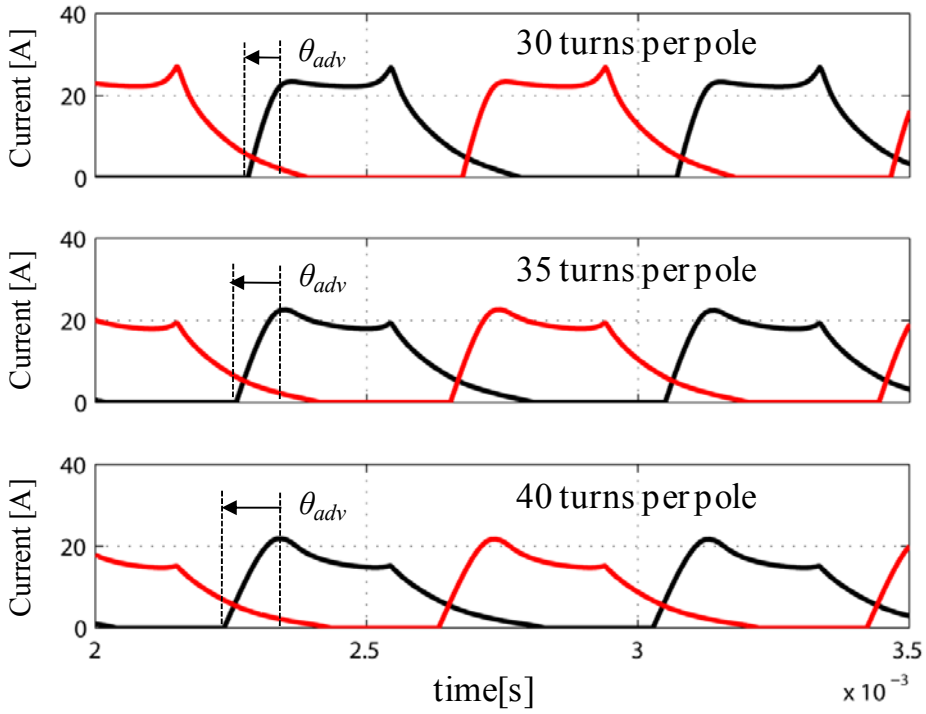

Fig. 5.17. Phase currents for different number of turns running at the same operating point (38,000 r/min, 0.3N-m)

On the other hand, a small number of turns allows phase current to build up quickly after turn-on and reduces the advance angle, thereby increasing efficiency. However, the rms current level to torque ratio is high resulting in a higher drive current rating and cost. As shown in Fig. 5.17, a lower number of turns correspond to a lower power loss and higher efficiency but higher rms current. From Table 5.1, 35 turns has been chosen for the prototype SRM drive considering the power converter VA rating and ac source constraints.

5.8 Simulation Verification

Based on the model derived in the previous sections, dynamic simulations are performed. The nonlinear machine characteristics are modeled from FEA results and non-ideal converter circuit model as well as control algorithms are implemented using Matlab. The simulation results are shown in Figs. 5.18, 5.19, and 5.20. Fig. 5.18 shows the waveforms of dc link capacitors, C1 and C2 that are charged during positive ac cycle (C1) and negative ac cycle (C2) respectively with approximately 20% voltage ripple. Note that each phase current is multiplied by five times of the original waveforms for clearer comparison. As observed from Fig. 5.18, the fluctuation in current waveform is due to the ripple of the dc link voltages that are applied to each phase, hence resulting in ripples in flux linkage and torque. Figs. 5.19 and 5.20 show the capability of the designed drive system capable of running at rated speed of 38,000r/min with full load power (1.2kW) and running at 48,000r/min with approximately 83% of full load power. Base on performance prediction through the dynamic simulation, the experimental results and its correlation with the simulation results will be discussed in the next section.

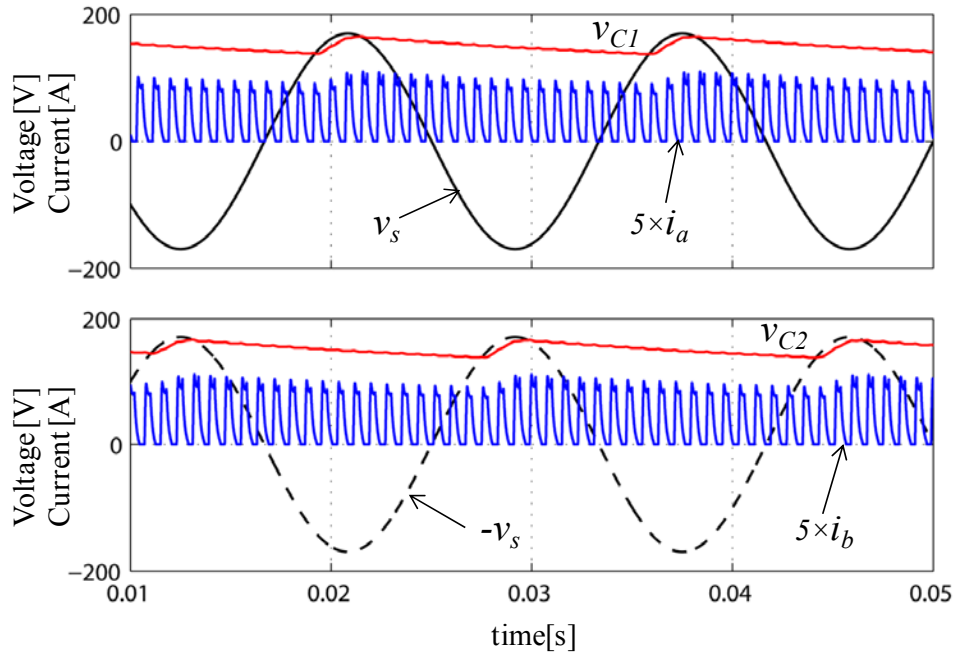

Fig. 5.18. AC input and dc link capacitor voltages along with the phase currents

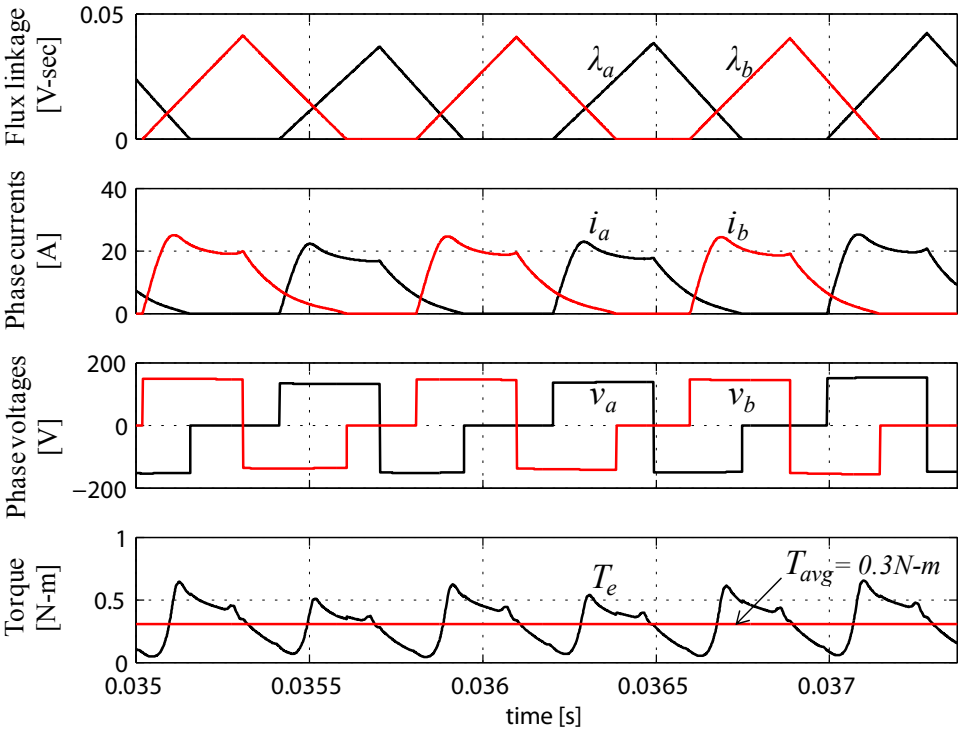

Fig. 5.19. Steady- state waveforms running at 38000r/min, 0.3N-m (1.2kW)

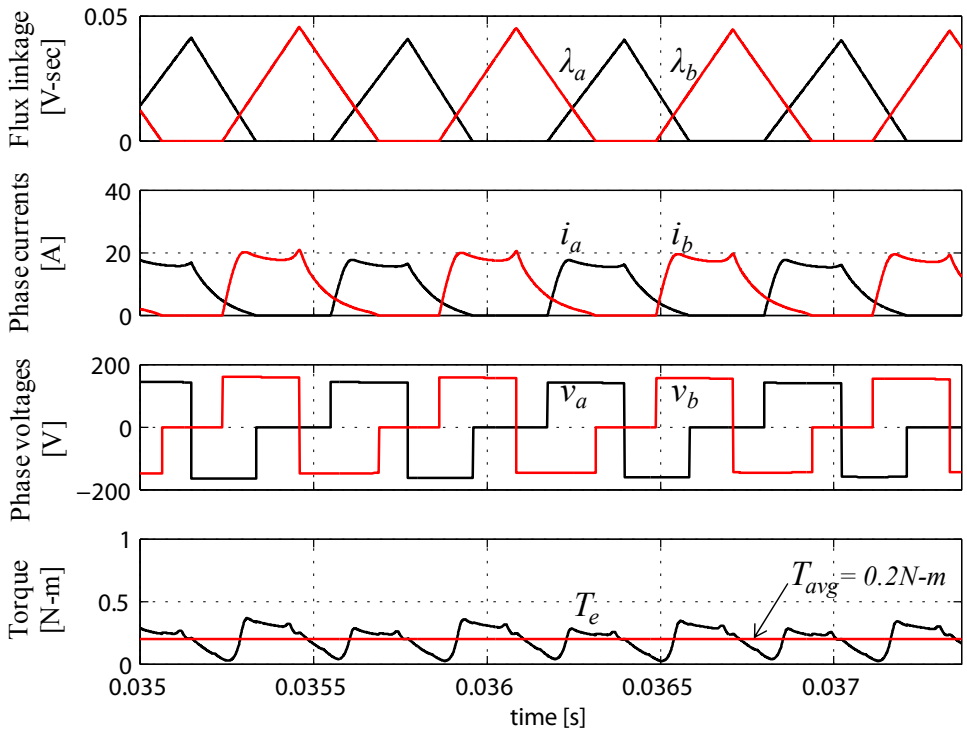

Fig. 5.20. Steady-state waveforms running at 48000 r/min, 0.20N-m (1kW)

5.9 Experimental Results

5.9.1 Construction of Prototype Drive System

Fig. 5.21 shows a prototype two-phase 4/2 SRM with phase windings mounted on the stator poles and a rotor mounted on an end bell. The specification of the prototype motor is listed in Table 5.2. Due high stroke (commutation) frequency at high speeds, the thickness of the iron steel lamination for both stator and rotor should be as thin as possible to minimize eddy current loss. In the prototype motor, a lamination with 26 gauge thickness was used.

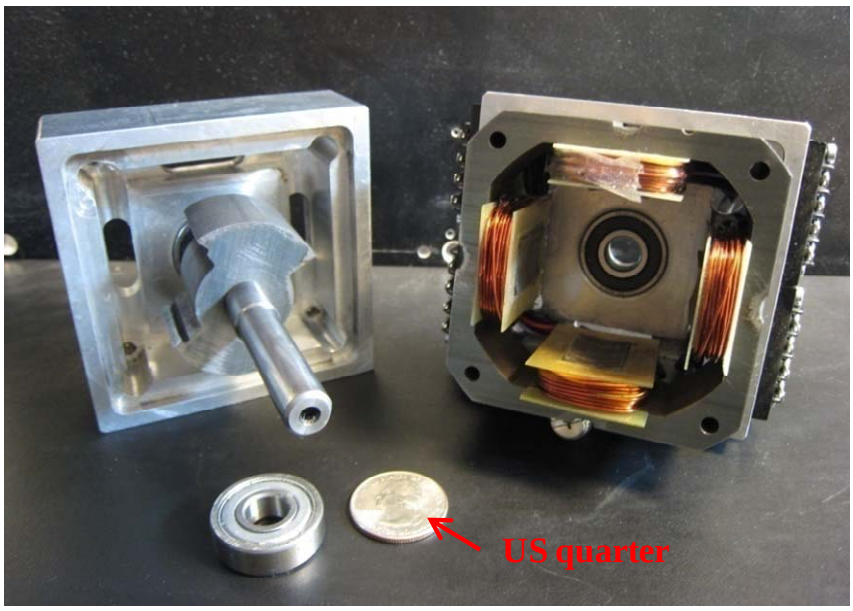

Fig. 5.21. Prototype two-phase 4/2 SRM

Table 5.2 Specification of the prototype two-phase 4/2 SRM

ITEM	VALUE
Rated output power	1.2kW
Rated/Max. speed	38,000/48,000rpm
Input ac line voltage	120Vrms
Stator outer dimension	76.4mm × 76.4mm
Number of pole(stator/rotor)	4/2
Lamination stack	25.4mm
Aligned phase inductance	4.3mH at 2A
Unaligned phase inductance	0.3mH at 2A

Fig. 5.22 shows the drive converter electronics. The on-board power supply and gate drive will sit vertically on the 3”x3” main converter board, making the overall converter electronics very compact. In the split ac supply converter, the dc link capacitors should be selected while considering the trade-off between capacitance, cost, and voltage ripple. The most severe voltage ripple occurs when the phase winding is fed by the discharging capacitor. As a

worst case, assuming 700W per phase output power with 20% voltage ripple, the minimum capacitance can be estimated using the following equations. V_{max} and V_{min} are the maximum and minimum capacitor voltage, and Δt is the maximum discharging time.

$$\Delta W = \frac{1}{2} C(V_{\max}^2 - V_{\min}^2) \tag{4.24}$$

$$C = \frac{2 \cdot P \cdot \Delta t}{V_{\max}^2 - V_{\min}^2} \approx 2000uF \tag{4.25}$$

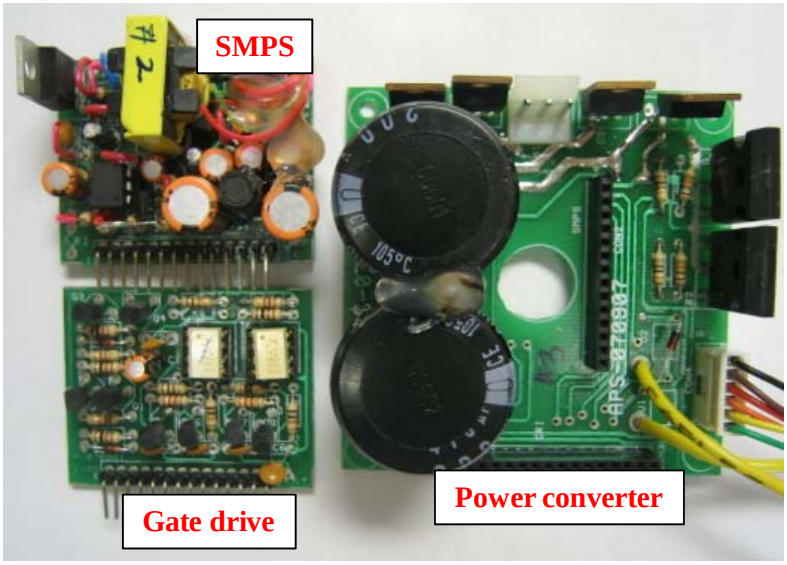

Fig. 5.22. Prototype power converter and drive electronics

5.9.2 Static Tests

To verify the prototyping quality and static performance of the motor, the inductance and torque profiles were measured and compared with the FEA simulation results using the setup shown in Fig. 5.23. Figs. 5.24 and 5.25 show the measured inductance and torque of the prototype machine and its correlation with FEA data. The static inductance and torque is measured every four degree at 6A and 8A excitation for a complete commutation cycle of 180 degree. The maximum error between FEA and measured inductance profiles is 7.2%, which may arise from the inaccurate B-H characteristics used in FEA simulations and manufacturing quality of the prototype. The maximum error between static FEA and measured torque profiles is 9.2%.

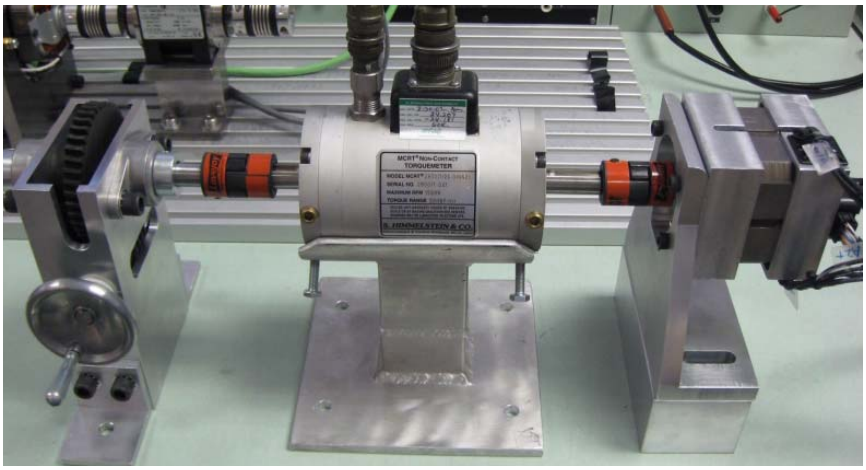

Fig. 5.23. Inductance and static torque measurement setup

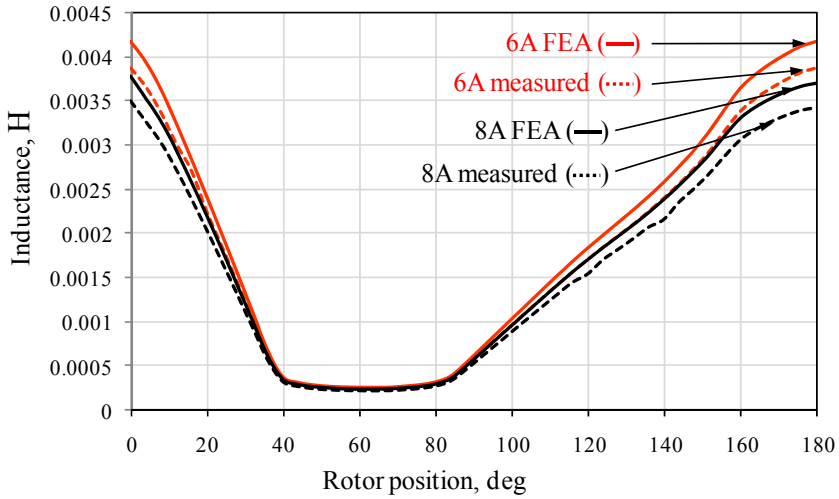

Fig. 5.24. Comparison between measured and FEA simulated inductance profiles

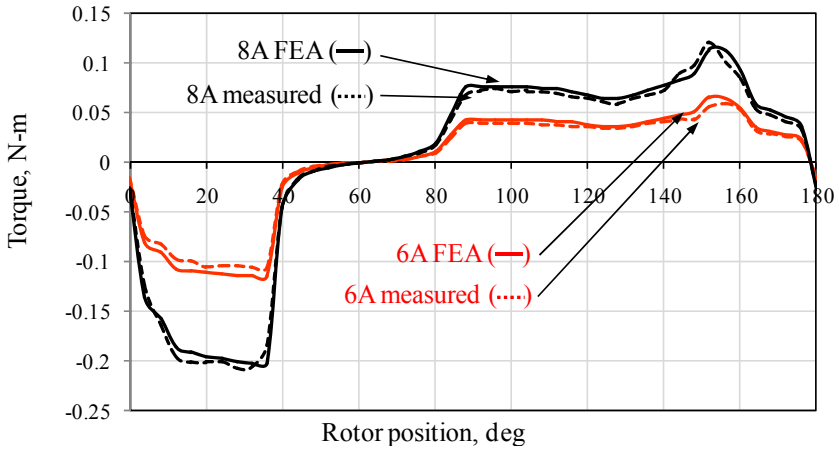

Fig. 5.25. Comparison between measured and FEA simulated torque profiles

5.9.3 Dynamic Tests

To verify dynamic performance of the prototype drive, experimental tests have been carried out using a dynamometer set-up as shown in Fig. 5.26. The mechanical speed, torque and output power are acquired by a high-speed torque transducer. Using this setup, the operation at different operating points was conducted. The test results for two operating points: 1) 38,000r/min with 0.3N-m load torque (1.2kW), 2) 48,000r/min with 0.2N-m load torque (1kW) are summarized in Table 5.3. Figs. 5.27 and 5.28 show the measured waveforms from running the SRM at 38,000 r/min and 48,000r/min with different loads, thereby demonstrating its high speed capability.

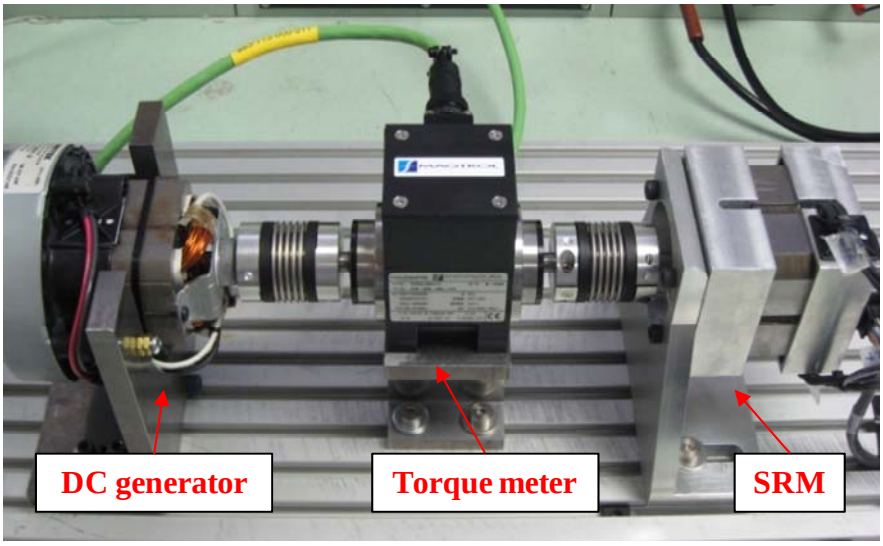

Fig. 5.26. Dynamometer setup for experiments

The measured converter, machine, and system efficiency at two different operating points and its correlation with simulation results is presented in Table 5.3 to validate the performance of the proposed drive system. To accurately estimate efficiency, copper and converter losses are calculated analytically [42] and core loss is estimated from FEA simulations. The measured power converter efficiency is approximately 97% which are comparable to the conventional asymmetric converter [42]. As for the machine and system efficiency, the error between the measured and estimated efficiency is 2.9 to 3.7%, which can be ascribed to unmodeled losses in the experimental system due to the quality of the prototype's manufacturing and assembly.

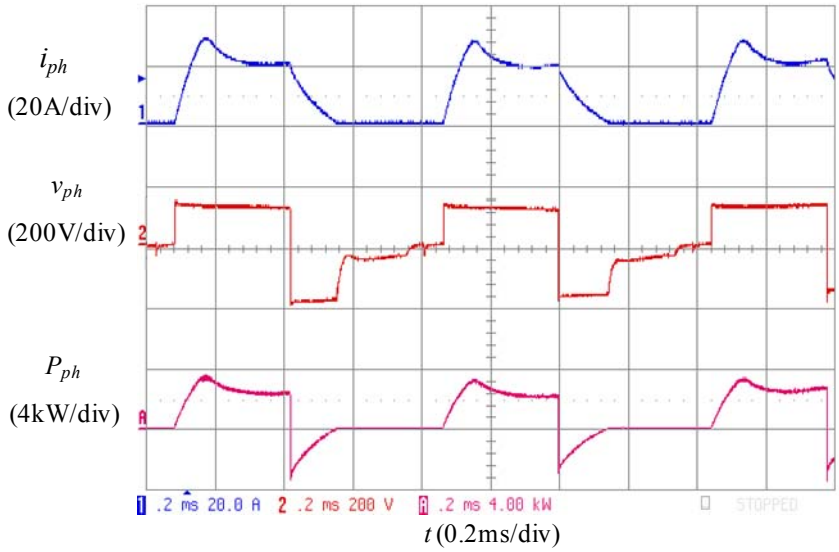

Fig. 5.27. Measured waveforms of phase current phase voltage, and phase input power operating for 38000 r/min, 0.3N-m (1.2kW)

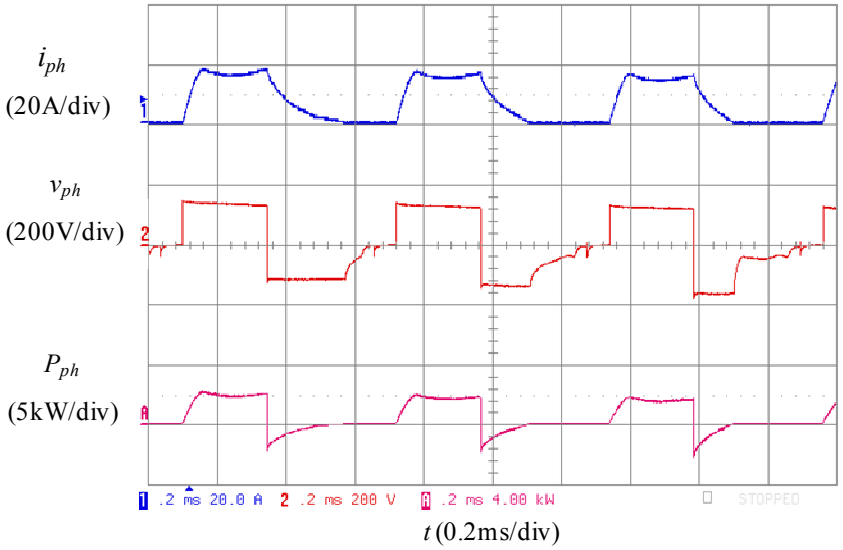

Fig. 5.28. Measured waveforms of phase current phase voltage, and phase input power operating for 48000 r/min, 0.2N-m (1kW)

Table 5.3 Specification of the prototype two-phase 4/2 SRM

Output [kW]	Converter [%]		Machine [%]		System [%]	
	Estimated	Measured	Estimated	Measured	Estimated	Measured
1.0	98.1	96.9	75.6	72.7	74.2	70.5
1.2	98.5	97.6	76.1	73.8	75.0	72.1

5.10 Summary

A low cost, high efficiency, high speed SRM drive system is presented in this paper. The drive system is realized with a two-phase SRM and a split ac converter. The drive system is designed for running at 38,000r/min (1.2kW) and maximum speed of 48,000r/min. The contributions of this paper are:

1) Modeling, design and analysis of a low cost high speed SRM drive system is presented and its performance has been validated via simulations and experiments.
2) The high speed capability of the proposed drive system was demonstrated experimentally.
3) Optimization of the turn on and turn off angles was performed to maximize system efficiency at the rated operating point. Switching angle vs. efficiency and torque in the single-pulse mode has been characterized to achieve the optimal operating efficiency.
4) Number of winding turns in the SRM was optimized by FEA and dynamic simulations in terms of efficiency and converter rating.
5) The presented drive system can be a strong candidate for high-speed low-cost applications where both cost and performance are valued.

Chapter 6

Position Sensorless Operation of SRM Drives

6.1 Introduction

The switched reluctance motor (SRM) produces torque through excitation of phase winding in synchronism with the rotor position. Therefore, the SRM requires rotor position information for proper control, which is achieved pervasively by position sensors mechanically mounted on the rotor shaft. These sensors, however, require mounting labor and space, and hence add to cost and packaging size of the drive system, which is not desired by manufacturers. In addition, some applications are reluctant to accept the sensor because of reliability, environmental constraints, etc. Therefore, extensive research has been carried out for decades to find methods for rotor position and/or speed estimation without resorting to those sensors. Various methods for position sensorless estimation and control have been proposed hitherto; however, it is difficult to find one particular method suitable for all types of applications since their selection primarily depends on specific application and operating speed.

A new, simple method for position sensorless control for SRMs is proposed and described in this chapter. Basic concept underlying this scheme is use of linearized relationship between the rotor position, inductance, and the rate of change of current. Two consecutive switch-on times of the controllable switch in hysteresis current control are compared to estimate

the rotor position and speed. Using this method, the unaligned and aligned positions which can be used as default turn-on and turn-off angles is determined.

The proposed method is very simple to implement in that it does not require complex computation or lookup table and thereby suitable for low cost applications. The method is robust in it is not dependent on the motor parameter variation.

6.2 State-of-the-art-review

Most position sensorless techniques utilize the fundamental principle the SRM's magnetic characteristic, i.e. the unique relationship between the flux linkage (or inductance), rotor position, and excitation current. Therefore, a key to the successful realization of a sensorless SRM drive is a reliable flux linkage or inductance estimate during operation.

The flux-current methods in [44], [45] estimate flux linkage by open-loop integration with measured terminal signals (voltage and current) and then extracts rotor position from the stored three-dimensional data between flux, current, and rotor position. While this approach is simple and more suitable for high speed, single-pulse operation, it needs a large amount of lookup tables and can have significant estimation errors at low speed, chopping mode operation where the effect of the winding resistance becomes significant. Flux or inductance variation can be obtained directly using sensing coils [46], [47], but the extra coils may cause coupling with main power signals and add to the manufacturing cost and effort. However, the extra coils may cause coupling with main power signals and add to the manufacturing cost and effort.

Observer-based methods [48]-[50] utilize model-based estimators to estimate state variables such as flux, speed, or rotor position by real-time computation with measured phase voltage and currents. Although these methods are valid over wide speed range, substantial real-time computation and high sensitivity to parameter variation are their major drawbacks.

Intelligent control methods such as neural networks and fuzzy logics in [51]-[53] provides an inherent capability to identification which is capable of adaptation of parameter change in contrast to static memory. However, such an approach requires off-line training and

depends on the designers' experience. An approach to decrease the computation effort significantly is proposed in [54].

Inductance based methods [55]-[59] exploit the relationship between the phase self-inductance (or incremental inductance) and rotor position for each excitation current. Phase inductance is obtained from analytical model using terminal measurement of phase currents and then the relationship between the rotor position and the self-inductance is derived using finite element analysis (FEA) results or off-line measurement. The phase inductance variation can be alternatively estimated by injecting a high frequency diagnostic signal into the inactive phase [22]-[23] but inter-phase coupling, switching noise interference, eddy current losses are the major drawbacks of this method.

Sensorless control proposed in [60]-[61] employed the fact that under certain assumptions the current rise and fall times within the switching cycle are proportional to the incremental inductance from which the rotor position can be extracted.. The incremental inductance is calculated using the voltage equation with measured current increment and rise or fall time and then obtain rotor position from the stored the incremental inductance data. The major drawback of this method is that the imprecise computation of back-EMF and uncertain winding resistance deteriorates the estimation accuracy. In addition, the incremental inductance is bi-valued even within half a rotor pole pitch at current equal to or greater than 50% of the rated current [56].

6.3 Proposed Sensorless Control Algorithm

The fundamental idea of the proposed sensorless control is that the rate of change of current depends on the phase self-inductance, which in turn depends on the rotor position. In this regard, it is similar to incremental inductance based method [59],[60]. However, the proposed method does not require magnetization data on-line calculation of the inductance and mapping of inductance–position relationship and hence no off-line measurement or lookup table is necessary. Instead, by comparing two consecutive switching times in the hysteresis current control mode, the proper commutation of the motor as well as the speed estimation can be achieved. The advantages of the proposed methods are summarized as follows.

- No a priori knowledge of inductance profile is required
- No pre-stored data of magnetic curve or inductance is needed.
- It is simple to implement.
- It is applicable to any conventional SRM.
- No extra hardware is required.
- Insensitive to system parameter variations

6.3.1 Principle of Estimation

The basic principle of the proposed sensorless control is illustrated in Fig. 6.1. In an unsaturated magnetization case, the voltage equation for the main phase winding can be approximated from (6.1) as

$$v_a = R_a i_a + L_a(\theta)\frac{di_a}{dt} + i_a \frac{dL_a(\theta)}{dt} \tag{6.1}$$

where L_a is the angle dependent main phase self inductance.

Assuming the motor is running at a constant speed, voltage equations at two sampling times for any two consecutive switch-on periods can be expressed respectively by

$$v_a(t_1) = R_a i_a(t_1) + L_a(t_1)\frac{di_a(t_1)}{dt} + i_a(t_1)\frac{dL_a(t_1)}{dt} \tag{6.2}$$

$$v_a(t_2) = R_a i_a(t_2) + L_a(t_2)\frac{di_a(t_2)}{dt} + i_a(t_2)\frac{dL_a(t_2)}{dt} \tag{6.3}$$

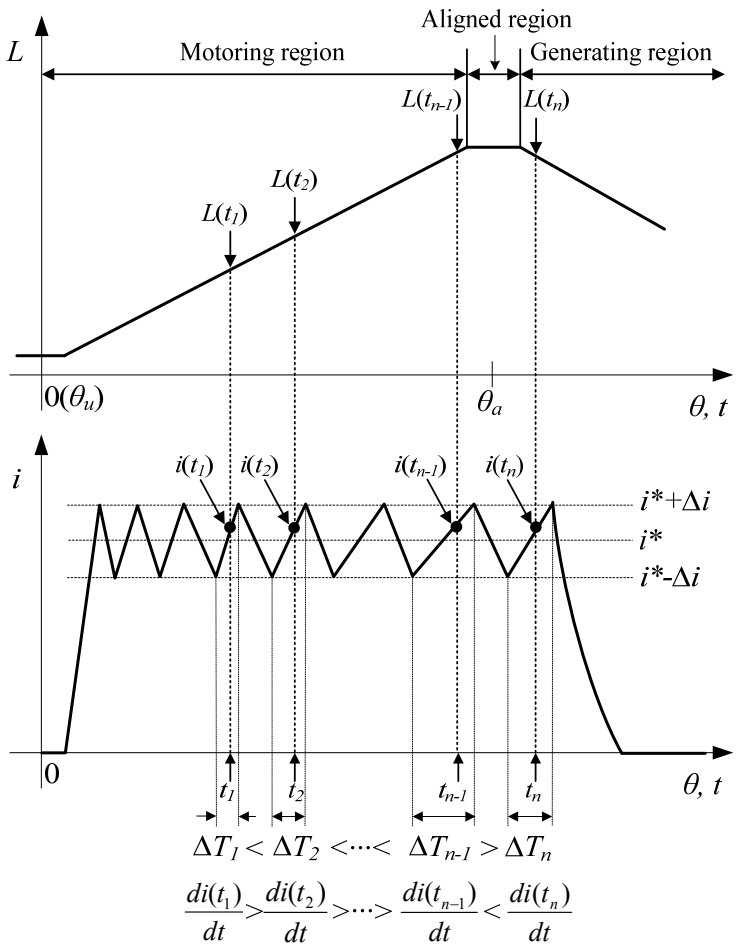

Fig. 6.1. Relationship between inductance and rate of change of current.

The voltage applied to main winding for each case is the dc bus voltage, i.e. $v_a(t_1) = v_a(t_2) = V_{dc}$. Assuming good current regulation (hysteresis control employed herein), each instantaneous current at t_1 and t_2 is comparable to the reference value, i.e. $i_a(t_1) \approx i_a(t_2) \approx i$, which yields

$$R_a i_a(t_1) \approx R_a i_a(t_2) \tag{6.4}$$

Assuming a non-saturated linear inductance case, the slope of the main phase inductance profile, $dL_a(\theta)/dt$ is constant in the motoring region. Therefore, the third terms of both (6.2) and (6.3) can be assumed to be the same:

$$i_a(t_1)\frac{dL_a(t_1)}{dt} \approx i_a(t_2)\frac{dL_a(t_2)}{dt} \tag{6.5}$$

Considering (6.4) and (6.5), subtracting (6.3) from (6.2) ends up with

$$L_a(t_1)\frac{di_a(t_1)}{dt} \approx L_a(t_2)\frac{di_a(t_2)}{dt} \tag{6.6}$$

From (6.6), following relationship between the rate of change of current and the phase inductance can be inferred:

1) Motoring region ($dL_a/dt > 0$)

$$\text{if } \frac{di_a(t_2)}{dt} < \frac{di_a(t_1)}{dt}, \text{then } L_a(t_2) > L_a(t_1) \tag{6.7}$$

: *di_a/dt decreases as L_a increases.*

2) Generating region ($dL_a/dt < 0$)

$$\text{if } \frac{di_a(t_2)}{dt} > \frac{di_a(t_1)}{dt}, \text{then } L_a(t_2) < L_a(t_1) \tag{6.8}$$

: *di_a/dt increases as L_a increases.*

3) Aligned and unaligned regions ($dL_a/dt = 0$)

$$\text{if } \frac{di_a(t_2)}{dt} = \frac{di_a(t_1)}{dt}, \text{then } L_a(t_2) = L_a(t_1) \tag{6.9}$$

: *di_a/dt does not change since L_a remains constant.*

The rate of change of current for each switch-on time can be calculated by measuring switch-on time (ΔT_{on}) and the current increment ($2\Delta i$) within a switch-on period as shown in Fig.6.1:

$$\frac{di_a}{dt} = \frac{2\Delta i}{\Delta T_{on}} \tag{6.10}$$

Since Δi is known from the predefined hysteresis current band which is constant for all switching cycles, (6.7), (6.8), and (6.9) can be rewritten as

$$\text{if } \Delta T_1 > \Delta T_2, \text{then } L_a(t_2) > L_a(t_1) \tag{6.11}$$

$$\text{if } \Delta T_1 < \Delta T_2, \text{then } L_a(t_2) < L_a(t_1) \tag{6.12}$$

$$\text{if } \Delta T_2 = \Delta T_1, \text{then } L_a(t_2) = L_a(t_1) \tag{6.13}$$

Therefore, by comparing switch-on times for two consecutive PWM cycles, the aligned (θ_a) and unaligned (θ_u) positions can be detected. If $\Delta T_n > \Delta T_{n-1}$ for any two consecutive switching cycles, the rotor is still in the motoring region (positive inductance slope) and hence the main phase should remain energized. If $\Delta T_n \le \Delta T_{n-1}$, then the rotor has reached the aligned position where commutation of the main phase should be established. Once the aligned position is detected, the unaligned position can be easily determined from the motor geometry shown in chapter 3 such that they are shifted by 45° each other. At low speed, the detected aligned position can be used as default turn-off (θ_{off}) angle, and turn-on (θ_{on}) angle can be adjusted to control dwell period with respect to operating speed and load. Fast sampling in hysteresis control is of importance so that the commutation should be initiated before the rotor enters the generating region significantly.

At high speed, however, turn-off angle needs to be advanced to avoid significant negative torque generation. In this case, the aligned position is first detected by monitoring transition of switch-on time vs. inductance relationship from (6.13) to (6.11), and then the proper turn-off angle can be adjusted based on the operating speed. Among the important advantages of the proposed sensorless method are: 1) Simple digital implementation without substantial computation or extra hardware is possible., 2) No pre-stored data for inductance profile or magnetization curves is required, 3) The voltage equation is not used for position estimation, and hence the accuracy of the estimation is not significantly affected by the effects of winding resistance and back-EMF.

6.3.2 Digital Real-time Implementation

A DSP controller has been used to implement the proposed sensorless algorithm as illustrated in Fig. 6.2 showing the waveforms of gate signal, main phase current, and timer counts. Two timers have been used to calculate the switch-on time and the motor speed and position.

***1) Timer 1* (*switch-on time calculation*):** Timer 1 is a CPU timer to calculate switch-on time. This timer counts by 10MHz clock frequency; hence, the switch-on time at each different switching cycle is calculated using

$$\Delta T_{on}(n) = TC(n) \times (0.1\mu s) \tag{6.14}$$

where $TC(n)$ is the total timer count for switch-on time at each different switching cycle. In hysteresis current control, when the main phase current falls below the lower hysteresis band limit, the switch is turned on. As soon as the switch is turned on, Timer 1 starts counting until the switch is turned off when the phase current reaches the upper hysteresis band limit. Total count value of Timer 1 for switch-on time is stored in the register and then Timer 1 is reset to zero for the next switching cycle. The timer begins to count again when the current reaches the lower hysteresis band limit and hence the switch is turned on. As shown in Fig. 6.2, the timer count value at each switching cycle, $TC(n)$ is compared with the one at the previous switching cycle, $TC(n–1)$ except for the first switch-on time during the initial current buildup. As soon as the controller detects the instant when $TC(n) – TC(n–1) \leq 0$, the excitation of the main phase is terminated (Excite = 0).

***2) Timer 2* (*Speed and position estimation*):** Timer 2 measures time interval between two consecutive aligned (45°) positions−i.e. 90° angular interval of rotor pole pitch−by counting PWM interrupt routine that occurs every 4μs (250kHz). The measured time interval is used to calculate the speed and position of the rotor. As shown in Fig. 6.2, Timer 2 starts incrementing when the rotor is on the aligned position (Excite = 0) until it reaches its maximum count at the next aligned position. Then, this timer resets to zero and starts counting again. The speed is calculated every time the aligned position is detected:

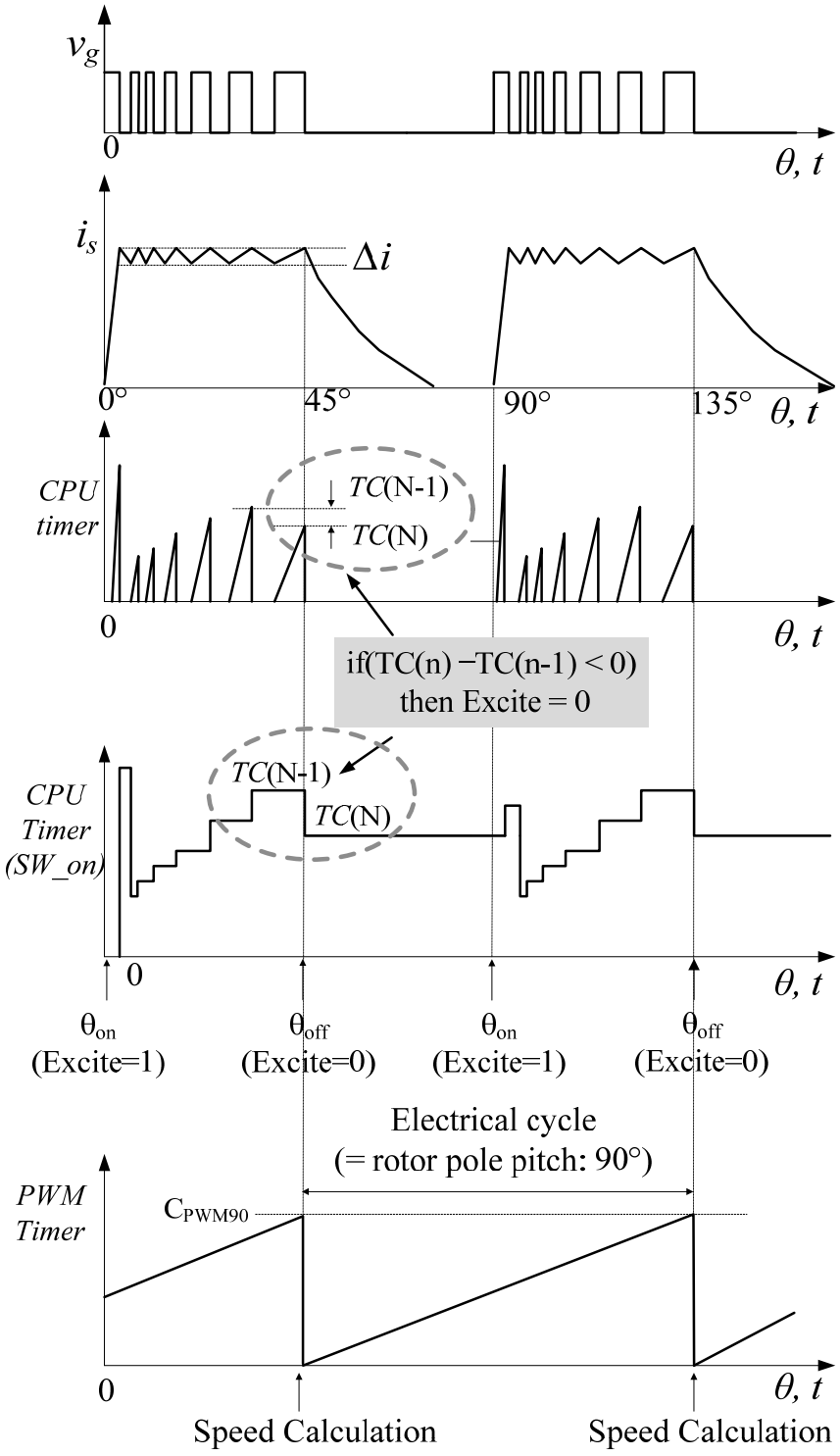

Fig. 6.2. Position estimation and sensorless control algorithm

$$\omega_r = \frac{d\theta}{dt} = \frac{90°}{TC\_90 \times 4\mu s}(\text{deg}/s) = \frac{90°}{TC\_90 \times 4\mu s} \times \frac{60}{360°}(r/\text{min}) \tag{6.15}$$

where TC_90 is total count value of Timer 2 for the interval between the two aligned positions (90° rotor pole pitch). Assuming the speed is constant at steady-state, the rotor position, θ within the phase commutation cycle (0° to 89°) can be calculated by

$$\theta = \text{rem}\left(\frac{Timer2\_Count}{TC\_90} \times 90° + 45°, 90°\right)(\text{deg}) \tag{6.16}$$

where Timer2_Count is an incremental count value of Timer 2 and the value of TC_90 is inherited from the previous speed calculation.

6.4 Sensorless Drive System Control

6.4.1 Sensorless Starting

At standstill, when S1 is turned on for a preset period of time to induce a large current pulse in the main phase winding. This current, along with the current through the auxiliary phase winding when S1 is turned off, results in torque production and causes the rotor to move. Note that the number and period of the applied starting pulses are predetermined based on required starting torque. Once the motor starts, the controller executes the sensorless control algorithm. First, the main winding is excited regardless of the rotor position to find the aligned position, and after the aligned position is determined, the controller executes normal commutation of each phase by calculating the rotor position and speed. After the sensorless control algorithm is put into execution, and the motor is driven to the desired speed.

6.4.2 Hysteresis Current Control

For inner-loop current control, hysteresis current control has been employed. Among the main advantages of hysteresis current control are simplicity, fast response, and robustness to

system parameter perturbation. The dynamic performance is limited only by switching speed and load time constant, which makes hysteresis current control suitable for parameter insensitive sensorless control. However, unknown switching frequency may lead to increased acoustic noise. For digital implementation, fast sampling is necessary in order to minimize the response delay and tracking error and hence to achieve performance comparable to analog implementation. In the considered experimental setup, 250 kHz sampling frequency is utilized.

6.4.3 Main Control Algorithm

The proposed sensorless control has been implemented in a 32-bit 100MHz fixed-point digital processor (DSP) controller and its software implementation is illustrated using flowcharts in Figs. 6.3, 6.4 and 6.5. Fig. 6.3 shows a flowchart for the main function of the drive control algorithm. After initialization of DSP, starting and sensorless control are put into execution in sequence. The sensorless control algorithm is executed every PWM interrupt routine as shown in Fig. 6.4. The PWM routine starts off monitoring the rotor position to determine whether to initiate the excitation of the main winding, followed by the current control loop. Timer 2 counts every time this routine is executed.

The current control loop shown in Fig. 6.5 executes hysteresis control, switch-on time calculation, and speed calculation. When the main winding current goes below the lower hysteresis limit ($i^*-\Delta i$), the switch is turned on. Timer 1 is reset and starts incrementing. When the main winding current exceeds the upper hysteresis limit ($i^*+\Delta i$), the switch is turned off and the final count of Timer 1 is stored and compared with the previously stored timer count value for the previous switching cycle. Keep on comparing until $TC(n)-TC(n-1) \leq 0$. The rotor is now in the aligned position, where phase excitation should be extinguished immediately (Excite = 0). Then, the rotor speed is calculated from Timer 2's value and then Timer 2 is reset to zero.

Although it is theoretically true that $T(n) > T(n-1)$ at any two consecutive positions within the motoring region, it may not be the case in practice due to unfiltered noise, discretization error, or choppy nature of instantaneous inductance profile resulting from current control. Thus, it is necessary to ensure the correct excitation period to avoid unwanted early termination of excitation. Instead of comparing only two discrete switch-on times, T(n) and T(n-

1), comparing two averaged switch-on times can solve this problem. First, take two moving averages of several (five cycles were used here) switch-on times: 1) average from T(n) to T(n-4) and 2) average from T(n-1) to T(n-5), and then compare two averaged switch-on times.

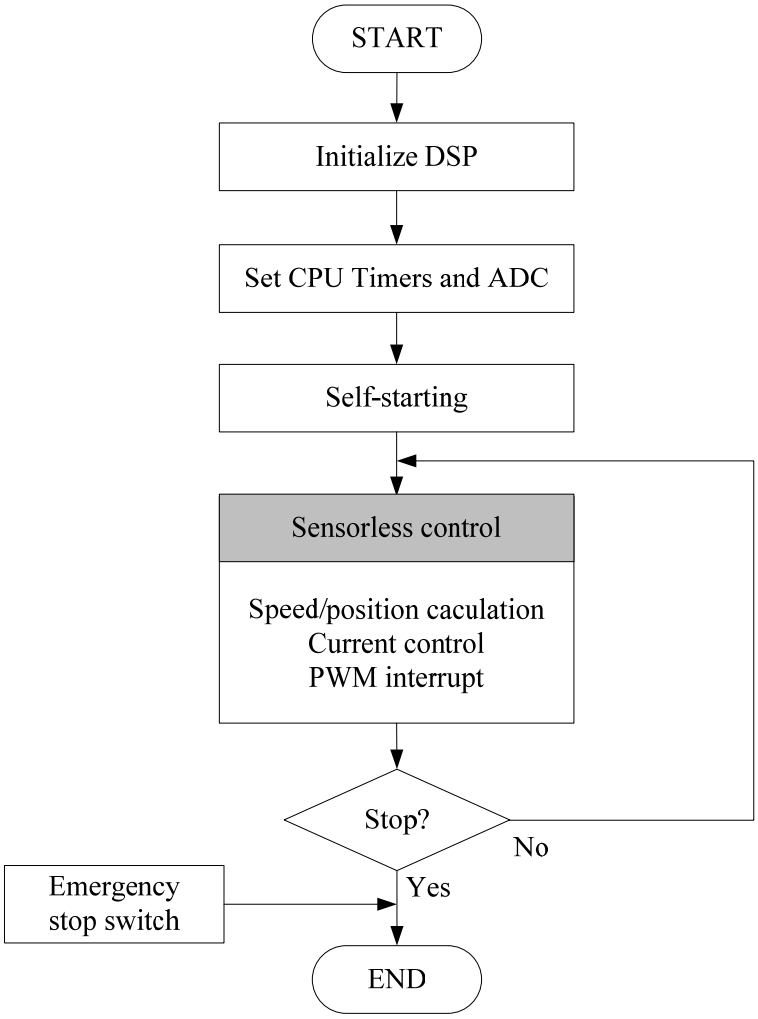

Fig. 6.3. Flowcharts for the main function algorithm

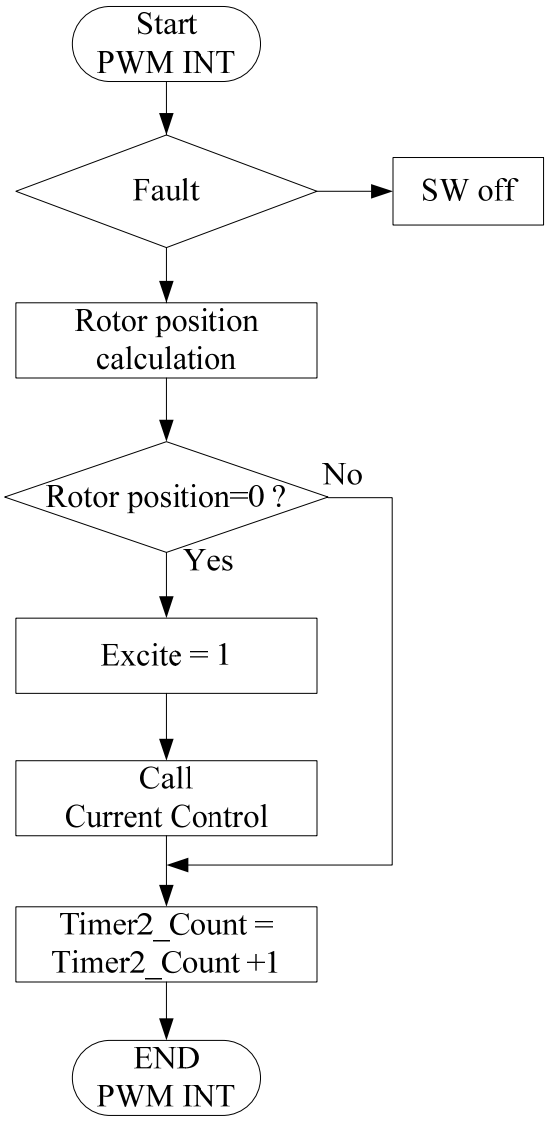

Fig. 6.4. Flowcharts for the PWM interrupt routine

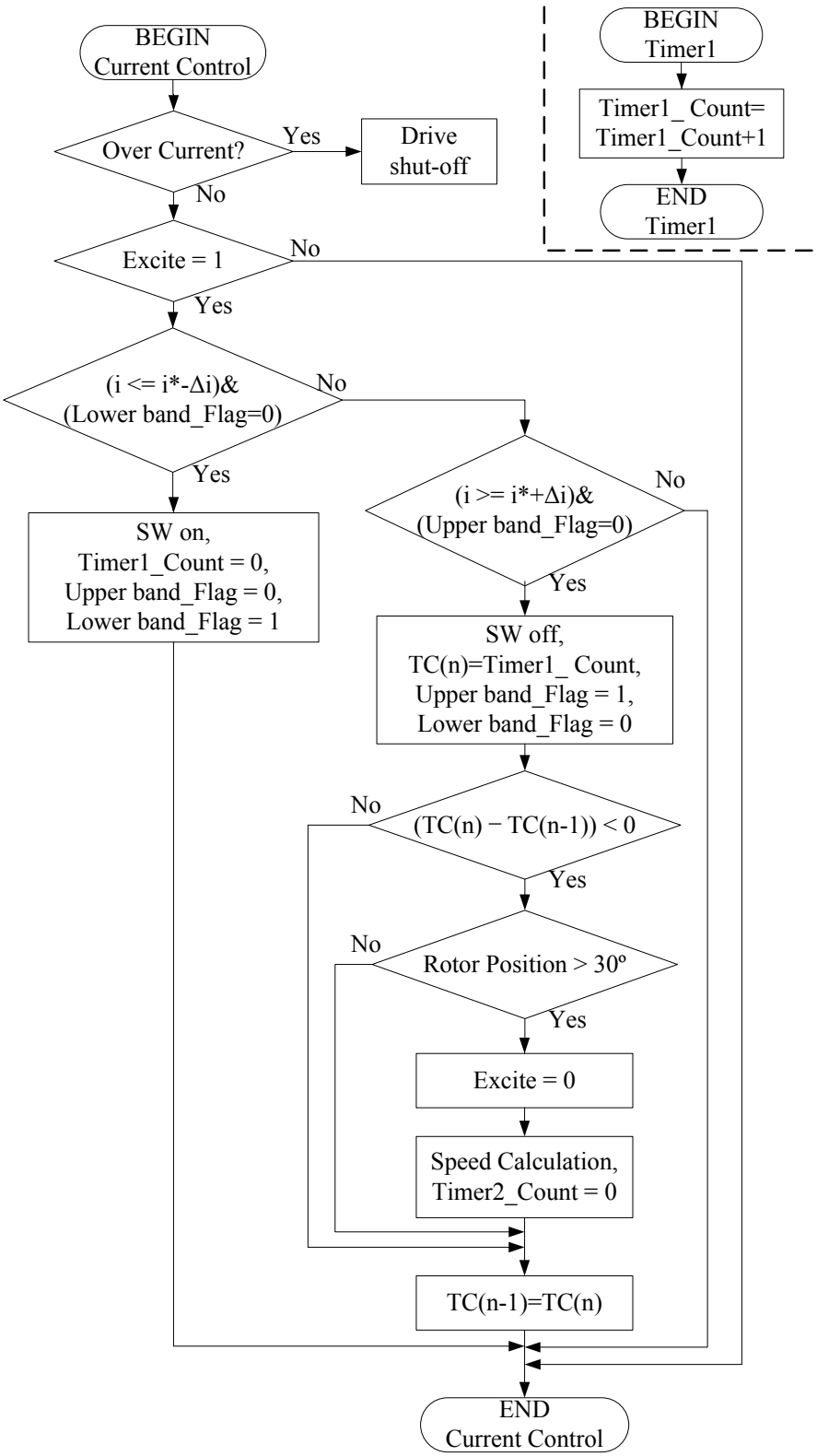

Fig. 6.5. Flowchart for current control loop

6.4.4 Firing Angle Control

In addition to controlling the amplitude of the phase current, correct placement of phase current stroke is also crucial to achieve optimal performance of the drive system at different operating speeds and loads. In sensorless operation, position estimation error due to load disturbance or measurement noises can result in loss of synchronism of the estimated position with the actual position. Although an error less than a few degrees may not be critical specifically in target low cost applications, significant out-of-synchronism due to accumulated errors may result in unacceptable deterioration of drive performance. Therefore, it is important to ensure the estimated position synchronized with the actual position. Key to ensure the synchronism is to find at least one absolute position within a stroke cycle, which can serve as an index position.

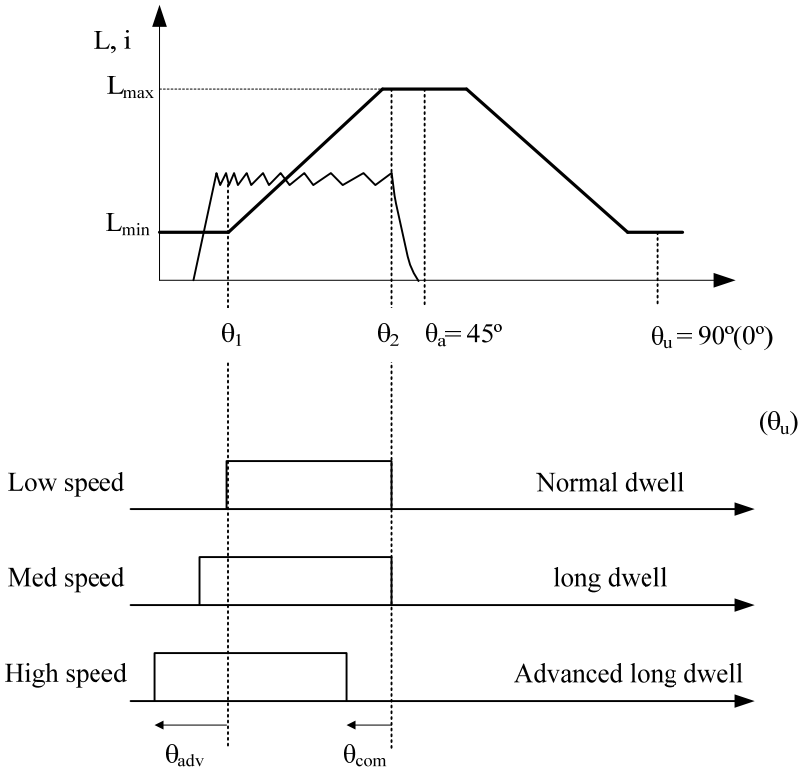

Fig. 6.6. Angle control strategy at different operation speeds

There are two index positions within a stroke cycle as shown in Fig. 6.6:

1) Rotor position where the inductance starts increasing (The rotor pole starts overlapping with the stator pole): θ_1
2) Rotor position where the inductance becomes constant at its maximum value (The rotor pole becomes completely overlapped with the stator pole): θ_2

Fig. 6.6 depicts the firing angle control scheme employed in this drive system. Idealized current pulses correspond to optimal excitation at different speed ranges. Angle control is carried out so that optimal current excitation at each different operating speed as well as smooth transition from low- to high-speed operation is achieved, and it is explained as follows.

Low speed

In low speeds, θ_2 where the inductance reaches the maximum value is used as an index position. This angle can be used as a default turn-off angle, θ_{off}. Turn-on angle can be determined using the motor geometry such that the unaligned position, θ_u (mid-point at maximum inductance region) and aligned position, θ_a (mid-point at minimum inductance region) are shifted 45° each other. The turn-on angle is determined by a position advanced by 45° from θ_2, which is slightly advanced than θ_1. No further advancing of either turn-on or turn-off is executed in this speed range so that dwell angle remains constant as the amplitude of current command is the main control parameter in low speeds.

Medium speed

As the speed increases, the current cannot rise fast enough to reach its commanded value at the onset of positive inductance slope, i.e., θ_1 due to the effect of back-EMF and finite rise time. The excitation must be initiated earlier than θ_1 and hence the turn-on angle should be advanced with respect to the operating speed. The index position is still θ_2 in this speed range and θ_2 is used as a turn-off angle which still remains the same.

High speed

As the speed even further increases, the back-EMF becomes comparable to dc link voltage, hence requiring further advancing the turn-on. In addition, the turn-off angle also needs

to be advanced to avoid negative torque production. Therefore, the index angle, θ_2 cannot be used as the constant turn-off angle as it is adjusted in this speed range. θ_1 is then used as an index angle. From detected θ_1, both turn-on and turn-off angles for the next cycle can be determined.

6.5 Simulation Verification

Fig. 6.7 shows simulation results for the proposed sensorless method implemented on the single-switch-based SRM running at 1800 r/min with 4A current command. Waveforms of the main phase inductance, gate signal for switch S1, main phase current, timer count for switch-on time, and estimated rotor position (electrical degree) are plotted. The timer count for each switch-on time varies with respect to the rotor position such that it increases along with the positive inductance slope but decreases with the negative inductance slope. Hence, the aligned position is detected from the transition of the timer count from incrementing to decrementing count. It can be seen that the timer count correlates with the actual inductance profile and hence with the estimated rotor position.

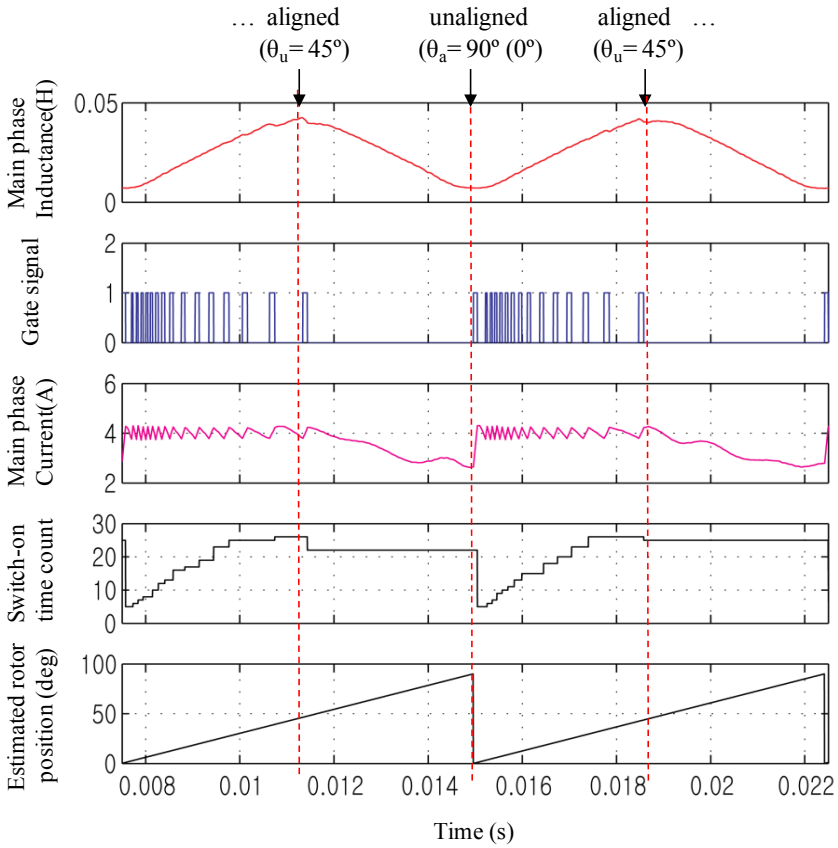

Fig. 6.7. Simulation results for the rotor position estimation

6.6 Experimental Results

Fig. 6.8 shows a block diagram of the experimental drive system including the motor, drive electronics, and controller. Drive control and sensorless algorithm is implemented in real-time using a TMS320F2808 DSP controller with 250 kHz sampling frequency for the main phase current. The dc link voltage is approximately 155V from the rectified ac main. The power switching devices for the converter are realized with an ultra-fast IGBT and fast-recovery diodes.

The execution of the sensorless starting is shown in Fig. 6.9. The large spike in the main phase current indicates the induced current pulse by the applied starting pulse with a preset period of time (1.2ms), which causes the rotor to rotate. The sensorless algorithm is invoked after 165ms to detect the aligned position. The starting may be challenging when the rotor is initially either at aligned position or midpoint between aligned and unaligned positions. In that case, multiple pulses should be applied to ensure the sufficient torque production in both main and auxiliary windings.

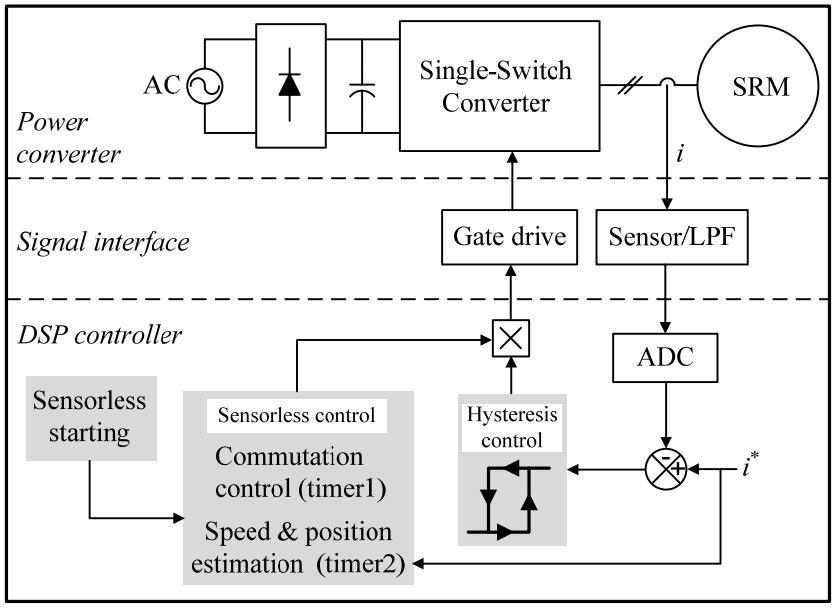

Fig. 6.8. Block diagram for experimental drive system

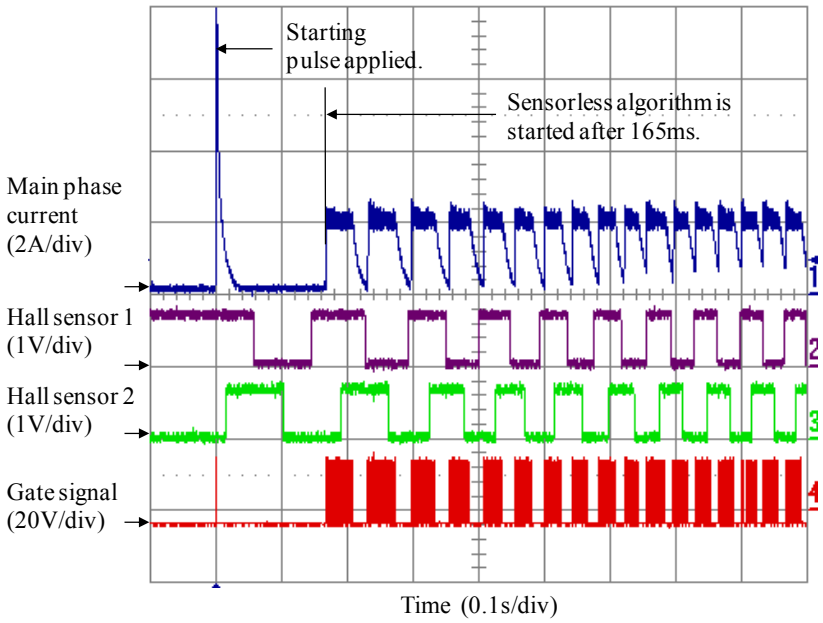

Fig. 6.9. Sensorless motor starting from standstill

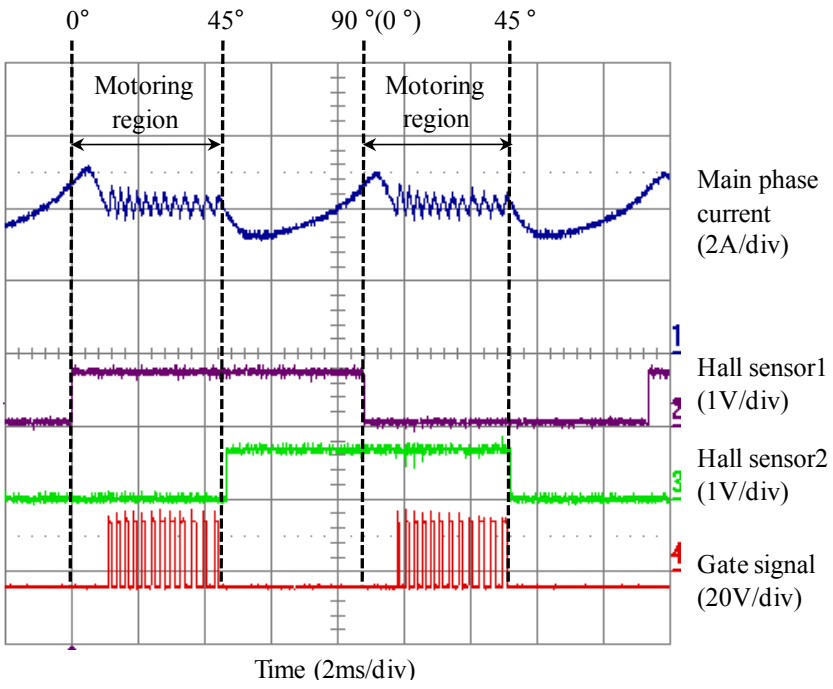

Fig. 6.10. Measured waveforms when the motor is running at 1800r/min

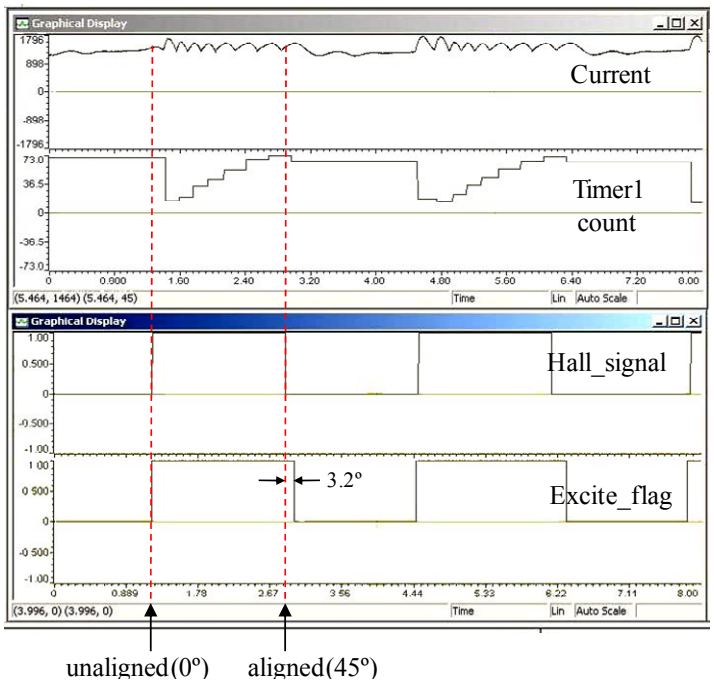

Fig. 6.11. Captured waveforms from DSP in real-time mode

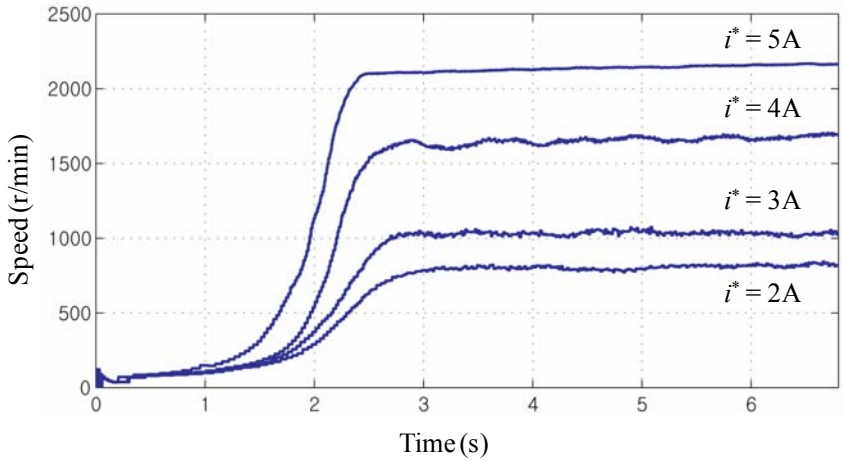

Fig. 6.12. Measured motor speed from startup to steady-state at different operating speeds

Experimental results for sensorless operation at steady-state are shown both in Fig. 6.10 and Fig. 6.11. Fig. 6.10 shows the winding current, two hall sensor signals, and gate signal. In the experimental motor, two hall sensors are mounted above two adjacent stator poles which are

45° shifted each other. Both rising and falling edges of the hall sensor 1 signal indicate the unaligned position (0°), and both rising and falling edges of the hall sensor 2 signal indicate the aligned position (45°). Note that only the estimated rotor position and speed are used for drive control, while the measured hall sensor signals are only a reference to indicate the correct motoring position. From Fig. 6.10, it can be seen that phase excitation is correctly achieved in the motoring region and the estimated aligned and unaligned positions are quite comparable to the actual ones detected by the hall sensors. The current spike at the beginning of excitation around the unaligned position is due to regenerative energy from the auxiliary winding.

Fig. 6.11 shows the waveforms captured by DSP in real-time mode, which correlates well with the simulation results in Fig. 6.7. While Hall_signal is logic sum of the hall sensor 1 and 2, representing the actual excitation period, Excite_flag is the flag signal for the sensorless algorithm, representing estimated excitation period. They both represent start of phase excitation at rising edge and end of excitation at falling edge. It can be seen that estimation of the unaligned position is quite accurate but there is a slight error at the aligned position, which is represented by the difference between the falling edges of the hall sensor signal and the excitation period flag about 3.2°. This is due to the inherent delay of phase commutation since the phase commutation is initiated after the unaligned position is detected. Another experiment result in Fig. 6.12 was performed to show the dynamic performance of the sensorless controller at different operating speeds with different loading, starting from standstill.

6.7 Summary

A new parameter insensitive sensorless control is proposed and experimentally demonstrated using the single-controllable-switch-based SRM drive. The key conclusions of this paper are:

1) The proposed scheme is very simple to implement requiring measurement of only phase current and minimal computation, and does not need any pre-stored lookup table or extra hardware, which makes this scheme inherently suitable for low cost deployment

2) The method is robust to the presence of system parameter variations since it does not employ an analytical inductance model or a model-based estimator which is sensitive to the estimation of the motor parameters.
3) Although the method is implemented using a two-phase SRM with the single switch converter, it can also be implemented with any multi-phase SRM with the conventional asymmetric converter.It does not limit low speed operation which is quite challenging in many flux or back-EMF based methods.
4) It is inherently suitable for current controlled operation rather than single-pulse operation where chopping is not possible.
5) The drive system has only one controllable switch and two diodes in total for driving the two-phase SRM, hence making it very compact and inexpensive. The considered SRM drive in conjunction with the proposed sensorless scheme can offer an attractive solution for brushless variable speed drives in low-cost, high-volume applications such as home appliances.

Chapter 7

Conclusions

This thesis has presented three different SRM drives that can be viable alternatives for conventional universal motors or permanent magnet DC brushes motors in high volume applications such as fans, pumps, home appliance drives. Two novel converters have been proposed. The drive systems are realized using two-phase motors and the proposed converters. The operation principles, derivation of system equations, converter modeling, as well as design consideration for all three different converter-based drives have been discussed. Simulation and experimental tests have also been conducted to validate feasibility of the drive systems. All of those drives have been validated based on conventional sensor-based speed control scheme. To achieve further cost reduction, a new parameter insensitive sensorless control has been proposed and partly implemented with the proposed drives. In addition, optimal efficiency control in single-pulse mode with optimal number of winding turns has also been presented to obtain optimal performance. The scope of this research is to develop low-cost, high-efficiency, brushless variable speed drives system targeting low-cost, high-volume application, such as home appliances markets. Three different two-phase SRM drives are designed and implemented with a focus on minimum electronics and simple yet efficient drive control to meet the demanding requirement from home appliance market in terms of cost, efficiency, input power factor.

The followings are the summary of the key contributions made in this research:

- Analysis, design, simulation, and experimental verification of the proposed two-phase, single-controllable-switch-converter based SRM drive.
- Analysis, design, simulation, and experimental verification of the proposed two-phase, two-controllable-switch-converter based SRM drive
- Analysis, design, simulation, and experimental validation of the proposed two-phase, two-switch based, high-speed SRM drive.
- Optimal efficiency control in single-pulse mode with optimal number of winding turns.
- Parameter insensitive position sensorless control and its implementation with the above proposed drive systems to achieve further cost reduction.
- Study of effect of input power factor correction and its implementation using only passive components and the drive structure without external electronics.
- Comparative study of the proposed drive systems, along with the existing brush-commutator or permanent magnet motors to provide guideline for their selection based on the requirement for their intended applications.

Bibliography

[1] R. Krishnan, “Whither motor drives: A case study in switched reluctance motor drives," Electrical Machines and Systems, 2007. ICEMS, pp.472-480, 8-11 Oct. 2007.

[2] V.R. Stefanovic, “Opportunities in Motor Drive Research – A View From Industry,” IEEE IECON, Proc. Record, pp.xxxvii-xlv, Orlando, 1995

[3] H. N. Hickok, “Adjustable speed—a tool for saving energy losses pumps, fans, blowers, and compressors,” IEEE Trans. Ind. Applicat., vol. 21, pp. 124–136, Jan./Feb. 1985.

[4] M. Chomat and T.A. Lipo, “Adjustable-Speed Single-Phase IM Drive With Reduced Number of Switches,” IEEE Trans. On IAS, Vol.39, No.3, pp. 819-825, May/Jun. 2003

[5] J.M. Bourgeois, J.M. Charreton, and P. Rault, “Improved Universal Motor Drive,” Application Note, AN422, ST Microelectronics, 1994.

[6] A.S. Ba-thunya, R. Khopkar, K. Wei, and H.A. Toliyat, “Single phase induction motor drives-a literature survey,” Electric Machines and Drives Conference, IEMDC 2001, IEEE International, vol., no., pp.911-916

[7] B. Welchko and T.A. Lipo, “A Novel Variable-Frequency Three-Phase Induction Motor Drive System Using Only Three Controlled Switches,” IEEE Trans. On IAS, Vol.37, No.6, pp. 1739-1745, Nov/Dec. 2001.

[8] R. Krishnan, “A Novel Single-Switch-Per-Phase Converter Topology for Four-Quadrant PM Brushless DC Motor Drive,” IEEE Trans. On IAS, Vol.33, No.5, pp. 1154-1161, Sep./Oct. 1997

[9] R. Krishnan, “An energy-efficiency-enhanced switched reluctance motor [From Mind To Market],” Industrial Electronics Magazine, IEEE , vol.1, no.1, pp.4-6, Spring 2007

[10] R. Krishnan, Switched Reluctance Motor Drives, CRC Press, 2001.

[11] M. Barnes, A.M. Michaelides, C. Pollock, “The design and performance of a self-starting 2-phase switched reluctance drive”, Power Electronics and Variable Speed Drives, 6th Int’l Conf. (Publ. No. 429), pp. 419 – 423, 1996

[12] R. Hamdy, J. Fletcher, and B.W. Williams, “Bidirectional Starting of a Symmetrical Two-Phase Switched Reluctance Machine,” IEEE Trans. On Energy Conversion, Vol. 15., No. 2, June, 2000

[13] S. Vukosavic, and V. R. Stefanovic, “SRM inverter topologies: a comparative evaluation,” IEEE Trans. On Industry Applications,Vol. 27, No. 6, 1991 pp. 1034 – 1047

[14] C. Pollock and B.W. Williams, “Power Converter Circuits for Switched Reluctance Motors with the Minimum Number of Switches,” IEE Proc. Vol. 137, Pt. B No. 6., 1990

[15] A. Ayob, V. Pickert, H. Slater, “Overview of low cost converters for single-phase switched reluctance motors,” 2005 European Conference on Power Electronics and Applications, 11-14, Sept. 2005

[16] S. Mir, "Classification of SRM Converter Topologies for Automotive Application," SAE Technical Paper Series Number 000-01-0133, March 6-9, 2000.

[17] M. Barnes and C. Pollock, "Selecting power electronic converters for single phase switched reluctance motors," in Proc. Power Electronics and Variable Speed Drives,1998, pp. 527-531.

[18] P.J. Lawrenson, J.M. Stephenson, P.T. Blenkinsop, J. Corda, and N.N. Fulton, "Variable speed reluctance motors," IEEE Proc. Electrical Power Appl. B, 127(4), 253-265, 1980.

[19] Davis, R.M. and R.J. Blake, "Inverter drive for switched reluctance motor circuits and component ratings," IEE Proc., 126–136, 1981.

[20] T.J.E. Miller, "Converter volt-ampere requirements of the switched reluctance motor drive," IEEE Trans. Industrial Application., Vol. 21, No. 5, pp.1136-1144, 1985

[21] R. Krishnan, S. Aravind, and P. Materu, "Computer-aided design of electrical machines for variable speed applications," Proceedings, IEEE-IECON'87, Cambridge, pp756-763.

[22] T.J.E. Miller, "Brushless reluctance motor drives," IEE Power Engineering Journal, Vol. 1, pp.283-289.

[23] R. Krishnan, and P. Materu, "Analysis and design of a new converter topology for switched reluctance motor drives, IEEE IAS, 1181–1185, 1989.

[24] R. Krishnan, P. Materu, "Design of a Single-Switch-per-Phase Converter for Switched Reluctance Motor Drives," IEEE Trans. on Industrial Electronics, vol.37, No.6, Dec.1990

[25] T.J.E Miller, *Switched Reluctance Motors and Their Control*, Magna Physics Publishing/Clarendon Press, Oxford, 1993

[26] M. Ehsani, I. Husain, K.R. Ramani, and J.H Galloway, "Dual-decay converter for switched reluctance motor drives in low-voltage applications," IEEE Trans. Power Electronics, 1993, 8, (2), pp. 224-230.

[27] M. Eshani,J.T. Bass,T.J.E. Miller, and R.L. Steigerwald, "Development of a unipolar converter for variable reluctance motor drives, " IEEE Trans. On Ind. App., Vol.23, No.3, pp.545-553, 1987.

[28] S. Mir, I. Husain, and M. Elbuluk, "Energy-Efficient C-dump Converters for Switched Reluctance Motors," IEEE Trans. on Power Electronics, Volume 12, Issue 5, Sept. 1997

[29] V.V. Deshpande, J.Y. Lim, "New converter configurations for switched reluctance motors wherein some windings operate on recovered energy," Industry Applications, IEEE Transactions on , vol.38, no.6, pp. 1558-1565, Nov/Dec 2002

[30] R. Krishnan, "Method, apparatus, and system for drive control, power conversion, and start-up control in an SRM or PMBDCM drive system," US patent, Pub. No.:US 2005/ 0146304 A1, Jul.7, 2005

[31] R. Krishnan, S. Y. Park, and K. S. Ha, "Theory and Operation of a Four-Quadrant Switched Reluctance Motor Drive with a Single Controllable Switch-The Lowest Cost Brushless Motor Drive", IEEE Trans. on IAS, Vol.41, No.4, pp.1047-55, Aug 2005

[32] R. Krishnan, "Single controllable switch based SRM drive system", Intellectual property of Ramu Inc., 2008. (Patent pending).

[33] Krishnan Ramu, "Apparatus for drive control, power conversion, and start-up control in a PMBDCM or two phase SRM Drive system", Patent pending, Pub.No: US 2005/0116679 A1, June 2, 2005.

[34] N.Mohan, T.M. Undeland, and W.P.Robbins, *Power Electronics: Converters, Applications, and Design*, John Wiley & Sons Inc., 2nd Edition, 1995

[35] W. Thong and C. Pollock, "Two Phase Switched Reluctance Drive with Voltage Doubler and Low DC link Capacitance" in Proc. *IEEE IAS Conference*, vol. 3, pp. 2155-2159 Oct. 2005.

[36] K. Ha, C. Lee, J. Kim, R. Krishnan, and S. G. Oh, "Design and development of brushless variable speed drive for low cost and high efficiency," in Proc. IEEE Industry Applications Conference, Vol. 4, pp.1649-1656, Oct. 2006.

[37] MacMinn, S.R., and Sember, J.W., "Control of a Switched-Reluctance Aircraft Engine Starter-Generator over a Very Wide Speed Range," in Proc. IECEC, Aug. 6-11, 1989.

[38] Kjaer, P. Nielsen, L. Andersen, and F. Blaabjerg, "A New Energy Optimizing Control Strategy for Switched Reluctance Motors," *IEEE Trans. Ind. Appl.*, vol. 31, no. 5, pp. 1088–1095, Sep./Oct. 1995.

[39] I. Kioskeridis and C. Mademlis, "Maximum Efficiency Operation of Switched Reluctance Motor Drives", *IEEE Trans. Energy Conversion*, Vol. 20, No. 4,Dec.2005

[40] C. Mademlis and I. Kioskeridis, "Performance Optimization in Switched Reluctance Motor Drives with Online Commutation Angle Control," *IEEE Trans. Energy Conv.*, vol. 18, no. 3, pp. 448–457, Sep. 2003.

[41] Y.Sozer, D.A.Torrey, and E.Mese, "Automatic control of excitation parameters for switched reluctance motor drives," *in Proc. Applied Power Electron. Conf and Exposition*, vol. 1, pp. 48-56, 2002.

[42] J.J Cribble, P.C. Kjaer, and T.J.Miller, "Optimal commutation in average torque control of switched reluctance motors", IEE Proc. Power Appl. Vol. 146, No.1,January 1999

[43] J. Corda, "Search for Optimum Number of Turns of Switched Reluctance Motor", *in Proc. Intl. Power Electronics Congress*, pp. 241 – 245, Oct. 1996.

[44] J.P. Lyons, S.R. MacMinn, and M.A. Preston, "Flux/current methods for SRM rotor position estimation," Proc. IEEE-IAS Annu. Meeting, 1991, pp.482-487

[45] N. H. Mvungi and J. M. Stephenson, "Accurate sensorless rotor position detection in an SR motor," in Proc.s European Power Electron. Conf., Vol. I, 1991, pp. 390-393.

[46] K.M. Richardson, C. Pollock, and J. O. Flower, "Design and Performance of a Rotor Position Sensing System for a Switched Reluctance Machine Propulsion Unit," in Proc. IEEE-IAS Annu. Meeting., 1996, pp.168-173

[47] H. Y. Yang, J.G. Kim, Y.C. Lim, S. K. Jeong, and Y. G. Jung, "Position detection and drive of a toroidal switched reluctance motor(TSRM) using search coils", IEE Proc. Electric Power Appl., 2004, pp.377-384

[48] I. Husain, S. Sodhi, and M. Ehsani, "A sliding mode observer basedcontroller for switched reluctance motor drives," in Proc. IEEE-IAS Annu. Meeting, 1994, pp. 635–643.

[49] Y. J. Zhan, C. C. Chan, and K. T. Chau, “A novel sliding-mode observer for indirect position sensing of switched reluctance motor drives,” IEEE Trans. Ind. Electron., vol. 46, pp. 390–397, Apr. 1999.

[50] F. Blaabjerg, L. Christensen, S. Hansen, J. P. Kristofferson, and P. O. Rasmussen, “Sensorless control of a switched reluctance motor with variable-structure observer,” Electromotion, vol. 3, no. 3, pp. 141–152, July 1996.

[51] A. D. Cheok, and N. Etugrul, “High Robustness of an SR Motor Angle Estimation Algorithm Using Fuzzy Predictive Filters and Heuristic Knowledge-Based Rules”, IEEE Trans.,1999, Ind. Electron, Vol. 46, pp.904-916

[52] E. Mese, and D. A. Torrey, “An Approach for Sensorless Position Estimation for Switched Reluctance Motors Using Artifical Neural Networks”, IEEE Trans., on Power Electron., 2002, pp.66-75

[53] S. Paramasivam, S. Vijayan, M. Vasudevan, R. Arumugam, and R. Krishnan, “Real-Time Verification of AI Based Rotor Position Estimation Techniques for a 6/4 Pole Switched Reluctance Motor Drive”, IEEE Trans. on Magnetics, Vol. 43, No. 7, July 2007

[54] C. Hudson, N. S. Lobo, and R. Krishnan, "Sensorless control of single switch based switched reluctance motor drive using neural network," in IECON 2004. 30th Annual Conference of IEEE, 2004, pp. 2349-2354 Vol. 3.

[55] G. Suresh, B. Fahimi, K. M. Rahman, and M. Ehsani, “Inductance based position encoding for sensorless SRM drives,” in Proc. IEEE Power Electronics Specialists Conf., vol. 2, 1999, pp. 832–837.

[56] H. Gao, F.R. Salmasi, and M. Ehsani, “Inductance model-based sensorless control of the switched reluctance motor drive at low speed”, IEEE Trans. on Power Electron., Nov. 2004. Vol. 19, pp: 1568- 1573

[57] S.R.MacMinn, W.J. Rzesos, P.M. Szczesny, and T.M. Jahns, “Application of sensor integration techniques to switched reluctance motor drives”, IEEE Trans. on Ind. Appl, 1992, Vol.28, No.6, pp. 1339-1344.

[58] M. Ehsani, I. Husain, and A. Kulkarni, “Elimination of discrete position sensor and current sensor in switched reluctance motor drives”, IEEE Trans. on Industry Appl., 1992,Vol. 28, No.1, pp. 128-135.

[59] P.P. Acarnley, R.J. Hill, and C.W. Hooper, “Detection of rotor position in stepping and switched reluctance motors by monitoring of current waveforms. IEEE Trans. Ind. Electron.”, 1985, Vol. 32, No. 3, pp. 215-222.

[60] S.K. Panda, and G.A.J. Amaratunga, “Analysis of the waveform detection technique for indirect rotor position sensing of switched reluctance motor drives,” IEEE Trans. on Energy Conversion, 1991,Vol. 6 , No. 3, pp. 476-483.

[61] G. Gallegos-Lopez, P. C. Kjaer, and T. J. E. Miller, “Anew sensorless method for switched reluctance motor drives”, IEEETrans. on Ind. Appl., Vol.34, No.4. pp. 832-840, July/August 1998.